分类号 _____ 密级 _____

U D C_____ 编号 _____

华中师范大学

博士学位论文

LHC-ALICE 实验中伴随粒子产生的能量依赖性研究

学位申请人姓名: 范 凤

申请学位学生类别: 全日制博士

申请学位学科专业: 粒子物理与原子核物理

指导教师姓名: 周代翠 教授

Antonio Ortiz Velásquez 教授

博士学位论文

LHC-ALICE 实验中伴随粒子产生的能量依赖性研究

论文作者：范　凤

指导教师：周代翠 教授

Antonio Ortiz Velásquez 教授

学科专业：粒子物理与原子核物理

研究方向：高能重离子碰撞实验

华中师范大学物理科学与技术学院

2024 年 06 月

Dissertation

Energy dependence of underlying-event observables with ALICE at the LHC

By

Feng Fan

Supervisor:	**Prof. Daicui Zhou**
	Prof. Antonio Ortiz Velásquez
Speciality:	**Particle Physics and Nuclear Phycisc**
Research Area:	**Heavy-ion Collisions Experiment**

College of Physical Science and Technology

Central China Normal University

June 2024

华中师范大学学位论文原创性声明和使用授权说明

原创性声明

本人郑重声明：所呈交的学位论文，是本人在导师指导下，独立进行研究工作所取得的研究成果。除文中已经标明引用的内容外，本论文不包含任何其他个人或集体已经发表或撰写过的研究成果。对本文的研究做出贡献的个人和集体，均已在文中以明确方式标明。本声明的法律结果由本人承担。

作者签名：　　日期：　　年　　月　　日

学位论文版权使用授权书

学位论文作者完全了解华中师范大学有关保留、使用学位论文的规定，即：研究生在校攻读学位期间论文工作的知识产权单位属华中师范大学。学校有权保留并向国家有关部门或机构送交论文的复印件和电子版，允许学位论文被查阅和借阅；学校可以公布学位论文的全部或部分内容，可以允许采用影印、缩印或其它复制手段保存、汇编学位论文。（保密的学位论文在解密后遵守此规定）

保密论文注释：本学位论文属于保密，在 ____ 年解密后适用本授权书。

非保密论文注释：本学位论文不属于保密范围，适用本授权书。

作者签名：　　导师签名：

日期：　　年　　月　　日　　日期：　　年　　月　　日

.....

本人已经认真阅读“CALIS 高校学位论文全文数据库发布章程”，同意将本人的学位论文提交“CALIS 高校学位论文全文数据库”中全文发布，并可按“章程”中的规定享受相关权益。同意论文提交后滞后：　半年：　一年：　二年发布。

作者签名：　　导师签名：

日期：　　年　　月　　日　　日期：　　年　　月　　日

摘　要

在重离子对撞实验的中心碰撞（即碰撞参数较小的碰撞）中，形成了一种强相互作用的热密物质，即夸克胶子等离子体（QGP）。长期以来，质子-质子碰撞被认为是在重离子实验中探测 QGP 信号的对照实验。然而，最近对高多重数质子-质子和质子-铅核碰撞（即小碰撞系统）的实验分析揭示了类 QGP 效应，比如集体性和奇异性增强，该效应的起源仍不清楚。目前，人们基于初态效应或与 QGP 形成相关的末态效应，来研究类 QGP 效应的成因。特别是，通过蒙特卡洛模型的预言及对比来探究实验现象，它在质子-质子碰撞中被广泛使用，且成功地描述了实验数据的某些特征。例如，多重部分子相互作用和色重联可以产生类集体效应，该效应在小碰撞系统中随着多重部分子相互作用数量的增加（碰撞参数的减小）而增强。这并非出人意料，因为在小碰撞系统中，经过散射产生的一些部分子在强子化之前仍然进行着相互作用。这种集体强子化行为产生了径向流效应，因此，对质子-质子碰撞中多重部分子相互作用的研究变得更加有趣。

在高多重数小碰撞系统的研究中存在选择偏差的问题，这一偏差主要表现为局域多重数的波动。例如，如果在非常窄的赝快度区间内测量多重数，那么选择高多重数事件会触发多喷注结构，这不符合我们的研究目的。也就是说，在小碰撞系统中，碰撞参数与带电粒子多重数之间的关联非常弱。在本文中，我们探究了两种事件分析方法，旨在减少不必要的选择偏差。其一是基于双强子关联的横向区域多重数分析方法；其二是扁平度分析方法，它用于进一步提高对碰撞参数的敏感度。

第一种分析方法是针对伴随事件。一个典型的质子-质子碰撞包含硬部分子-部分子散射和伴随事件。其中，伴随事件的粒子产生来自于束流残余和多重部分子相互作用，多重部分子相互作用是指在同一质子-质子碰撞中发生的两个或多个半硬部分子散射。

实验上，不可能将伴随事件从逐事件硬散射过程中分离出来。为了提高对伴随事件的敏感度，我们采用了 CDF 实验合作组引入的技术，该技术是基于对伴随事件具有不同敏感度的三个不同拓扑区域而建立的。这三个拓扑区域是根据触发粒子和关联粒子之间的方位角度差定义的，$|\Delta\varphi| = |\varphi^{\mathrm{assoc}} - \varphi^{\mathrm{trig}}|$，其中 φ^{trig} 和 φ^{assoc} 分别对应于事件中触发粒子和关联粒子的方位角。触发粒子是单个事件中具有最大横动量（$p_{\mathrm{T}}^{\mathrm{trig}}$）的粒子，则其余粒子称为关联粒子。近端 ($|\Delta\varphi| < \pi/3$) 和远端 ($|\Delta\varphi| > 2\pi/3$) 主要由硬散射部分子碎裂（强子化）主导。虽然，伴随事件覆盖了整个方位角平面，但总的来说，这两个区域对伴随事件的敏感度较低。相反，横向区域 ($\pi/3 < |\Delta\varphi| < 2\pi/3$) 对伴随事件最敏感，因为它受硬散射影响较小。

对不同能量下的质子-质子碰撞中伴随事件的研究表明，在横向区域中，平均粒子数密度作为 $p_{\mathrm{T}}^{\mathrm{trig}}$ 的函数随着 $p_{\mathrm{T}}^{\mathrm{trig}}$ 的增加而增加，直到达到 $5\,\mathrm{GeV}/c$ 时达到饱和。这种饱和效应通常

被解释为质子-质子碰撞偏向于产生小碰撞参数事件。换言之，这是一种在质子-质子碰撞中利用 $p_{\mathrm{T}}^{\mathrm{trig}} > 5\,\mathrm{GeV}/c$ 来选择中心碰撞的实验方法。在本文中，我们报告了在每个核子对质心能量为 5.02 TeV 的质子-质子和质子-铅核碰撞中进行的 CDF 分析（发表于 JHEP 2023）。结果显示，在高出 TEVATRON 2.5 倍以上质心能量的质子-质子和质子-铅核中的产生粒子数密度也呈现出非常相似的饱和效应，这意味着质子-铅核碰撞也偏向于产生小碰撞参数事件。这一发现表明，双强子关联的横向区域中的事件似乎是小碰撞系统中选择具有小碰撞参数事件的良好候选者。

如上所述，通过改变 $p_{\mathrm{T}}^{\mathrm{trig}}$ 的范围，可以选择平均碰撞参数接近于零的质子-质子碰撞。因此，碰撞参数的波动减小，并且预计横向区域中的带电粒子多重数分布具有 KNO 标度性。在蒙特卡洛模型模拟的 LHC 能区的质子-质子碰撞中，观察到横向区域的多重数分布在 $0.5 < R_{\mathrm{T}} < 2.5$ 范围内遵循类 KNO 标度行为，其中 $R_{\mathrm{T}} = N_{\mathrm{ch}}^{\mathrm{T}}/\langle N_{\mathrm{ch}}^{\mathrm{T}}\rangle$ 是伴随事件分类，$N_{\mathrm{ch}}^{\mathrm{T}}$ 是横向区域中单个事件的多重数，$\langle N_{\mathrm{ch}}^{\mathrm{T}}\rangle$ 则对应于平均多重数。这种类 KNO 标度性通常可以解释为单个质子-质子碰撞是由多个独立发射粒子的部分子相互作用叠加而成的，即多重部分子相互作用可以导致这样的效果。我们需要阐明的是，横向区域不仅包含伴随事件的贡献，还包含初态和末态辐射（ISR-FSR）的贡献。因此，在较低或较高 R_{T} 下类 KNO 标度的破坏是否归因于横向区域中 ISR-FSR 的影响。为了理解类 KNO 标度被破坏的原因，本文将横向区域平均分为两个子区间。然后，根据两个子区间中的相对多重数的大小定义了 “trans-max”（具有较大多重数的子区间）和 “trans-min” 区间（具有较小多重数的子区间），它们分别对 ISR-FSR 和伴随事件更敏感。根据这两个子区间的多重数（$N_{\mathrm{ch}}^{\mathrm{Tmax}}$ 和 $N_{\mathrm{ch}}^{\mathrm{Tmin}}$），我们还定义了 $R_{\mathrm{T}}^{\mathrm{max}}$ 和 $R_{\mathrm{T}}^{\mathrm{min}}$。

在本文中，我们首次利用 ALICE 探测器测量研究了 $\sqrt{s} = 2.76$、5.02、7 和 13 TeV 下质子-质子碰撞中横向区域、trans-max 和 trans-min 区间的 KNO 变量（发表于 JHEP 2024）。实验结果显示，在误差允许范围内（20%），横向区域的多重数分布在 $0 < R_{\mathrm{T}} < 3$ 范围内具有类 KNO 标度性；然而，当 $R_{\mathrm{T}} > 3$ 时，类 KNO 标度性被破坏，这可能是由喷注碎裂偏差导致的。在 trans-max 区间观察到了类似的结果。然而，trans-min 区间的多重数分布在更广的 $R_{\mathrm{T}}^{\mathrm{min}}$ 范围内（$0 < R_{\mathrm{T}}^{\mathrm{min}} < 4$）也呈现出类 KNO 标度行为；但当 $R_{\mathrm{T}}^{\mathrm{min}} > 4$ 时，这种标度性依然不成立，这可能也是由喷注碎裂偏差引起的。为了更深入地理解这三个区域中的粒子产生机制，我们使用负二项分布函数对这些粒子多重数分布进行了拟合。结果表明，单个负二项分布能够有效描述 $N_{\mathrm{ch}}^{\mathrm{T}}$ 和 $N_{\mathrm{ch}}^{\mathrm{Tmin}}$ 分布，且对 $N_{\mathrm{ch}}^{\mathrm{Tmin}}$ 分布的拟合效果更佳，这与碰撞参数波动的减小是一致的。相比之下，$N_{\mathrm{ch}}^{\mathrm{Tmax}}$ 分布的拟合效果最差，这是因为 trans-max 区间包含两种贡献：伴随事件和来自 ISR-FSR 的喷注碎裂。我们还报告了横向区域、trans-max 和 trans-min 区间中平均多重数密度的质心能量依赖性。我们的结果（$\sqrt{s} = 2.76$、5.02、7 和 13 TeV 的质子-质子碰撞）与现有实验数据的趋势一致。同时，我们发现 $s^{0.27} + 0.14\log(s)$ 函数能够有效

描述平均多重数密度，其中幂律项和对数项分别描述了质子-质子碰撞中对多重部分子相互作用和 ISR-FSR 敏感的拓扑区域的粒子产生。这些结果表明，横向区域和 trans-min 区间的多重数是选择具有小碰撞参数的质子-质子碰撞的良好候选者。然而，多重数范围仅限于无偏差质子-质子碰撞中横向区域平均多重数的 $2-3$ 倍左右。

正如前文所述，带电粒子多重数的研究受到选择偏差的影响。这种偏差也在 R_{T} 分析中观察到，我们只能在 $R_{\mathrm{T}} \approx 2-3$ 范围内进行相关研究。为了更好地控制这种偏差的影响，本文探讨了一种新的事件分析方法，即扁平度。扁平度是根据前向赝快度区域的多重数定义的，相较于 R_{T}，它可能更为有效。我们采用 PHYTHIA 8 事件产生器对 $\sqrt{s} = 13.6\,\mathrm{TeV}$ 下质子-质子碰撞中的扁平度进行了系统研究（发表于 PRD 2023），同时采用被广泛使用的多重数估计器进行了相同的分析。结果显示，两者都表现出与平均多重部分子相互作用活动相同水平的相关性，但局域多重数波动引起的偏差对扁平度的影响较小。因此，扁平度为 ALICE RUN 3 的数据分析提供了新的研究方向。目前，本课题组正在利用 RUN 3 实验数据进行扁平度的研究。

本论文由如下内容组成：第 1 章简要介绍强相互作用、质子-质子碰撞中的粒子产生机制、伴随事件、KNO 标度、以及本文分析中使用的蒙特卡洛模型。第 2 章简要介绍 ALICE 探测器，并着重介绍本文分析中使用的主要探测器。第 3 章描述数据的选取和研究方法。第 4 章讨论伴随粒子产生的能量依赖性。第 5 章讨论质子-质子和质子-铅核碰撞中的伴随事件的性质。第 6 章讨论扁平度的蒙特卡洛模拟结果。第 7 章给出研究结论及未来展望。

关键词： 伴随事件及其性质; 多重部分子相互作用; 初态和末态辐射;KNO 标度; 负二项分布; 扁平度

Abstract

In heavy-ion collider experiments, a hot and dense, strongly-interacting nuclear matter, the so-called quark–gluon plasma (QGP) is formed in central collisions (collisions with small impact parameter). For many years, pp collisions were considered as a control experiment to extract the genuine QGP effects from heavy-ion data. However, recent studies on high-multiplicity proton-proton (pp) and proton-lead (p–Pb) collisions, the so called small-collision systems, unveiled QGP-like effects such as collectivity and strangeness enhancement. The origin of the new effects is still unknown. Two approaches based on either final-state effects (QGP formation) or initial-state effects are currently under investigation. In particular, the Monte Carlo (MC) models widely used in pp collisions have been successful at describing some aspects of data. For example, multi-parton interactions (MPI) and colour reconnection (CR) can produce collective-like effects. The effects increase with the increase of the number of MPI (decrease of the impact parameter) involved in the collision. This is not surprising because in these collisions, several scattered patrons are produced and they are allowed to interact before the hadronization. This sort of collective hadronization mimics radial flow effects. The study of pp collisions as a function of MPI is therefore interesting.

One issue with the study of high multiplicity pp and p-Pb collisions are the selection biases, which are basically biases towards local multiplicity fluctuations. For example, if the multiplicity is measured in a very narrow pseudorapidity interval then requiring a high multiplicity could act as a trigger on jet multiplicity, which is not what we want to study. This is, the correlation between the impact parameter and the charged particle multiplicity is very weak in small-collision systems. In this thesis we investigate two event activity estimators aimed at reducing the unwanted selection biases. One of them is the multiplicity in the transverse region of the di-hadron correlation, and the second one is a proposal to further improve the sensitivity to the impact parameter of the collision using the so-called flattenicity estimator.

The first estimator aims at triggering on the underlying event. A typical pp collision can be viewed as a hard parton-parton scattering accompanied by UE which consists of particles from beam-beam remnants (BBR) and MPI. MPI refers to two or more semi-hard parton-parton scatterings occurring within the same pp collision.

Experimentally, it is impossible to uniquely separate the UE from the event-by-event hard scattering process. In order to enhance the sensitivity to UE, we followed the technique introduced by the CDF Collaboration, which is based on the definition of three distinct

topological regions with different sensitivities to the UE. The three topological regions are defined from the angular difference between the trigger and associated particles, $|\Delta\varphi| = |\varphi^{\rm assoc} - \varphi^{\rm trig}|$, where $\varphi^{\rm trig}$ and $\varphi^{\rm assoc}$ refer to the value of the azimuthal angle for the trigger particle and for associated particles in the event, respectively. The trigger particle is the one with the largest transverse momentum ($p_{\rm T}^{\rm trig}$) in the event, and the rest are termed as associated particles. The toward ($|\Delta\varphi| < \pi/3$) and away ($|\Delta\varphi| > 2\pi/3$) regions are dominated by the fragments of jets. Although UE appears everywhere, in general, these two regions are less sensitive to the UE. In contrast, the transverse region ($\pi/3 < |\Delta\varphi| < 2\pi/3$) is the most sensitive to UE since it is less affected by contributions from the hard scattering.

Measurements of UE in pp collisions at different energies showed that in the transverse region the mean charged-particle multiplicity as a function of $p_{\rm T}^{\rm trig}$ ("number density") increased with $p_{\rm T}^{\rm trig}$ up to about $5\,{\rm GeV}/c$ (plateau) where it saturated. Such saturation effect observed in the number density is commonly interpreted as a bias towards collisions with small impact parameter. In other words, selecting pp collisions with $p_{\rm T}^{\rm trig}$ above $5\,{\rm GeV}/c$ is an experimental approach to select central pp collisions. Among the results presented in this thesis, we report the CDF analysis implemented in pp and p-Pb collisions at a centre-of-mass energy per nucleon pair of 5.02 TeV (published in JHEP 2023). The results exhibit a very similar saturation of the number density in p-Pb collisions, suggesting a bias in the impact parameter of the nucleon-nucleon collision, and to some extend in the p-Pb impact parameter. This finding suggests that the event activity in the transverse region of the di-hadron correlations seems as a good candidate to select pp and p-Pb collision with small impact parameter.

As explained above, the selection on $p_{\rm T}^{\rm trig}$ allows to select pp collisions with average impact parameter near to zero. Therefore, the fluctuations on impact parameter diminish, and a Koba-Nielsen-Olesen (KNO) scaling of the multiplicity distributions in the transverse region is expected. This scaling was observed in MC simulation for pp collisions at the LHC energies for $0.5 < R_{\rm T} < 2.5$, where $R_{\rm T} = N_{\rm ch}^{\rm T}/\langle N_{\rm ch}^{\rm T}\rangle$ is the relative transverse activity classifier, $N_{\rm ch}^{\rm T}$ being the charged-particle multiplicity and $\langle N_{\rm ch}^{\rm T}\rangle$ being the mean charged-particle multiplicity in the transverse region that is calculated considering all the events. The KNO-like scaling is expected in models which assume that a single pp collision is merely a superposition of a given number of elementary partonic collisions emitting particles independently. Therefore, MPI is expected to produce such an effect. One has to keep in mind that the transverse region does not only include contributions from UE, but also from initial- and final-state radiation (ISR-FSR). Therefore, it raises a question whether the violation of the KNO-like

scaling at lower or higher R_{T} is attributed to ISR-FSR. To understand this violation, in this work the transverse region is further subdivided in two regions, defined according to their relative multiplicities: "trans-max" (the sub-transverse region with the larger multiplicity) and "trans-min" (the sub-transverse region with the smaller multiplicity) regions which have an enhanced sensitivity to ISR-FSR and UE, respectively. Using $N_{\mathrm{ch}}^{\mathrm{Tmax}}$ (the multiplicity in the trans-max region) and $N_{\mathrm{ch}}^{\mathrm{Tmin}}$ (the multiplicity in the trans-min region), instead of $N_{\mathrm{ch}}^{\mathrm{T}}$, we can also define the quantities $R_{\mathrm{T}}^{\mathrm{max}}$ and $R_{\mathrm{T}}^{\mathrm{min}}$, respectively.

In this thesis, we report for the first time the measurement of the multiplicity distributions in KNO variables for the transverse, trans-max and trans-min regions using pp data at $\sqrt{s} =$ 2.76, 5.02, 7, and 13 TeV reconstructed with the ALICE detector (published in JHEP 2024). Our results show that, in the transverse region, within 20%, a KNO-like scaling holds for $0 < R_{\mathrm{T}} < 3$, whereas for higher R_{T} values ($R_{\mathrm{T}} > 3$), the KNO-like scaling is broken which might be attributed to jet fragmentation bias. The results for trans-max are qualitatively similar to those reported for the transverse region. On the other hand, for the trans-min region, the KNO-like scaling holds within a wider $R_{\mathrm{T}}^{\mathrm{min}}$interval ($0 < R_{\mathrm{T}}^{\mathrm{min}} < 4$), whereas for $R_{\mathrm{T}}^{\mathrm{min}} > 4$ the KNO-like scaling is still broken which might be also a result of jet fragments bias. To further understand the production mechanism of particles in the three regions, single negative binomial distributions (NBD) were fitted to data. The parameterisation suggests that a single NBD is enough to describe $N_{\mathrm{ch}}^{\mathrm{T}}$ and $N_{\mathrm{ch}}^{\mathrm{Tmin}}$ distributions, and the best result is observed for $N_{\mathrm{ch}}^{\mathrm{Tmin}}$ distributions. This result is consistent with the reduction in the fluctuations of impact parameter. In contrast, the quality of the fit gets worst for the trans-max region because there two components are present, the UE as well as jet fragments from ISR and FSR. We also report the centre-of-mass energy dependence of the average multiplicity density in the transverse, trans-max, and trans-min regions. Our results in pp collisions at $\sqrt{s} = 2.76$, 5.02, 7, and 13 TeV follow the trend of existing data results. The average multiplicity density as a function of centre-of-mass energy can be described by the parameterisation of the form $s^{0.27} + 0.14\log(s)$. The power-law term and the logarithmic term describe the MPI- and ISR-FSR-sensitive topological region of the collision, respectively. The results reported here support the interpretation that the multiplicity in transverse region and trans-min are good candidates to select pp collisions with small impact parameter. However, the multiplicity reach is limited to around $2-3$ times the average multiplicity in minimum-bias pp collisions.

As already stated, the studies as a function of the charged-particle are affected by selection biases. This bias is also observed in R_{T}, as mentioned above, we could only explore

multiplicities up to $R_{\mathrm{T}} \approx 2-3$. In order to have a better control on the biases, this thesis explores the use of the new event classifier, flattenicity, which is calculated in the forward pseudorapidity region, and which could be more powerful than R_{T}. A comprehensive study of flattenicity in pp collisions $\sqrt{s} = 13.6\,\mathrm{TeV}$ is performed using PYTHIA 8 simulations (published in PRD 2023). A comparison between the widely used multiplicity estimator and flattenicity shows that although both of them show the same level of correlation with the average MPI activity, flattenicity is less affected by the bias due to local multiplicity fluctuations. The implementation of flattenicity in ALICE during RUN 3 is currently ongoing by other groups.

This thesis is organised as follows. In chapter 1 the main aspects of strong interactions are briefly introduced, as well as the particle production mechanisms in pp collisions, the UE and KNO scaling, and the MC models used in this theses. Chapter 2 gives a brief review of the ALICE detectors, especially focusing on the main detectors used in this thesis. Chapter 3 presents the data sample and analysis strategy. In chapter 4 the energy dependence of UE are discussed. In chapter 5 UE properties in pp and p–Pb collisions is discussed. In chapter 6 a MC study of flattenicity is reported. Chapter 7 summarises the main results with outlook.

Keywords: Underlying event; Multi-parton interactions; Initial- and final-state radiation; Koba-Nielsen-Olesen scaling; Negative binomial distributions; Flattenicity

目　录

第 1 章 Introduction

1.1 Quantum Chromodynamics

The universe appears to be governed by the four fundamental forces: gravity, electromagnetism, the strong force and the weak force. Strong interactions bind nuleons in nulei, which is a manifestation of the fundamental theory of strong interactions, called Quantum Chromodynamics (QCD). In QCD the fundamental degrees of freedom are quarks and gluons. Quarks are characterised by the flavour quantum number. Up to the present time, there are six different flavours: u (up), d (down), s(strange), c(charm), b (bottom) and t (top). In addition to fractional electric charges of $+\frac{2}{3}e$ or $-\frac{1}{3}e$, quarks carry a colour charge. Quarks can exist in three different colour states: red, green and blue.

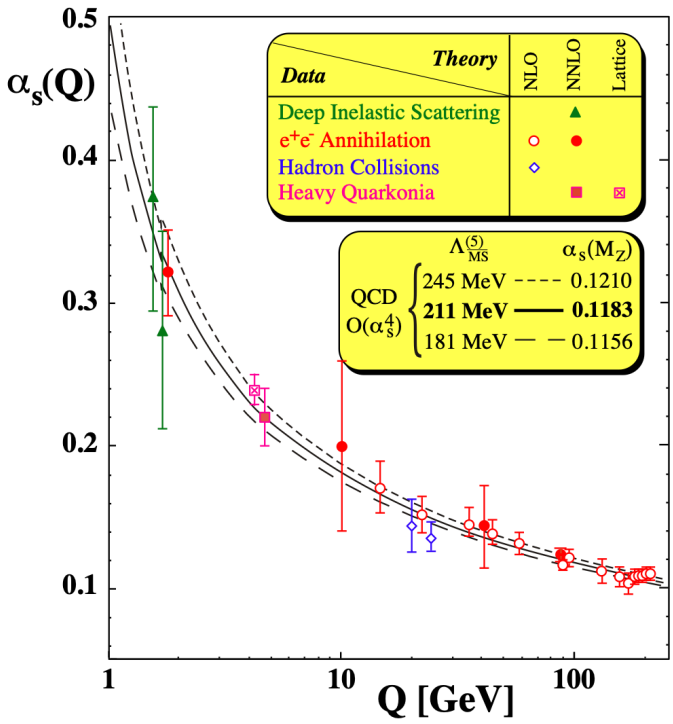

图 1.1: The strong coupling constant α_S as a function of the momentum transfer Q. The figure is taken from [1]

The strong interactions between quarks are mediated by gluons (with eight kinds of "colour"), massless particles carrying colour charge, which are remarkably distinct from the electromagnetic interaction typified by photons without charge. For instance, in terms of the exchange particle, gluons can directly couple to other gluons, whereas photons cannot directly

couple to other photons. It is worth noting that there is a crucial characteristic in the strong interactions: in general both quarks and gluons cannot individually exist in nature but only occur within colour-neutral composite hadrons, i.e., “colour confinement”.

The running coupling constant for the strong interaction is predicted by QCD to be

$$\alpha_s(Q^2) = \frac{\alpha_0}{1 + \frac{11n_c - 2n_f}{12\pi\alpha_0 \ln(Q^2/\mu^2)}}, \tag{1.1}$$

where Q is the four-momentum transfer involved in the interaction process, α_0 is the coupling constant for the momentum transfer scale of μ, n_c the number of colour charges and n_f is the number of flavours. Thus, provided the number of quark flavours is less than 16 [2], it follows that α_s decreases with increasing energy (momentum) transfer (see Fig. 1.1). When the distance scale of the interaction is small, as for example when one probes the high momentum component of the distribution of quarks, the coupling constant is small. Therefore, quarks move almost freely inside hadrons, corresponding to the case of “asymptotic freedom”. On the other hand, when the distance scale is large, the interaction strength is large, resulting in the “confinement” of quarks.

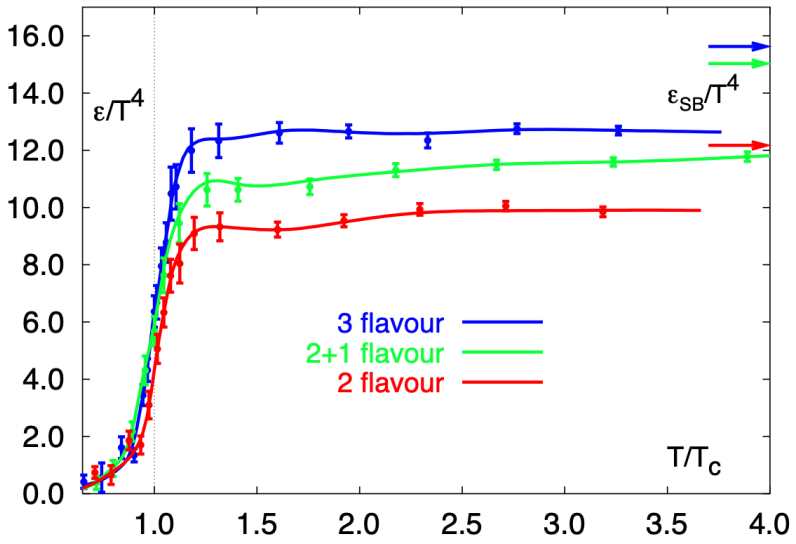

图 1.2: Lattice QCD results [3] for the energy density ε/T^4 as a function of the temperature normalised to the critical temperature T_C. The arrows on the right side correspond to the values for the Stefan-Boltzmann limit.

Asymptotic freedom implies that QCD physics gets simpler at very high temperatures. At sufficiently high temperatures and densities, QCD predicts an entirely new form of matter

called quark–gluon plasma (QGP). In such a plasma, quarks and gluons are no longer confined in hadrons, but behave like free single particles. In contrast to normal matter these single particles are not colourless.

Theoretically, the crossover phase transition from hadronic matter to a possible QGP has been studied in lattice QCD (LQCD) calculations. As shown in Fig. 1.2, LQCD calculation at zero baryon chemical potential (μ_B) predicts that at a critical temperature T_C of $\sim 155\,\mathrm{MeV}$ [3, 4] corresponding to an energy density of $1\,\mathrm{GeV/fm^3}$, nuclear matter undergoes a crossover phase transition to a deconfined state of quarks and gluons.

It is commonly believed that a QGP was realised right after (a few microseconds after) the Big Bang, the believed origin of our present universe. Today quark matter is expected to exist, due to high particle densities, in neutron stars. It is expected that, by means of high energy heavy-ion collisions, a sufficiently large particle density and high temperature can be established to form a QGP.

1.2 Heavy-ion collision

Ultra-relativistic heavy-ion collisions allow the investigation of the QGP formed under extreme conditions of high energy density and temperature. These conditions have been achieved in heavy nuclei collisions at both LHC and RHIC. The so-called standard model of heavy-ion collisions consists of several stages to describe the evolution of the system, a schematic representation is shown in Fig. 1.3. Following the description presented in Ref. [5], such a evolution include:

- The initial state is defined by the wave functions of the two incident nuclei, which are universal and do not depend on any certain partonic-scattering process. As the energy of the projectiles increases, one would expect an increase in the strength of the transverse colour field.

- When heavy nuclei collide, most of partonic interactions involves low momentum transfers (small Q^2 interactions). However, occasionally, hard scatterings may occur and partons are scattered at large angles.

- Right after the collision, the system is far of equilibrium. It takes some time to the system to reach the equilibrium ($< 1\,\mathrm{fm}/c$) and the QGP is formed. The temperature is high, and partons are deconfined. The system then develops an hydrodynamic evolution.

- At some point the temperature would be low enough to have the cross over transition. At this stage, the degrees of freedom are not dictated anymore by partons, instead, a hadron gas is formed.
- When inelastic interactions stop, the yields of the different particle species get fixed and we said that the system achieved the chemical equilibrium.
- Hadrons might still interact elastically, and therefore the spectral shapes of the hadron transverse momentum distributions can still be affected. When such interactions stop, the system achieved the kinetic freeze out, and hadrons decouple from the system. Final stable particles are detected by apparatus like ALICE. The goal is then to reconstruct the particle trajectories as well as identify the particles using different techniques.

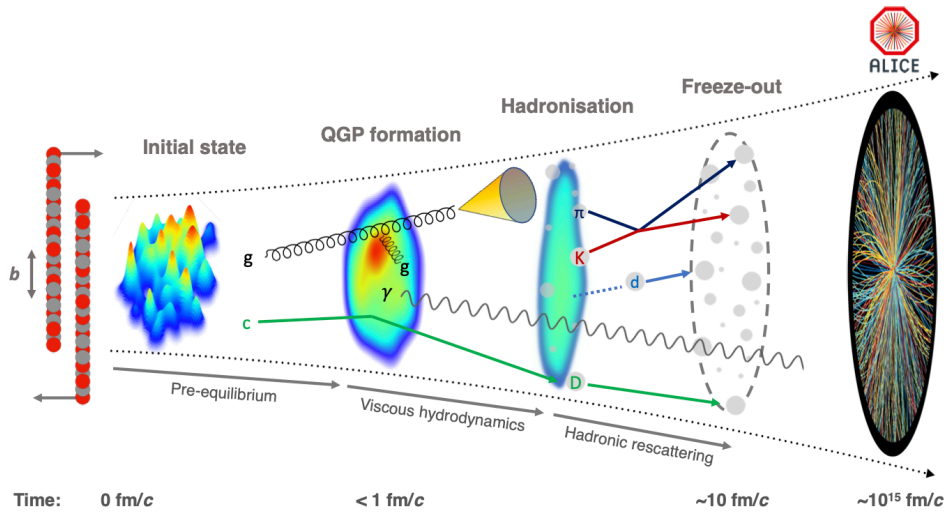

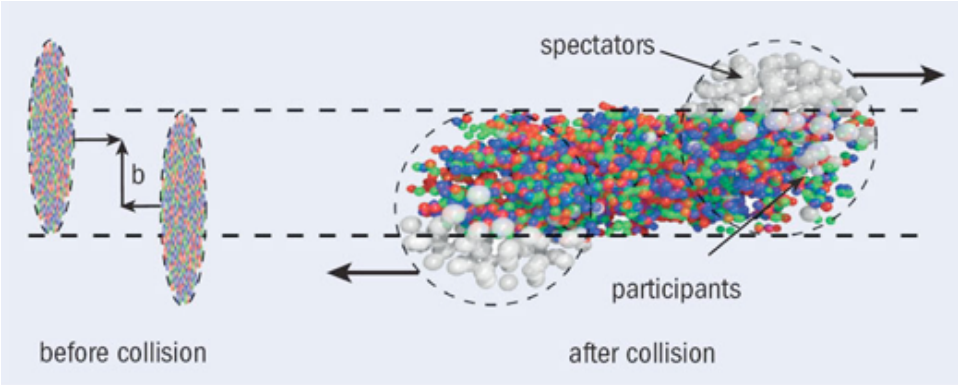

图 1.3: The evolution of a heavy-ion collision. Figure taken from Ref. [5].

In the centre-of-mass frame (the "lab frame" at a collider), when two ultra relativistic nuclei collide head on, each incident nucleus is a Lorentz contracted disc. In these two nuclei, the number of nucleons participating in the nuclei collision (at least once) is termed as $N_{\rm part}$, and the total number of inelastic nucleon-nucleon collisions is assigned as $N_{\rm coll}$, these collisions are the responsible for the hard scatterings that allows one to study for example the interaction of a fast parton within the medium. $N_{\rm part}$ and $N_{\rm coll}$ are correlated with the impact parameter b of the collision, it is just the distance between the centre of two colliding nuclei. For large $N_{\rm part}$ values (small b values), the collision can achieve up to 2A participating nucleons (if each colliding nuclei have the same number A of nucleons), whereas for $N_{\rm coll}$ the respective number is $\approx A^{4/3}$. The nucleons that do not participate in the collision are termed as spectators, and continue travelling approximately along the beam direction after the collision. For this reason hadronic calorimeters in the forward region are important because they provide a measure of $N_{\rm part}$.

The expanding high energy density system generated around the midpoint between the two discs, where the collision occurred, has an energy density at that time that is still far in excess of $500\,{\rm MeV/fm^3}$, the energy density inside a typical hadron. Thus, the quarks and gluons produced in the collision cannot be described as a collection of distinct individual hadrons. They are so strongly coupled to each other that they form a collective medium, QGP [6], that expands and flows as a relativistic hydrodynamic fluid [4]. As the discs recede from each other and the QGP generated between them is expanding and cooling, at the same time new QGP is continuously forming in the wake of each receding disc. After further expansion, it subsequently falls apart into hadrons. Meanwhile, remnants of the original nuclei progress in the forward and backward directions.

In the case of central heavy-ion collisions since the pressure gradient is isotropic, the collective motion is radial. The transverse momentum distribution of hadrons will be affected depending on the hadron mass. The higher the hadron mass, the larger the effect of collective radial flow. For non-central collisions, in the overlap region, the process is the same as described above, except that the droplet of QGP is formed with an initial approximately almond shape in the transverse plane. In reality, because nuclei are made of individual nucleons the energy density of the QGP that forms is lumpy in the transverse plane, making it neither perfectly circular in head-on collisions nor perfectly almond shape in non-central collisions. Deviations from circular symmetry in the initial shape of the QGP, whether due to off-centre collisions or the lumpiness and fluctuations of the incident nuclei, result in anisotropies in

the pressure of the hydrodynamic fluid, which in turn drive anisotropies in the expansion velocity. Figure 1.4 shows the flow coefficients measured in heavy ion collisions. It is worth mentioning that the size of the anisotropic flow coefficient reflects that the system actually behaves more like a fluid rather than a gas. This observation yielded to the discovery of the strongly-interacting quark gluon plasma at the RHIC energies. We therefore speak about a perfect fluid rather than a gas.

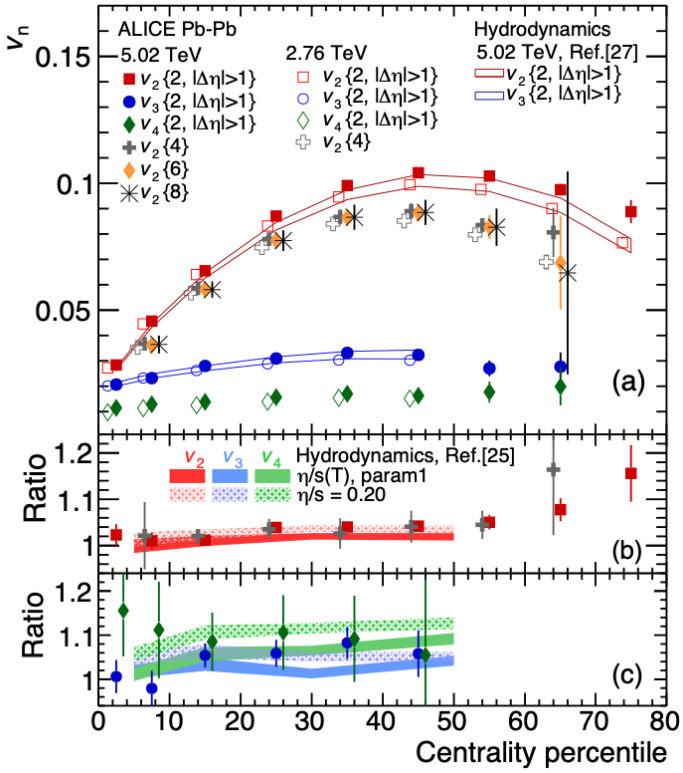

图 1.4: (a) Anisotropic flow v_n integrated over the p_{T} range $0.2 < p_{\mathrm{T}} < 5.0\,\mathrm{GeV}/c$, as a function of event centrality, for the two-particle (with $|\Delta\eta| > 1$) and multi-particle correlation methods. Measurements for Pb–Pb collisions at $\sqrt{s_{\mathrm{NN}}} = 5.02$ (2.76) TeV are shown by solid (open) markers. (b) Ratios of $v_2\{2, |\Delta\eta| > 1\}$ and $v_2\{4\}$ results for Pb–Pb collisions at $\sqrt{s_{\mathrm{NN}}} = 5.02$ and 2.76 TeV. (c) Ratios of $v_3\{2, |\Delta\eta| > 1\}$ and $v_4\{2, |\Delta\eta| > 1\}$ measurements for Pb–Pb collisions at $\sqrt{s_{\mathrm{NN}}} = 5.02$ and 2.76 TeV. Figure is taken from [7].

In the field of heavy-ion physics, the measurements in proton-proton (pp) collisions were used as control experiment in order to extract the genuine effects of QGP from heavy-ion data. This because no QGP was expected to be formed in minimum-bias pp collisions, thus the produced partons were expected to evolve without suffering the effects from the strongly-

interacting medium. However, given the large amount of high-quality data collected at the LHC during the Runs 1 and 2, studies as a function of the particle multiplicity in pp collisions were performed aimed at searching for QGP effects in high-multiplicity pp collisions. This yields a series of results that up today we have not fully understand their origin.

In the sake of seeking for signatures of QGP, one looks for differences in measurements between collisions having QGP (nucleus-nucleus collisions) and collisions without QGP (minimum-bias pp collisions). Below, we will briefly review some of the potential experimental signals that have been proposed to probe the QGP system in relativistic heavy-ion collisions.

Anisotropic flow. As mentioned before, in non-central collisions the droplet of QGP is formed with an initial approximately lenticular shape in the transverse plane, whether due to off-centre collisions or the lumpiness and fluctuations of the incident nuclei, which results in anisotropies in the pressure of the hydrodynamic fluid, in turn driving different expansion rates depending on the azimuthal angle. Such an azimuthal anisotropy is transferred to the final momentum of colour neutral particles (hadrons). Experimentally, the azimuthal anisotropy of the particle's transverse momentum spectra can be described by its Fourier expansion with respect to the reaction plane,

$$\frac{\mathrm{d}N}{\mathrm{d}\varphi} \propto 1 + 2\sum_{n=1}^{\infty} v_n \cos\left[n(\varphi - \Phi_n)\right], \tag{1.2}$$

where φ is the particle's azimuthal angle and Φ_n is the azimuthal angle of the reaction plane in the lab frame for the n^{th} harmonic. The Fourier coefficients v_n characterise the anisotropy of produced particles. For example, the first (second) order coefficient v_1 (v_2) represents the directed flow (elliptic flow) intensity. Anisotropic flow can also be studied by multi-particle correlations (cumulants), seen in Fig. 1.4.

Strangeness enhancement. In high-energy hadronic collisions, $q\bar{q}$ pair is mainly produced by hard scattering, however, the production of particles containing strange quarks is normally suppressed due to the high mass of the s-quark ($m_s \sim 170\,\mathrm{MeV}/c^2$) compared to u and d quark masses. In the presence of QGP in a collision, where gluon density is high at high temperature, the $s\bar{s}$ pair will be produced from the gluon fusion reaction $gg \to s\bar{s}$, with a threshold energy of around 200 MeV, and the typical thermal energy of massless gluons is 3 T, which results in an enhancement of the $s\bar{s}$ pair production compared to a confined medium. Figure 1.5 shows the ratios of the yields of K^0_{S}, Λ, Ξ and Ω to the pion ($\pi^+ + \pi^-$) yield as a function

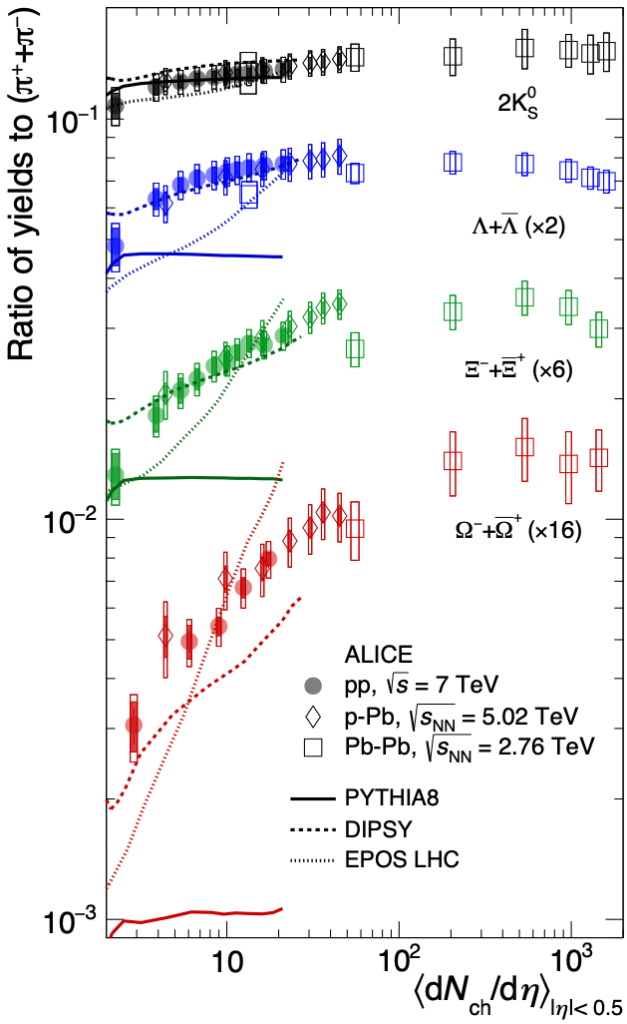

图 1.5: p_{T}-integrated yield ratios to pions $(\pi^+ + \pi^-)$ as a function of $\langle \mathrm{d}N_{\mathrm{ch}}/\mathrm{d}\eta \rangle$ measured in $|\mathrm{y}| < 0.5$. Figure is taken from [8].

of $\langle \mathrm{d}N_{\mathrm{ch}}/\mathrm{d}\eta \rangle$. A significant enhancement of strange to non-strange hadron production is observed for lead-lead (Pb–Pb) collisions.

However, in high-multiplicity pp and proton-lead (p–Pb) collisions, called as small-collision systems, heavy-ion-like effects are also observed [9]: long-range azimuthal correlations [10] (see Fig. 1.6), radial flow [11] and strangeness enhancement [8] (see Fig. 1.5). The origin of the new effects is still unknown. Two approaches based on either final state effects (QGP formation) and initial state effects are currently under investigation. For example, the formation of QGP in pp collisions would require the observation of jet quenching effects that results from the exchange of quantum numbers between the hard probe and the medium.

But jet quenching effects have not been seen so far in pp collisions. This probably is not a required observation because the size of the system is small and therefore, jet quenching effects might be tiny. What is really an issue for the QGP explanation of the new phenomena is the recent discovery of long range angular correlations even in low multiplicity pp collisions ($\mathrm{d}N_{\mathrm{ch}}/\mathrm{d}\eta \approx 5$) or in ultra-peripheral Pb–Pb collisions. In both case it is hard to argue that collectivity could be developed with a few number of particles.

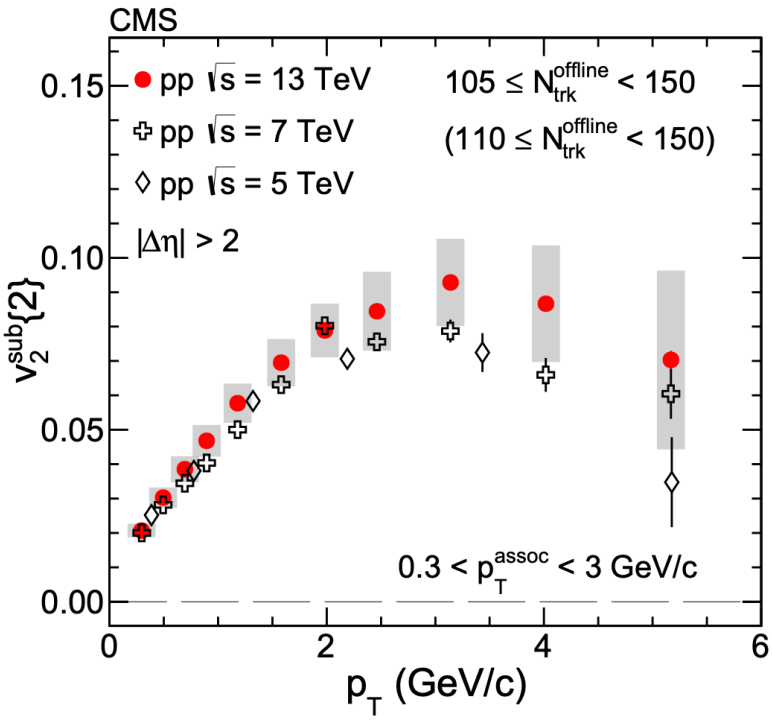

图 1.6: The v_2 results of inclusive charged particles, after subtracting correlations from low-multiplicity events, as a function of p_{T} in pp collisions at $\sqrt{s} = 13\,\mathrm{TeV}$ for $105 \leq N_{\mathrm{trk}}^{\mathrm{offline}} < 150$ and at $\sqrt{s} = 5,\ 7\,\mathrm{TeV}$ for $110 \leq N_{\mathrm{trk}}^{\mathrm{offline}} < 150$. Figure is taken from [10].

Given the issues to describe all the observations from the QGP perspective, this thesis focuses on an interpretation that would not invoke the QGP formation. In particular, the Monte Carlo models widely used in high-energy hadronic collisions have been successful at describing some aspects of data. For example, multi-parton interactions (MPI) and colour reconnection (CR) can produce collective-like effects [12]. The interactions among strings have allowed to qualitatively reproduce the strangeness enhancement. Therefore, the particle production as a function of quantities sensitive to MPI has attracted the interest of a fraction of the heavy-ion community [13–17]. Thus, the studies on the underlying event (UE), mainly

including MPI, are quite important, and this is the focus of the present work.

MPI is a phenomenon that is somehow expected given the composite nature of protons. At large energies more than one parton-parton scattering is expected within the same pp collision. This is consistent with the observation that the jet cross section is larger that the total pp cross section for $p_{\mathrm{T}} \approx 5\,\mathrm{GeV}/c$ at the LHC energies. One way to understand this behaviour is assuming that more than one scattering can occur in the same collision. In Monte Carlo generators the amount of MPI is parameterised in terms of the impact parameter. The smaller the impact parameter of the collision, the larger the hadronic overlap matter in the collision and therefore larger probability to have more than one MPI. This parameterisation is successful at describing the multiplicity distributions in particular the high multiplicity tails. The model with varying impact parameter describe the multiplicity distributions at the LHC energies.

1.3 Underlying event

The inelastic pp cross section has contributions from diffractive (single diffraction and double diffraction) and non-diffractive processes. For non-diffractive processes, occasionally, a hard parton-parton scattering occurs producing jets and high transverse momentum (p_{T}) particles. The hard scattering component of the event consists of particles that arise from the hadronization of the two outgoing partons (i.e., the primary outgoing two jets) plus the particles that arise from initial- and final-state radiation (ISR-FSR, i.e., multi-jets). The UE consists of particles from the proton break-up (beam-beam remnants) and the MPI that accompany such a hard scattering [18]. MPI, i.e. two or more semi-hard parton-parton scatterings within the same pp collision, is a natural consequence given the composite nature of hadrons [19]. Several data support the presence of MPI in hadronic interactions [20–34]. The successful description of pp collisions by Monte Carlo (MC) generators relies on the precise modelling of UE [19].

As mentioned above, heavy ion-like effects are also observed in high-multiplicity pp collisions, and MPI and CR can produce collective-like effects. In the sake of establishing whether a small drop of strongly-interacting QGP is formed in pp collisions, one has to isolate high-multiplicity pp collisions with small impact parameter. Some approaches on the relative transverse activity classifier (R_{T}) [13, 35, 36] and flattenicity [37] have tried. In this thesis the R_{T} is discussed because it is the measurement that is reported. However, a separate chapter is included in this thesis to present the phenomenological studies on flattenicity.

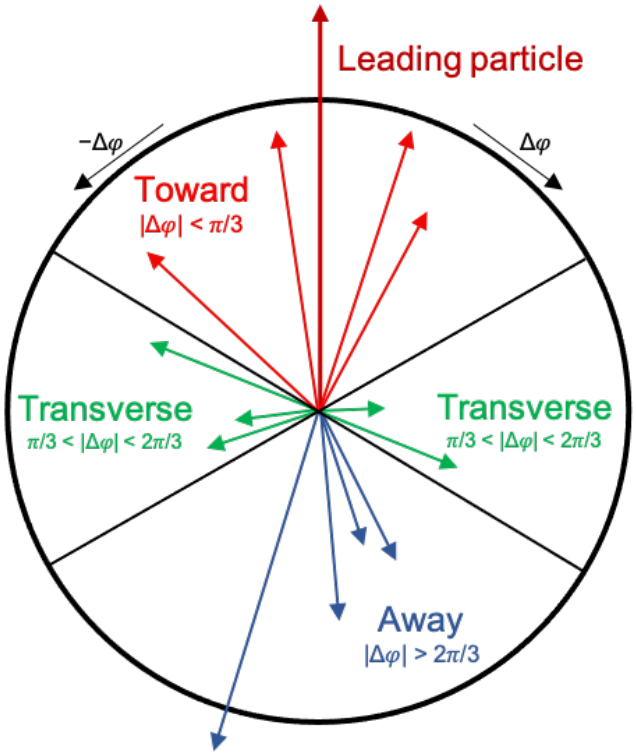

图 1.7: Schematic representation of the toward, transverse, and away regions in the azimuthal plane with respect to the leading particle, i.e. the particle with the highest p_{T} in the event. Figure taken from Ref. [38]

Experimentally, it is impossible to uniquely separate the UE from the event-by-event hard scattering process. However, the UA1 experiment in proton–antiproton collisions at CERN performed the first study of this kind by measuring the transverse energy density outside the leading jet, which is also known as jet pedestal region [39–41]. Another approach based on the definition of three distinct topological regions was introduced by the CDF Collaboration [42]. The three topological regions are defined from the angular difference between the trigger and associated particles, $|\Delta\varphi| = |\varphi^{\mathrm{assoc}} - \varphi^{\mathrm{trig}}|$, where φ^{trig} and φ^{assoc} refer to the value of the azimuthal angle for the trigger particle and for associated particles in the event, respectively [32]. The trigger particle is the one with the largest transverse momentum ($p_{\mathrm{T}}^{\mathrm{trig}}$) in the event, and the rest are termed as associated particles. The criteria for the definition of the different topological regions are depicted in Fig. 1.7. The toward region ($|\Delta\varphi| < \pi/3$) contains the main jet while the away region ($|\Delta\varphi| > 2\pi/3$) involves the fragments of the recoil jet. In general, these two regions are less sensitive to the UE. In contrast, the trans-

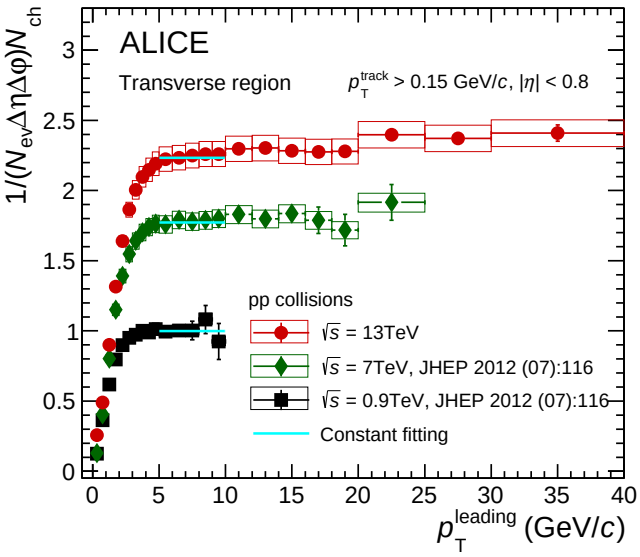

图 1.8: Comparison of number density as a function of $p_{\mathrm{T}}^{\mathrm{trig}}$ fort different centre-of-mass energies. Figure taken from Ref. [32]

verse region ($\pi/3 < |\Delta\varphi| < 2\pi/3$) is less affected by contributions from the hard scattering. Moreover, data show that the onset of the UE plateau in the transverse region is observed at $p_{\mathrm{T}}^{\mathrm{trig}} \sim 5\,\mathrm{GeV}/c$ [25, 32, 43]. This effect is illustrated in Fig. 1.8 that shows the charged particle density in the transverse region as a function of $p_{\mathrm{T}}^{\mathrm{trig}}$ in pp collisions at $\sqrt{s}$ =0.9, 7 and 13 TeV. The mean charged-particle multiplicity in the transverse region has little dependence on $p_{\mathrm{T}}^{\mathrm{trig}}$. Thus, it is safe if we classify the events with a trigger particle in the range $5 < p_{\mathrm{T}}^{\mathrm{trig}} < 40\,\mathrm{GeV}/c$ based on their per-event activity in the transverse region with respect to the mean:

$$R_{\mathrm{T}} = \frac{N_{\mathrm{ch}}^{\mathrm{T}}}{\langle N_{\mathrm{ch}}^{\mathrm{T}} \rangle}, \tag{1.3}$$

with $N_{\mathrm{ch}}^{\mathrm{T}}$ being the charged-particle multiplicity and $\langle N_{\mathrm{ch}}^{\mathrm{T}} \rangle$ being the mean charged-particle multiplicity in the transverse region.

Although the purpose of R_{T} is to quantify the UE activity of the events, it can still be influenced by jet fragments since the transverse region not only includes contributions from UE but also from ISR-FSR [42], especially for events with high R_{T} values in experiments with limited acceptance [17, 44]. In order to investigate the UE properties, a further treatment of the transverse region is implemented, where the transverse region is further divided in two sub-regions:

- transverse-I: $\pi/3 < \Delta\varphi < 2\pi/3$
- transverse-II: $\pi/3 < -\Delta\varphi < 2\pi/3$

The overall transverse region corresponds to the combined transverse-I and transverse-II regions. These two distinct regions are characterised in terms of their relative charged-particle multiplicities. Trans-max (trans-min) refers to the transverse region (I or II) with the larger (smaller) number of charged particles. Thus, the trans-max and trans-min regions are more sensitive to ISR-FSR and MPI, respectively. Using $N_{\rm ch}^{\rm Tmax}$ (the multiplicity in the trans-max region) and $N_{\rm ch}^{\rm Tmin}$ (the multiplicity in the trans-min region), instead of $N_{\rm ch}^{\rm T}$, we can also define the quantities $R_{\rm T}^{\rm max}$and $R_{\rm T}^{\rm min}$, respectively.

1.4 Koba-Nielsen-Olesen scaling

The Koba-Nielsen-Olesen (KNO) scaling was suggested in 1972 by Koba, Nielsen, and Olesen [45]. It is the hypothesis that at high $\sqrt{s}$ the probability distributions $P(n)$ of producing n particles in a certain collision process should exhibit the scaling relation

$$P(n) = \frac{1}{\langle n \rangle} \Psi \left(\frac{n}{\langle n \rangle} \right), \tag{1.4}$$

with $\langle n \rangle$ being the average multiplicity. This means that after scaling with $\langle n \rangle$, measured $P(n)$ at different energies collapse onto a universal function Ψ [46].

An analysis of the multiplicity distributions of pp and p$\bar{\rm p}$ data from $\sqrt{s} = 23.6\,\text{GeV}$ to $\sqrt{s} = 1.8\,\text{TeV}$ shows that the KNO scaling does not hold except for very central and small regions of phase space [47]. The scaling is broken due to fluctuations in impact parameter. Since with $R_{\rm T}$ to some extend central pp collisions are selected (this due to the selection on a high-$p_{\rm T}$ particle that biases the impact parameter of the collision), then the fluctuations on impact parameter are expected to be significantly reduced. To check whether the UE exhibits a KNO scaling, a MC simulation on the charged particles multiplicity distributions ($|\eta| < 2.5$, $p_{\rm T} > 0$) of the UE region (transverse region) was studied in KNO variables [36]. It was shown that the scaling held for pp collisions at the LHC energies for $0.5 < R_{\rm T} < 2.5$. The KNO-like scaling is expected in models which assume that a single pp collision is merely a superposition of a given number of elementary partonic collisions emitting particles independently [48]. Therefore, MPI is expected to produce such an effect.

In this thesis, a complementary study on KNO scaling of the UE activity in the transverse region using pp data at $\sqrt{s} = 2.76$, 5.02, 7, and 13 TeV with ALICE detector is reported. Furthermore, the study is also extended to the trans-max and trans-min regions, investigating the impact of radiation (MPI) using $N_{\rm ch}^{\rm Tmax}$ ($N_{\rm ch}^{\rm Tmin}$) distributions. We also report the centre-of-mass energy dependence of the average multiplicity density in the transverse, especially for the trans-max and trans-min regions at higher LHC energies. On the other hand, to understand the production mechanism of particles in the three regions, the multiplicity distributions fitted with negative binomial distributions (NBD) are also discussed.

1.5 Negative Binomial Distributions

The Negative Binomial Distribution (NBD) [47] is defined as

$$P_{p,k}^{\rm NBD}(n) = \binom{n+k-1}{n} (1-p)^n \, p^k. \tag{1.5}$$

It gives the probability for n failures and $k-1$ successes in any order before the k'th success in a Bernoulli experiment with a success probability p. The NBD is a Poisson distribution for $k^{-1} \to 0$ and a geometrical distribution for $k = 1$. For negative integer k and $\langle n \rangle \leq -k$ the distribution is a binomial distribution where $-k$ is the number of trials and $-\langle n \rangle / k$ the success probability. The continuation to negative integer k is performed by writing the binomial in terms of the Γ function and using the equation $\Gamma(x+1) = x\Gamma(x)$:

$$\begin{aligned} \binom{n+k-1}{n} &= \frac{(n+k-1)!}{n!(k-1)!} = \frac{\Gamma(n+k)}{\Gamma(k)\Gamma(n+1)} \\ &= \frac{(n+k-1)(n+k-2)\cdot \ldots \cdot k}{\Gamma(n+1)} \end{aligned} \tag{1.6}$$

The mean of the distribution $\langle n \rangle$ is related to p by $p^{-1} = 1 + \langle n \rangle / k$. This leads to the form of the NBD that is commonly used to describe multiplicity distributions [49–51]:

$$\begin{aligned} P_{\rm NBD}(n) &= \frac{\Gamma(n+k)}{\Gamma(k)\Gamma(n+1)} \left(\frac{\langle n \rangle / k}{1 + \langle n \rangle / k} \right)^n \frac{1}{(1 + \langle n \rangle / k)^k} \\ &= \frac{\Gamma(n+k)}{\Gamma(k)\Gamma(n+1)} \left(\frac{\langle n \rangle}{k + \langle n \rangle} \right)^n \left(\frac{k}{k + \langle n \rangle} \right)^k. \end{aligned} \tag{1.7}$$

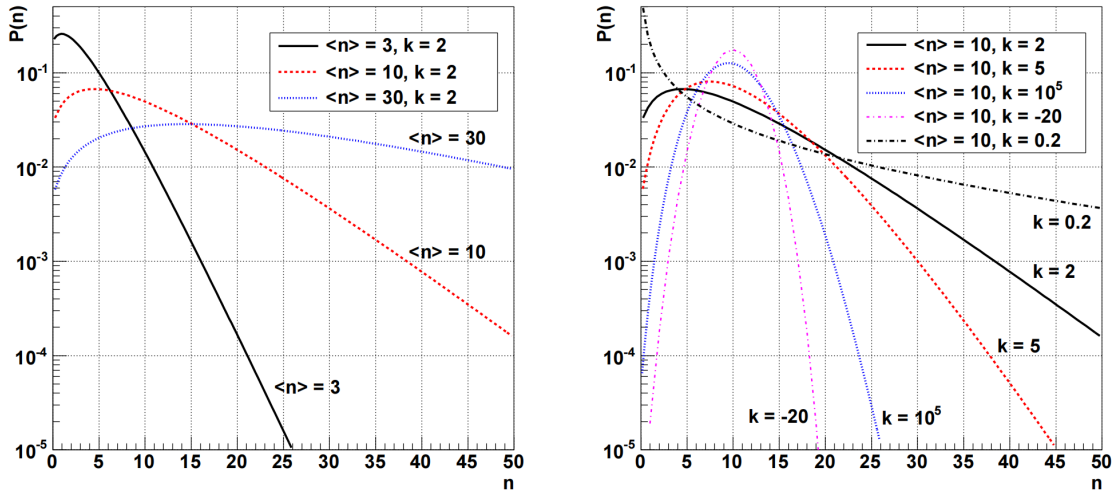

图 1.9: Examples of negative binomial distributions. Figure taken from Ref. [47]

Figure 1.9 shows normalised NBDs for different sets of parameters. NBDs for values of k that lead to characteristic shapes are also shown: the case of a large k where the distribution approaches a Poisson distribution is shown, the case with a negative integer k where the function becomes binomial, and the case of k being positive and smaller than unity.

UA5 found that multiplicity distributions up to $\sqrt{s} = 540\,\text{GeV}$ could be well described by a single NBD. At LHC energies, the multiplicity distributions of primary charged particles, produced in pp collision for INEL>0 events (events with at least one charged particle in the pseudorapidity interval $|\eta| < 1$), concluded that at $\sqrt{s} = 0.9\,\text{TeV}$ multiplicity distributions, of which no shoulder structure at high multiplicities was observed, could be also described by a single NBD within uncertainties, seen in Fig. 1.10. However, above 2 TeV, a shoulder structure at high multiplicities was observed in multiplicity distributions, which could no longer be represented by a single NBD. Instead, a double NBD gave a good representation of the data in Ref. [51]. Inspired by Giovannini and Ugoccioni [52], the two NBD-shaped components are needed to describe the soft (e.g. diffractive physics) and hard components of the sample. They can be understood as events with and without parton-parton scatterings, respectively. Therefore, we are interested in the effect of fitting charged-particle multiplicity distributions in the transverse, trans-max, and trans-min regions with NBD, especially for the latter two regions.

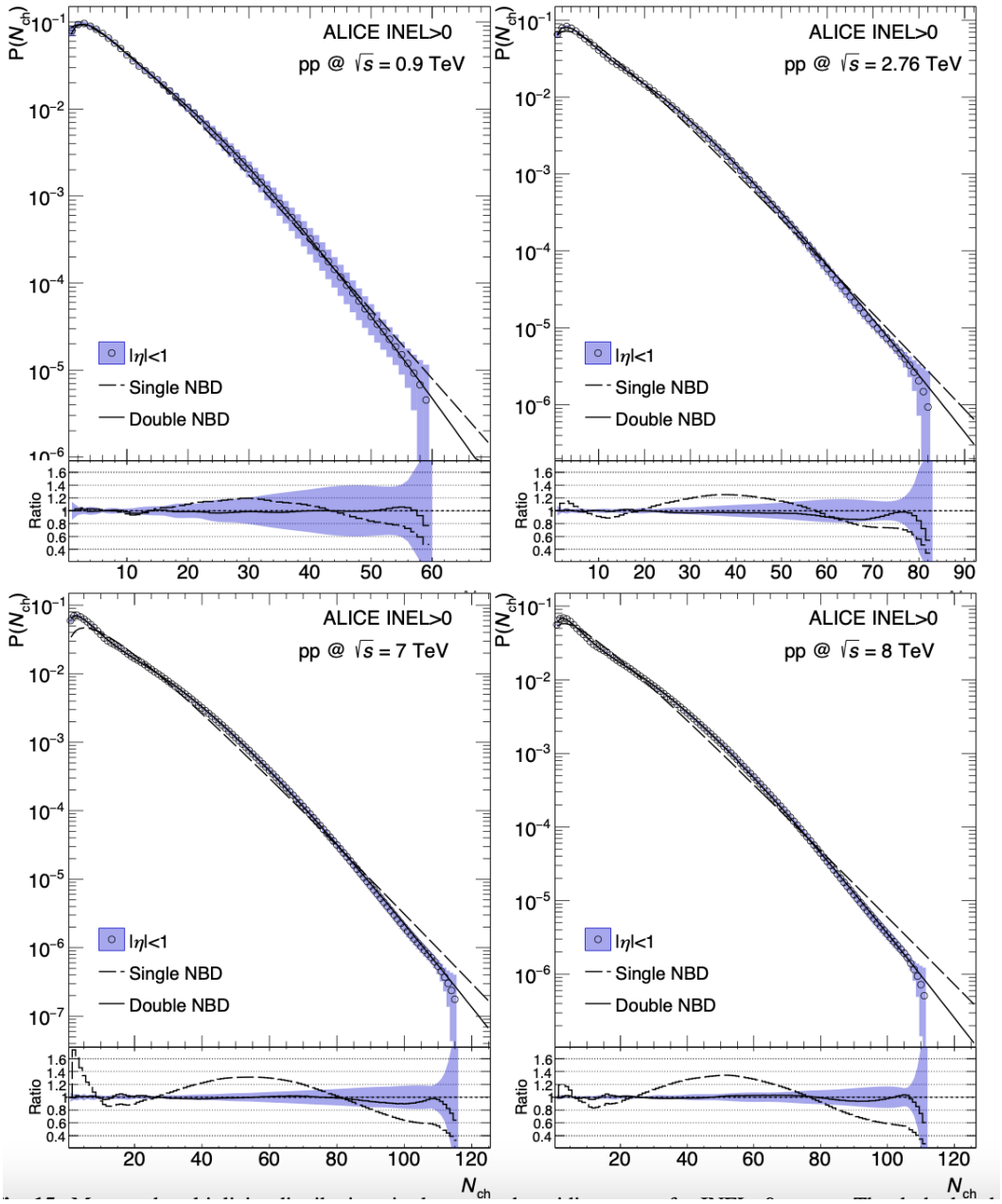

图 1.10: Measured multiplicity distributions in three pseudorapidity ranges for INEL>0 events. The dashed lines (solid lines) show the single NBD fits (double NBD fits). (a) data at $\sqrt{s} = 0.9\,\text{TeV}$ (upper left); (b) data at $\sqrt{s} = 2.76\,\text{TeV}$ (upper right); (c) data at $\sqrt{s} = 7\,\text{TeV}$ (bottom left); (d) data at $\sqrt{s} = 8\,\text{TeV}$ (bottom right). Ratios of data to the fits are also shown, with shaded areas representing combined systematic and statistical uncertainties. Figure taken from Ref. [51]

1.6 Monte Carlo event generators

The modern Monte Carlo event generators for simulation of particle collisions in collider experiments have been developed for several decades and encompass numerous physics mechanisms to describe huge amount of data. In particle physics, the outcome of a collision between two incoming particles, or of the isolated decay of a particle, is called an "event". At the most basic level, an event therefore consists of a number of outgoing particles such as might be recorded in a snapshot taken by an idealised detector, with conservation laws implying that the total summed energies and momenta of the final-state particles should match those of the initial state, as should any discrete quantum numbers that are conserved by the physics process(es) in question. Due to the randomness of quantum processes, the number of outgoing particles and their properties vary from event to event. The probability distributions for these properties can be inferred by studying an ensemble of events in data. Conversely, given a set of theoretically calculated (or modelled) probability distributions, it is possible to produce ensembles of simulated events to compare to data. A numerical algorithm that can produce (or "generate") random sequences of such simulated events, one after the other, is called an "event generator". The simulations can be based on known or hypothetical laws of nature. This allows for the exploration and comparison of competing paradigms, and studies of the sensitivity of proposed physical observables to the differences.

In this thesis, our results from pp collisions at LHC energies are compared to predictions from the PYTHIA 8 (Monash 2013 tune [53]) and EPOS tune LHC [54] MC event generators, hereinafter referred to as PYTHIA 8/Monash and EPOS LHC, respectively. The text below is fully based on the official documents of PYTHIA 8 [55] and EPOS [56].

PYTHIA 8. With this event generator we can simulate the particle production in high-energy collisions over a wide range of energy scales accessible to experiments. The simulation of hadronic collision is particularly challenging because the system is extremely complex, and no comprehensive theory exists currently that can predict event properties over such a wide energy range. In PYTHIA 8, a plethora of phenomena are factored into a number of components aiming at reducing the complexity of the system. A natural division for these components is a time-ordering or, equivalently, an energy or transverse momentum ordering, where the best understood physics is calculated at the shortest time scales and largest energies. The description of each component can be found in the official PYTHIA 8 documentation of Ref. [55] The ordering in time is not completely intuitive. Namely, time windows, centred on

a hard partonic interaction, are defined and then expanded forwards and backwards in time, introducing successive phenomena, until the event is left with a pair of incoming protons from beams and a number of outgoing particles. In momentum space, we normally speak of the "hardness" scale that characterises each (sub)process, and often use a measure of transverse momentum p_{T} to quantify this. In the hardness- or time-ordered picture, the components of a high-energy collision are:

- A hard scattering of two partons, one from each incoming hadron, into a few outgoing particles. The initial partons are selected using parton distribution functions for the incoming hadrons, and the kinematics of the outgoing particles are based on matrix elements calculated in perturbative QCD. Such calculations introduce a factorisation scale and a renormalisation scale. Partons with momenta below these scales are not included in the hard scattering, but will be introduced by other stages of the event generation. Hard-scattering predictions depend on a few, universal input parameters that are determined from data, such as the value of the strong coupling at the Z boson mass and parton distribution functions.

- The hard process may produce a set of short-lived resonances, such as Z or $W^{\pm}$ gauge bosons or top quarks, whose decay to normal particles has to be considered in close association with the hard process itself.

- Fixed-order radiative corrections may be incorporated via (combinations of) matrix-element corrections, matching, and/or merging strategies.

- Initial state radiation (ISR) of additional particles (partons, photons, and others) starting from the scattering initiators using numerical resummation of soft and collinear gluon emission. This (together with its final-state equivalent below) is commonly referred to as the parton shower.

- Final state radiation (FSR) of additional particles from the hard scattering itself and also from any resonance decays.

- In competition with ISR and FSR, further scattering processes between additional partons from the incoming beams may take place, in a phenomenon known as multiparton interactions (MPI). Due to the composite nature of hadrons, it is possible to have MPIs, i.e. events in which two or more distinct hard parton interactions occur simultaneously

in a single hadron-hadron collision. This mechanism is crucial for the precise description of data at the LHC energies.

- At some stage after the MPIs and perhaps before resonance decays, strings begin to form, as the non-perturbative limit of colour dipoles. These dipoles, however, are typically defined by colour connections. The associated colour-space ambiguities can be modelled via Colour Reconnection (CR). It is also possible that long-range dynamical interactions could physically alter the colour flow and/or change the configuration of the expanding strings before they fragment. Depending on the characteristic timescales involved (often not specified explicitly in simple CR models), such effects may also be referred to as colour reconnections, but could also be referred to as string interactions. Color reconnection has been found to produce collectivity-like effects in pp collisions with an active MPI environment [12].

- The strong interaction now results in the confinement of QCD partons into colour-singlet subsystems known as strings or, in small-mass limiting cases, clusters. What is currently left of the incoming hadron constituents are combined into beam remnants.

- The strings fragment into hadrons based on the Lund string model. Optionally, effects of overlapping strings may be taken into account, e.g. by collecting them into so-called "ropes" and/or allowing interactions between them.

- Identical particles that are close in phase space may exhibit Bose-Einstein enhancements (for integer-spin particles) or Fermi-Dirac suppressions (for half-integer-spin particles).

- Unstable hadrons produced in the fragmentation process decay into other particles until only stable particles remain (with some user flexibility to define what is stable).

- In densely populated regions of phase space, the produced particles may rescatter, re-annihilate, and/or recombine with one another.

EPOS LHC. The main difference of this model with respect to PYTHIA 8 is that includes a complete chain of possible hadronic phase as used in heavy-ion collisions aiming at improving the description of minimum bias p-p data at the LHC. Figure 1.11 shows a sketch of the space-time evolution of the particle production in pp collisions for two cases: the standard approach like in PYTHIA 8 and the more complete treatment used in EPOS LHC [54].

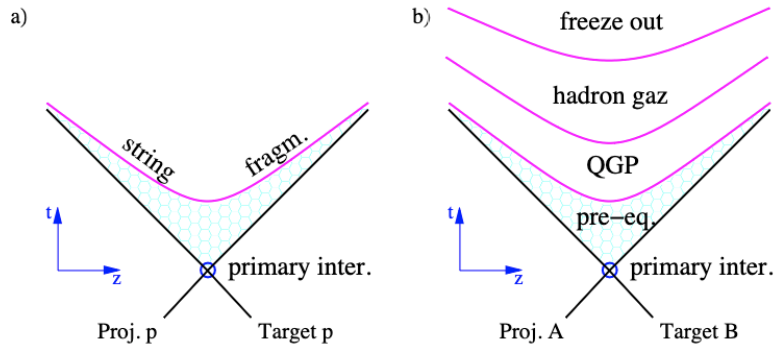

图 1.11: Space-time evolution of the particle production in pp (left) and heavy-ion collisions (rigth). The lines (hyperbolas) represent particles with the same proper time. Figure taken from Ref. [54]

EPOS LHC is based on the Parton-Based Gribov Regge Theory [57] developed for NEXUS, which was based on the VENUS model [58] for soft interactions and the QGSJET model [59] for the semi-hard scattering. It can be used to simulate pp, p–A, and A–A collisions. An elementary scattering corresponds to a parton ladder, containing a hard scattering which is calculated based on pQCD, including ISR-FSR. Parton ladders that are formed in parallel to each other share the total collision energy leading to consistent treatment of energy conservation in hadronic collisions. String hadronisation in EPOS is developed according with the local density of the string segments per unit volume relative to a critical-density parameter. Event-by-event, string segments in low-density regions hadronise normally and independently, creating the so-called “corona”, while string segments in high-density regions are used to create a “core” with collective expansion causing the radial and longitudinal flow effects. The EPOS LHC tune considered here is based on a dedicated parameter set used to describe data from different centre-of-mass energies and collision systems at the LHC.

第 2 章　ALICE experiment

ALICE (A Large Ion Collider Experiment) [60,61] is a general-purpose heavy-ion detector at the CERN LHC that focuses on QCD, the strong-interaction sector of the Standard Model. It is designed to address the physics of hot dense matter at extreme energy density and extreme temperature conditions attained in ultra-relativistic nucleus-nucleus collisions. It enables to comprehensively study hadrons, electrons, muons, and photons generated in heavy-ion collisions (Pb–Pb). The physics programme also includes collisions of lighter ions, in order to vary the energy density and interaction volume, as well as dedicated proton-nucleus and proton-proton (pp) runs. Data taking during pp runs at the top LHC energy has provided reference data for the heavy-ion analysis and has been utilised to explore areas where ALICE complements the other detectors at the LHC.

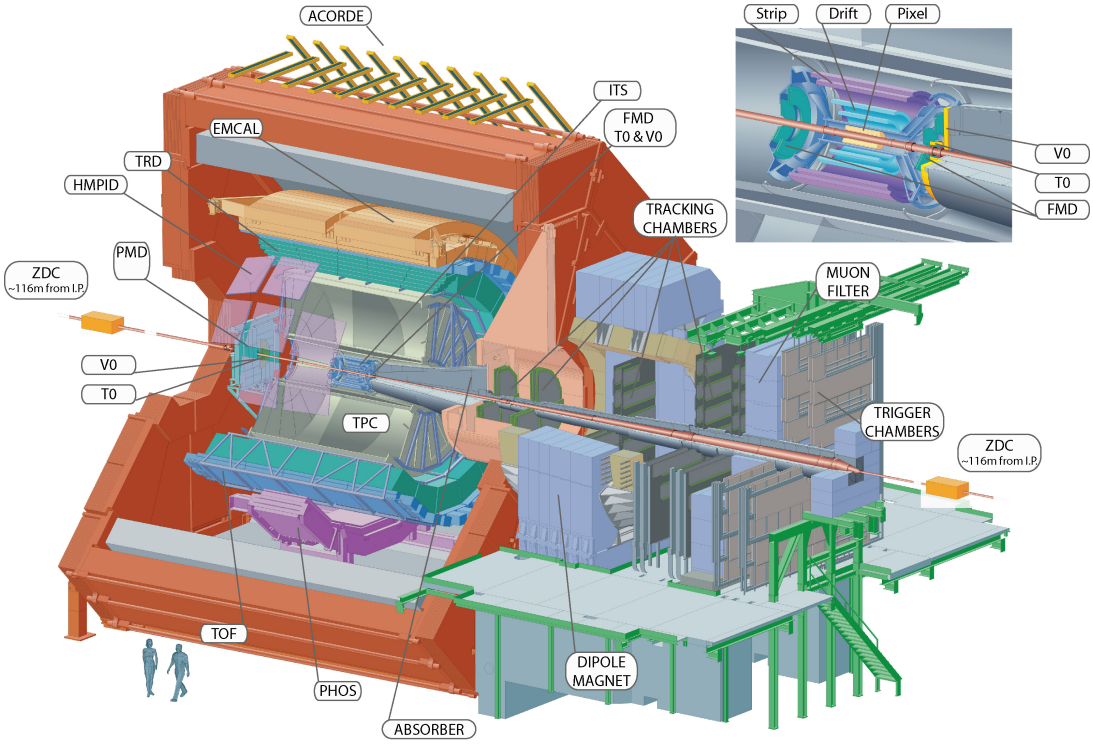

图 2.1: Layout of the ALICE detector during the LHC runs 1 and 2.

The ALICE apparatus is located at the so-called point 2 (IP2) of the LHC. ALICE is optimised for nuclear collisions and therefore requires a reduced luminosity in pp interactions at IP2. During the LHC Run 1 ALICE could operate at around 700 kHz, which is the max-

imum pp interaction rate at which all ALICE detectors can be safely operated. The typical luminosity values for the ALICE pp data taking range from $L \approx 10^{29}\,\mathrm{s}^{-1}\mathrm{cm}^{-2}$ (during minimum bias data taking) to $L \approx 10^{31}\,\mathrm{s}^{-1}\mathrm{cm}^{-2}$ (when accumulating rare triggers). The average number of interactions per bunch crossing (μ) was found between 0.05 to 0.3. The impact of pileup in the analyses presented in this thesis were evaluated and was found to be negligible.

Figure 2.1 shows the general layout of the ALICE detector during the LHC runs 1 and 2. ALICE consists of the three components presented below. Details about the detectors relevant for this work are also introduced in separated subsections.

- **Central detectors.** It consists of the following subdetectors: Inner Tracking System (ITS), Time-Projection Chamber (TPC), Transition Radiation Detector (TRD), Time-Of-Flight (TOF) detector, High-Momentum Particle Identification Detector (HMPID), PHOton Spectrometer (PHOS), and ElectroMagnetic CALorimeter (EMCal). They cover polar angles from 45° to 135° and are embedded in a large solenoid magnet which produce a magnetic field of 0.5 T along the beam axis.

- **Forward detectors.** The Zero Degree Calorimeter (ZDC), Photon Multiplicity Detector (PMD), Forward Multiplicity Detector (FMD), V0 detector, and T0 detector; are located in the forward and backward pseudo-rapidity regions for global event characterisation and triggering.

- **Muon spectrometer.** It is designed to detect muons in the polar angular interval $171° - 178°$. This interval, corresponding to the pseudorapidity interval of $-4.0 \leq \eta \leq -2.5$, is determined by considering acceptance and detector cost. The spectrometer is comprised of five components: a passive front absorber designed to capture hadrons and photons originating from the interaction vertex; a high-granularity tracking system consisting of 10 detection planes; a large dipole magnet; a passive muon-filter wall, followed by four planes of trigger chambers; and an inner beam shield intended to prevent the chambers from primary and secondary particles generated at high rapidities.

In this thesis, we used the following detectors for triggering, event characterisation and tracking.

2.1 Inner Tracking System

The main tasks of the ITS [62] are:

- Reconstruct the primary vertex with a position resolution better than 100 μm.
- Reconstruct the secondary vertices from the decays of hyperons, D and B mesons.
- Track and identify particles with momentum smaller than 200 MeV/c.
- Optimise the momentum and angular resolution for tracks reconstructed using the TPC.

The ITS (Fig. 2.2), located at radii from 4 to 43 cm, is comprised of six cylindrical layers of silicon detectors. It is designed, based on the length of the interaction diamond ($\pm 1\sigma$, i.e. ± 5.3 cm along the beam direction), to cover the rapidity interval of $|\eta| < 0.9$ for all vertices. In the seek of efficiently detecting tracks and high impact-parameter resolution, it optimised the number, position and segmentation of the layers. Especially, the outer radius is quantified with the requirement of matching tracks between ITS and TPC, and the inner radius is constrained by the size of the beam pipe. To ensure the continuous measurement of charged-particle multiplicity from the ITS to the FMD, the first layer must have a wider pseudo-rapidity coverage ($|\eta| < 1.98$).

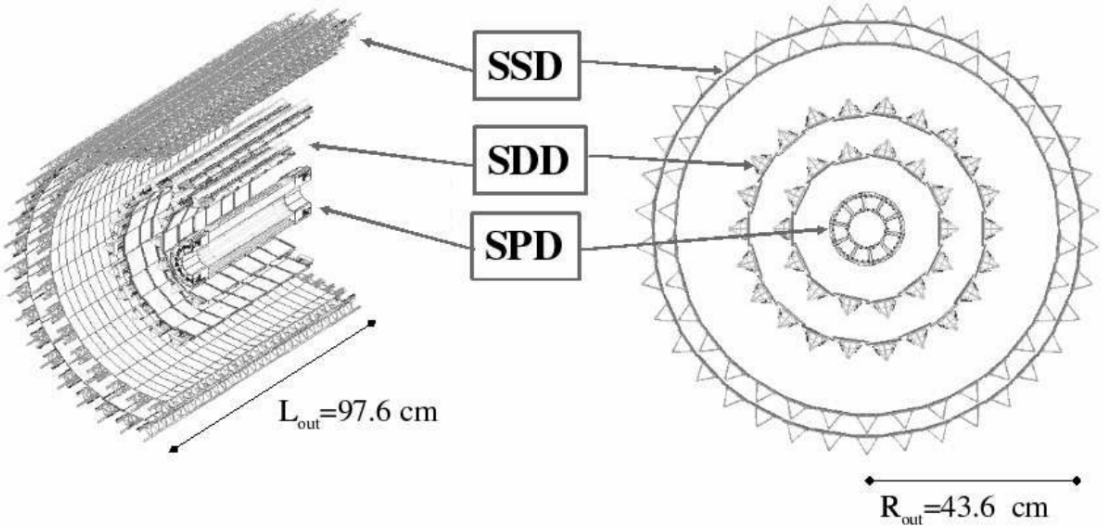

图 2.2: The layout of the Inner Tracking System. Figure taken from [61].

Because of the high particle density expected in heavy-ion collisions at LHC, and in order to achieve the required impact parameter resolution, Silicon Pixel Detectors (SPD) have been chosen for the innermost two layers, and Silicon Drift Detectors (SDD) for the following two layers. The two outer layers, where the track density was below one particle per cm^2, are

equipped with double-sided Silicon micro-Strip Detectors (SSD). The four outer layers have analogue readout and therefore can be used for particle identification via $\mathrm{d}E/\mathrm{d}x$ measurement in the non-relativistic ($1/\beta^2$) region. The analogue readout has a dynamic range large enough to provide the $\mathrm{d}E/\mathrm{d}x$ measurement for low-momentum, highly ionising particles, down to the lowest momentum at which tracks can still be reconstructed. This feature gives the ITS stand-alone capability as a low-p_{T} particle spectrometer.

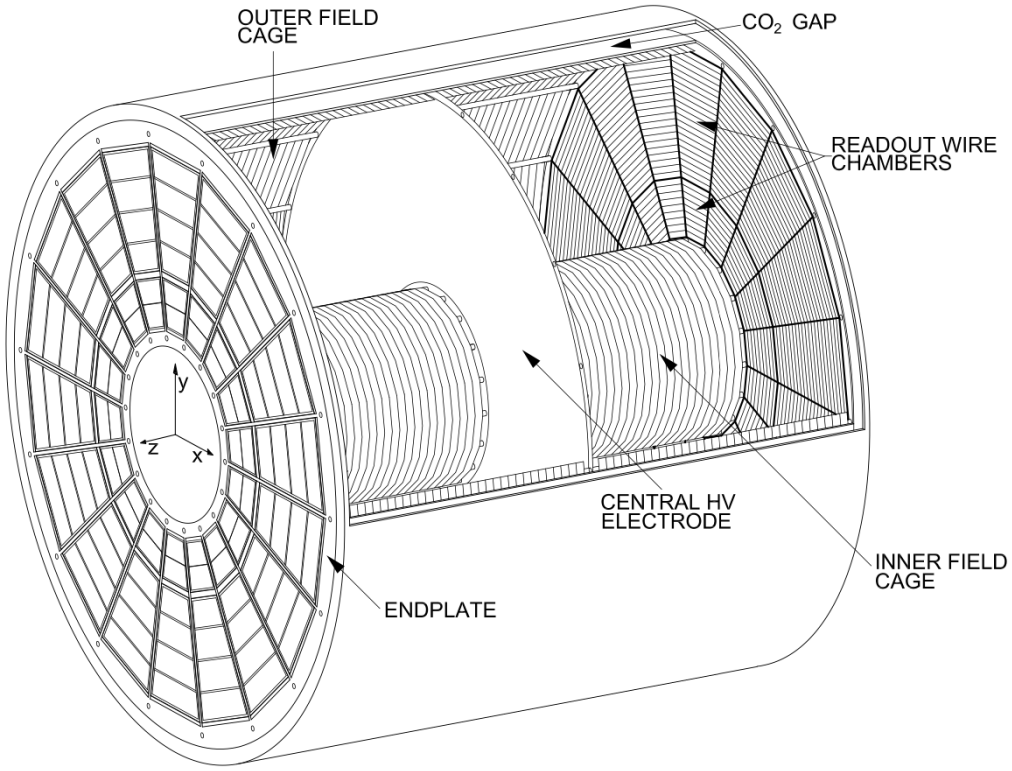

图 2.3: The layout of the Time-Projection Chamber. Figure taken from [63].

2.2 Time-Projection Chamber

The TPC [64] is the main tracking detector of the central barrel and is optimised to provide, together with the other central barrel detectors, charged-particle momentum measurements with good two-track separation, particle identification, and vertex determination. In addition, data from the central barrel detectors are used to generate a fast online High-Level Trigger (HLT) for the selection of low-cross section signals. The phase space covered

by the TPC in pseudorapidity is $|\eta| < 0.9$ for tracks with full radial track length (matches in ITS, TRD, and TOF detectors); for reduced track length (at reduced momentum resolution), an acceptance up to about $|\eta| = 1.5$ is accessible. The TPC covers the full azimuth (with the exception of the dead zones). A large p_{T} range is covered from low p_{T} of about 0.1 GeV/c up to 100 GeV/c with good momentum resolution.

The TPC (Fig. 2.3) is cylindrical in shape; the active volume has an inner radius of about 85 cm, an outer radius of about 250 cm, and an overall length along the beam direction of 500 cm. The detector consists of a large cylindrical field cage filled with 90 m^3 of $\mathrm{Ne/CO_2/N_2}$ (90/10/5) and is segmented into two drift regions by the central electrode located at its axial centre. The field cage ensures a uniform electric field along the z-axis. Each of the two end plates is divided into 18 sectors, each holding one Inner ReadOut Chamber (IROC) and one Outer ReadOut Chamber (OROC). In total, the TPC readout is based on 36 IROCs and 36 OROCs. The TPC readout chambers have 159 tangential pad rows and thus a charged particle can, ideally, produce 159 clusters within the TPC volume. Multi-wire proportional chambers with cathode pad readout are mounted into 18 trapezoidal sectors at each end plate.

Track reconstruction is implemented in three stages, using the so called inward-outward-inward scheme [65]. In the first stage, track finding starts from the TPC and begins at a large radius. Two procedures are considered to build track seeds : the one is required with two clusters in TPC as well as the vertex point, another one has three TPC clusters but without the constrain in vertex point. For each procedure, along each step of seeds propagating inward, the nearest cluster will be assigned as the updated seed only if the nearest one satisfies a proximity cut. However, the clusters can be multiply used by distinct seeds, leading to the repeated reconstruction of the same physical track. Therefore, to avoid this, one performs a special algorithm to seek track pairs for which the faction of shared clusters should exceed a limit (25% to 50%). Subsequently, the worse between two tracks is rejected based on the quantities related with clusters, i.e., number of clusters, density of clusters, and momentum. Moreover, a track can be accepted only if the number of clusters in this track is not less than 20 (the maximum possible number of clusters is 159) and the number of missing clusters in this track does not exceed 50% at a given track position. These clusters keep propagating inward to the inner radius of TPC. The track transverse momentum p_{T} dependence of TPC track efficiency, referring to the ratio of reconstructed tracks to generated particles in MC simulation, is seen in Fig. 2.4. There is a drop at low p_{T} ($<$0.5 GeV/c) due to energy loss in the detector material, whereas, at higher p_{T} the efficiency is influenced by missing clusters in

tracks which are projected onto the dead zone between readout sectors. And the efficiency is nearly not related with the detector occupancy.

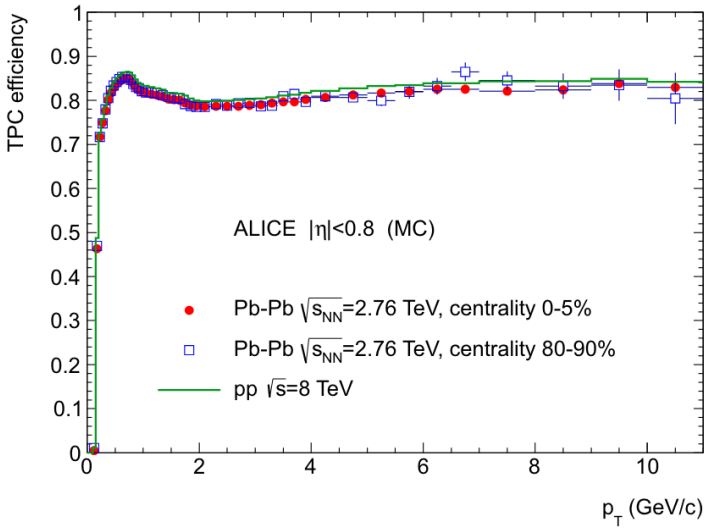

图 2.4: TPC track efficiency for pp and Pb–Pb collisions. Figure taken from [65].

Then the reconstructed tracks in TPC are propagated inward to the outermost layer of ITS and are used as seeds to seek tracks in ITS. As seeds propagating inward, at each layer within ITS, they are renew based on all clusters within a proximity cut, in which the relevant positions and errors are considered. A new seed is saved by the result in each updating. Due to the low detection efficiency, if seeds are not updated at a given layer, they are still used to further seek tracks. In this case, the χ^2 of these seeds consider a penalty factor due to a missing cluster (unless the seed extrapolation is in the dead zone of this layer). Therefore, in ITS each track hypothesis tree is produced by a TPC track. This seeding procedure also takes into account two passes like in TPC: with and without the constraint of vertex point. Once the candidates of the complete track hypothesis tree for the TPC track are built, they are sorted based on the decreased χ^2. For each tree, the candidate with the highest quality can be determined. It can then be further checked whether there are shared clusters among these candidates. If shared clusters are present, the alternative candidates are considered in the relevant trees. In the case of failing to fully distinguish between two tracks, the worse of the two tracks is tagged with a special label which is used to include clusters that might be incorrectly matched ("fake"). Eventually, the reconstructed event contains the highest quality candidate from each hypothesis tree. Figure 2.5 shows the ITS-TPC matching efficiency with respect to p_{T} for pp and Pb–Pb collisions, considering distinct requirements associated with ITS.

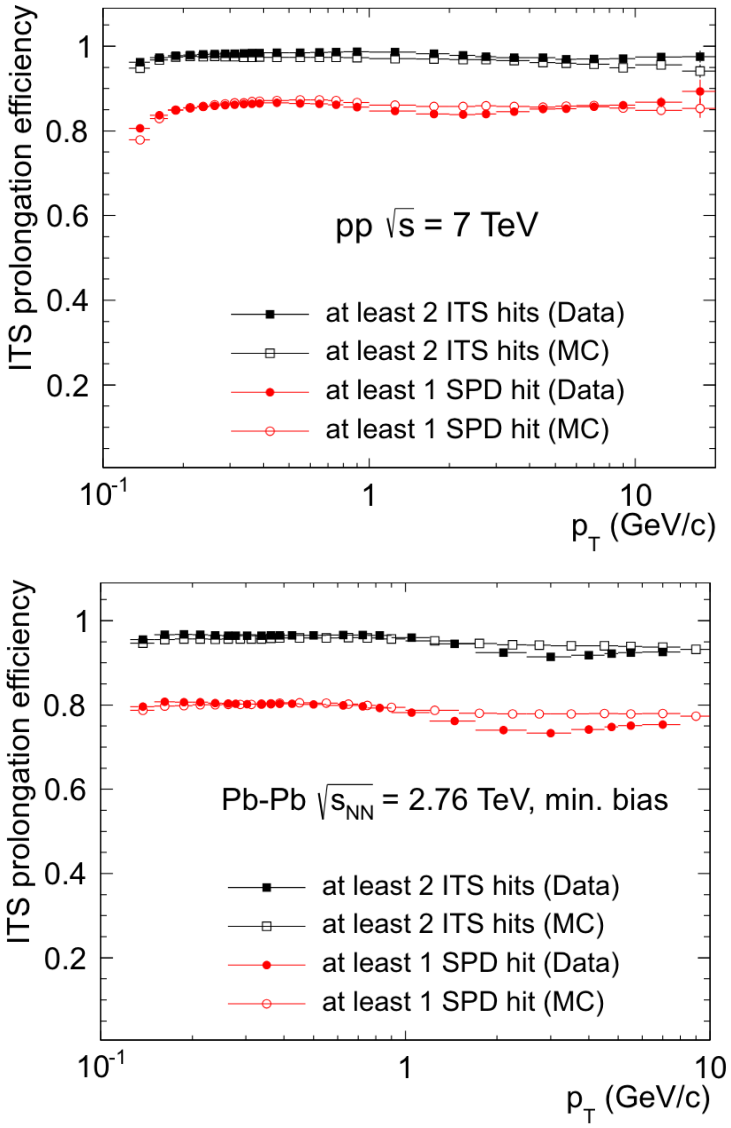

图 2.5: ITS-TPC matching efficiency for data (full markers) and MC (open markers) in pp (top) and Pb–Pb (bottom) collisions. Figure taken from [65].

As mentioned above, Fig 2.4 indicates that in TPC the tracking efficiency steeply decreases at low p_{T}. For pions and protons, the cutoff are around 200 MeV/c and 400 MeV/c, respectively, which results from energy loss and multiple scattering in the detector material. Consequently, those clusters, which are not utilised in ITS-TPC tracks, are proposed to apply with the standalone ITS reconstruction. The helical seeds are built based on two clusters from the three innermost layers of ITS together with the primary vertex constrain. As the seed propagating to other layers, it is renew according to clusters within a proximity cut.

The accumulation of the number of seed-completion hypotheses depends on each matching cluster. In the last step of seed processing, a Kalman filter is used to refit all hypotheses, the track reaching the best fit χ^2 is accepted, and the clusters in the track can be removed from further search. For the sake of rising the tracking efficiency, the full procedure is repeated several times, gradually opening the seed completion road widths. This algorithm allows to reconstruct track having low p_{T} values down to around $80\,\mathrm{MeV}/c$.

While finalising the reconstruction process in ITS, all of the tracks are extrapolated to the point of their nearest approach to the preliminary interaction vertex, and the outward propagation is followed, i.e., the beginning of the second stage. The Kalman filter refits the tracks along the outward direction utilising the clusters identified from the first stage. The integral of the track length, together with the flight time for different species of particles (e.g., electrons, muons, pions, kaons, protons), at each outward step, are renew for the followed particle identification with TOF. If the track accesses the TRD at a radius of 290 cm, it is matched to a TRD tracklet (track segment within a layer TRD layer) in each of the six layers in TRD. This is also the case in the TOF detector, the tracks are matched with corresponding TOF clusters while they access the TOF. At this point, the integral of the track length and the time-of-flight computation are terminated. Afterwards, the tracks are further propagated to EMCal, PHOS, and HMPID for matching with signals in these external detectors. The tracks continue to propagate outward the EMCal, PHOS, and HMPID detectors in order to be matched with signals in these external devices. The detectors located beyond the radius of the TPC are presently not used for updating the measured track kinematics, instead, their data retain in the track object is used for particle identification.

In the last stage, all tracks are propagated inward, beginning at the outer radius of the TPC. The tracks in both TPC and ITS detectors are refitted using the clusters that are previously identified, which determines the track's location, orientation, inverse curvature, and covariance matrix.

Most of tracks, that are reconstructed using the aforementioned inward-outward-inward scheme, are from the primary vertex, seen in Fig. 2.6. Secondary tracks, which are produced from decays and secondary interactions in the detector material, can be reduced even further by applying restrictions on the longitudinal and transverse distances of closest approach, denoted as d_0, to the primary vertex.

For identified ITS-TPC tracks, their resolution of the transverse distance to the primary vertex is reported for pp collisions, along with a comparison to simulation results, seen in the

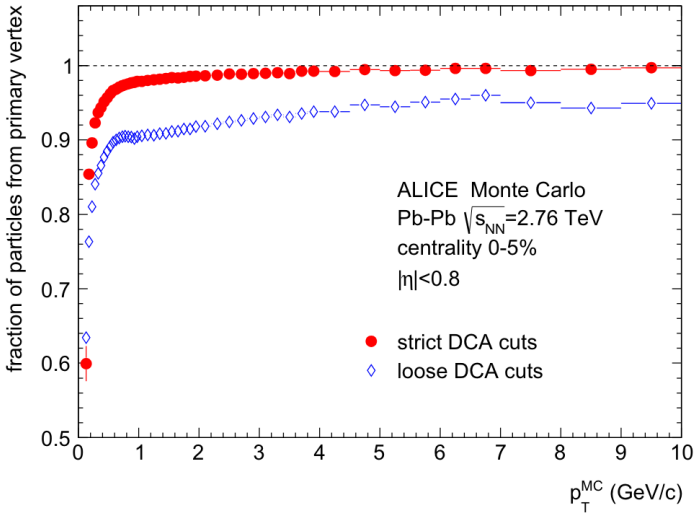

图 2.6: Fraction of reconstructed tracks coming from the primary interaction vertex. Two sets of cuts on the track distance of closest approach (d_0) to the primary vertex are shown: "loose" with $|d_{0,z}| < 3\,\text{cm}$, $d_{0,xy} < 3\,\text{cm}$, and "strict" with $|d_{0,z}| < 2\,\text{cm}$, $d_{0,xy} < (0.0182 + 0.0350\,\text{GeV}/c\,p_T^{-1})\,\text{cm}$. Figure taken from [65].

top panel of Fig. 2.7. The contribution arising from vertex resolution is not deducted. In the case of all charged particle tracks, such resolution is discussed for three different colliding systems, extending to a higher p_T range, seen in the bottom panel of Fig. 2.7. In the heavier systems, a better resolution is observed, which is attributed to that the primary vertex is more precisely identified at higher multiplicities.

Fig. 2.8 shows the p_T resolution, obtained from the associated track covariance matrix, for both TPC-standalone tracks and ITS-TPC combined tracks, as well as shows the effect of the tracks constrained to the primary vertex. The inverse-p_T resolution is given by the below relation according to the relative p_T resolution:

$$\frac{\sigma_{p_T}}{p_T} = p_T\,\sigma_{1/p_T}. \tag{2.1}$$

The plot shows the most progressive reconstruction approach that was utilised for the data collected during p–Pb run. Within the context of central Pb–Pb collisions, the p_T resolution was anticipated to decrease by around 10-15% at high p_T. This decrement was attributed to several factors, including the loss or diminution of clusters situated on the tails of ions, the overlap of their clusters, and fake clusters associated with the tracks.

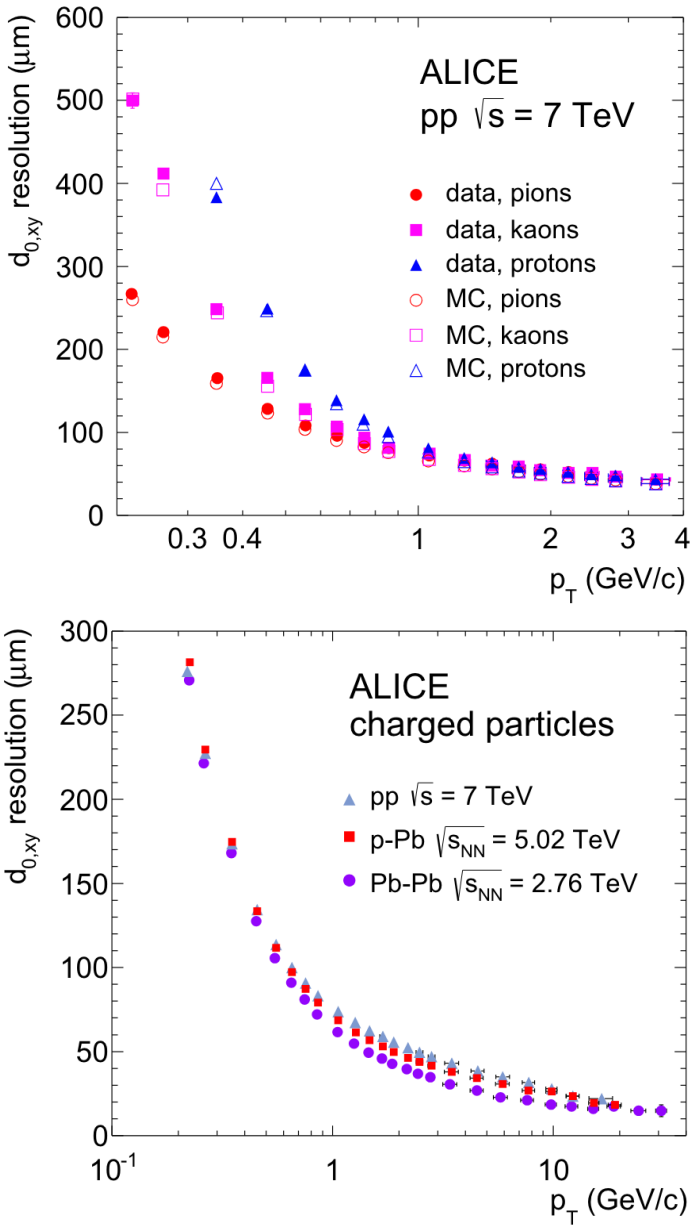

图 2.7: Resolution of the transverse distance to the primary vertex for identified particle global ITS-TPC tracks (top) and for all charged ITS-TPC tracks (bottom). Figure taken from [65].

Fig. 2.9 shows the invariant mass spectra of $\mu^+\mu^-$ and e^+e^- pairs in ultra-peripheral Pb–Pb collisions at $\sqrt{s_{\rm NN}} = 2.76\,\text{TeV}$, collaborating the mass resolution that can be achieved using ITS-TPC global tracks. At the J/Ψ peak the mass resolution is superior to 1%. The global ITS-TPC track reconstruction is hindered by gaps in the ITS acceptance, despite the fact that it offers the most accurate estimate of track parameters. Specifically, in the two SPD

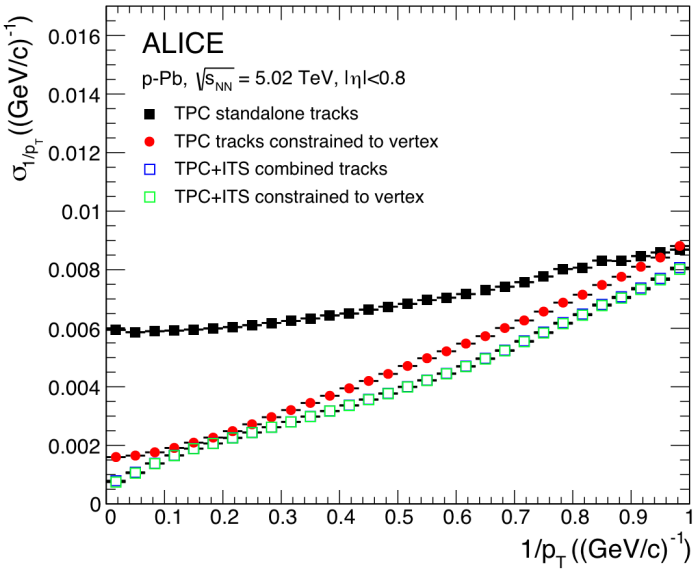

图 2.8: The p_{T} resolution for standalone TPC and ITS-TPC matched tracks with and without constraint to the vertex. The vertex constrain significantly improves the resolution of TPC standalone tracks. For ITS-TPC tracks, it has no effect (green and blue squares overlap). Figure taken from [65].

layers (the innermost layers in ITS), up to around 20% (30%) of the modules are not active in 2010 (2011). The inefficiency is decreased to around 5% in 2012 following the resolution of issues related to detector cooling. On the other hand, one can use track parameters that are fitted exclusively in TPC and restricted to the primary vertex in analyses requiring a uniform detector response. In this case, the p_{T} resolution of these tracks is similar to that of the global tracks for p_{T} values up to around 10 GeV/c, but it is remarkably poorer for higher p_{T} values, as indicated by the red full circles in Fig. 2.8.

Global tracks (ITS-TPC combined tracks) allow for a more precise determination of the interaction vertex compared to using only tracklets from SPD. To determine the approximate point of closest approach of validated tracks, the tracks are extrapolated to the point of closest approach to the nominal beam line, and far outliers are excluded. Following this, the precise vertex fit is carried out, utilising track weighting to minimise the impact of any remaining outliers [67]. To enhance the precision of the transverse vertex position in low-multiplicity events, the fit incorporates the nominal beam position as an independent measurement, with associated errors reflecting the transverse size of the luminous zone.

Regarding data-taking conditions in which a high pileup rate is anticipated, an improved

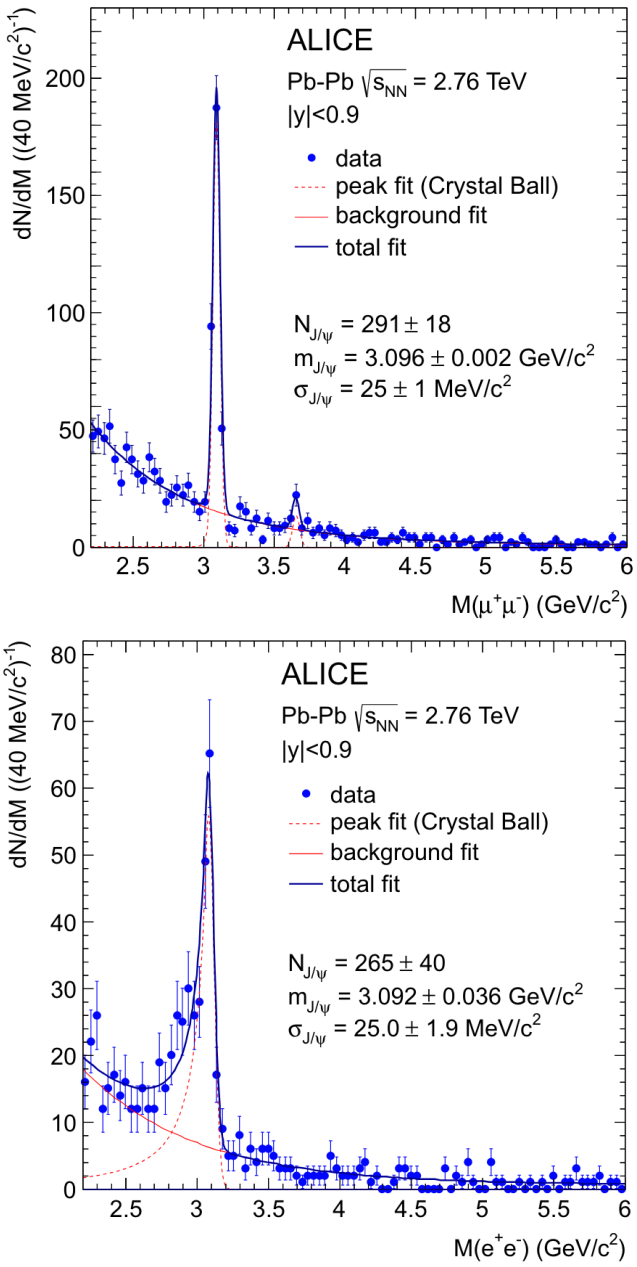

图 2.9: Invariant mass spectra of $\mu^+\mu^-$ and e^+e^- pairs in ultra-peripheral Pb–Pb collisions. The solid and dotted lines represent the background (exponential) and peak (Crystal Ball [66]) fit components, respectively. The bremsstrahlung tail in the e^+e^- spectrum is reproduced in simulation. Figure taken from [65].

vertex-finding technique based on the one described in Ref. [68], is employed. The method is based on a iteration process of vertex finding and fitting, utilising Tukey bisquare weights [69]

to reduce the impact of outliers. The inflation of the scaling factor, which is implemented to the errors on the tracks extrapolated to the nominal beam axis, is halted until an initial vertex position is found with at least two tracks that have non-zero weights. After performing the fit, which is similar to that in Ref. [67] but incorporating these weights, the scaling factor is reduced as the fitted vertex approaches its real position. The iterations do not stop unless there is less than 10 µm between the vertices that has been fitted consecutively. If, at this stage, the scaling factor remained remarkably more than unity or the maximum iteration count is achieved, the vertex candidate is discarded, and the search is restarted with a distinct seeding position. Otherwise, the ultimate fitting procedure for the weighted tracks is finalised, followed by the validation of the vertex, tracks that possess non-zero weights are excused from the pool, and subsequent vertex searches are carried out within the same event. While no additional vertices are identified during the scan along the beam direction, the algorithm halts. In the sake of reducing the risk of incorporating tracks from distinct bunch crossings into the same vertex, the tracks, contributed to the same vertex, are required with the same or an undefined bunch crossing. The relationship between tracks and bunch crossings is determined by utilising the temporal information obtained from the TOF detector. The left panel of Fig. 2.10 illustrates the assignment of bunch crossings to ITS-TPC tracks during a typical high-intensity pp run. An instance of identified pileup in a single event is displayed on the right panel of Fig. 2.10, which reports z-coordinate of the tracks' closest approach to the beam axis, while markers represent the positions of reconstructed vertices with their corresponding bunch crossings.

Figure 2.11 displays the x- and z-profiles of the luminous region acquired from the vertices reconstructed in both pp and Pb–Pb collisions. Figure 2.12 displays the transverse resolutions of the preliminary interaction vertices identified utilising the SPD, alongside the resolution of the final vertices determined with global tracks. As anticipated, the resolutions for both sets of vertices exhibit a proportional relationship with the square root of the number of contributing tracks.

2.3 V0 detector

The V0 detector [70] is a small angle detector consisting of two arrays of scintillator counters, called V0A and V0C (Fig. 2.13). The V0A detector is located 340 cm from the vertex on the side opposite to the muon spectrometer whereas V0C is fixed to the front face of the hadronic absorber, 90 cm from the vertex. They cover the pseudorapidity ranges

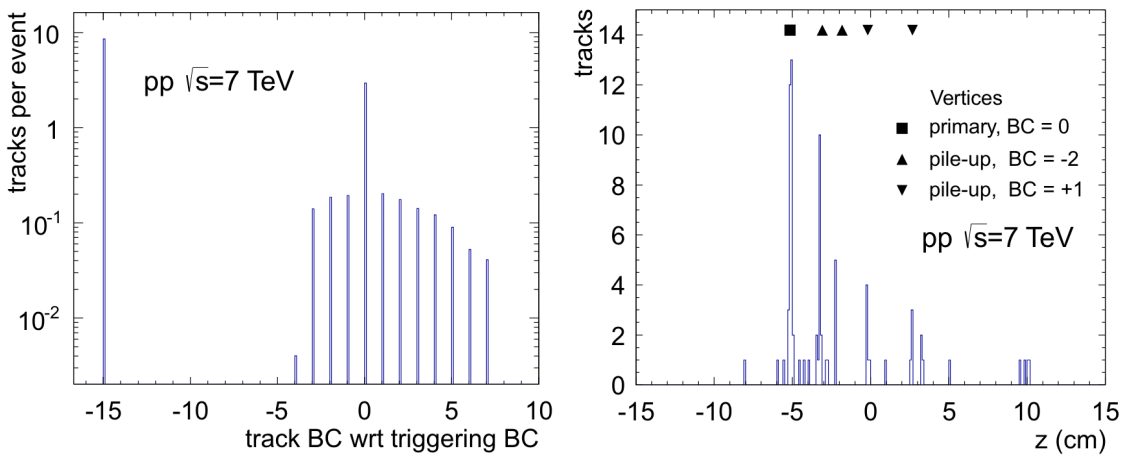

图 2.10: Left: Bunch crossing (BC) ID of tracks obtained from the comparison of time of flight measured in the TOF detector and expected from the track kinematics. The ID is defined with respect to the BC in which the triggering interaction took place. The peak at -15 corresponds to tracks not matched in TOF (mostly from the pileup in the TPC, outside of the TOF readout window of 500 ns). Right: z-coordinates of tracks' PCA to the beam axis in a single event with pileup; the positions of reconstructed vertices with attributed bunch crossings are shown by markers. Figure taken from [65].

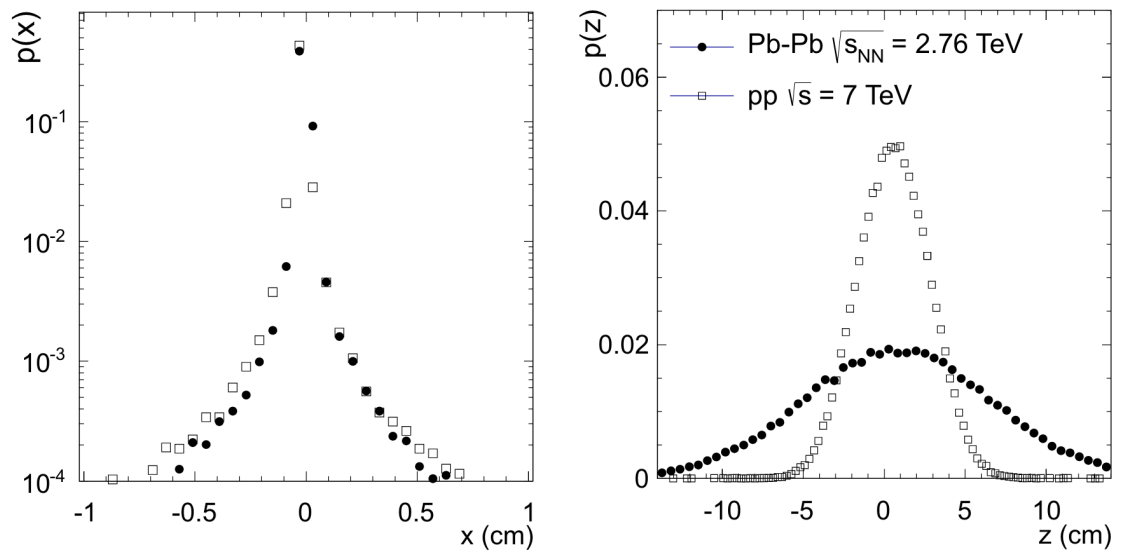

图 2.11: The x (left) and z (right) projections of the luminous region obtained from reconstructed vertices in pp and Pb–Pb collisions (folded with vertex resolution). Figure taken from [65].

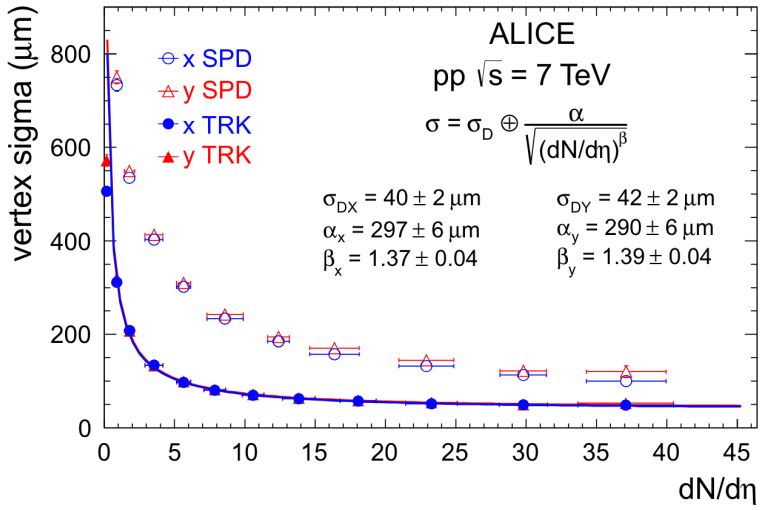

图 2.12: Transverse width of the final vertex distribution (solid points), decomposed into the finite size of the luminous region σ_D and the vertex resolution $\alpha/\sqrt{(\mathrm{d}N_{\mathrm{ch}}/\mathrm{d}_\eta)^\beta}$. For comparison, the widths of the preliminary (SPD) interaction vertices are shown as open points. Figure taken from [65].

$2.8 < \eta < 5.1$ (V0A) and $-3.7 < \eta < -1.7$ (V0C).

This detector has several functions. It provides minimum-bias triggers for the central barrel detectors in pp and A–A collisions. These triggers are given by particles originating from initial collisions and from secondary interactions in the vacuum chamber elements. The V0 is used to quantify the centrality of a collision based on the event multiplicity, due to the monotonic relationship between the number of particles registered on the V0 arrays and the number of primary emitted particles. The rough centrality triggers can be achieved by varying the number of fired counters and the total charge. There are three such triggers: the multiplicity trigger, the semi-central and central triggers.

In practice and during normal operation, both arrays are required (AND mode) to provide triggers, namely: Minimum Bias trigger (MB), Multiplicity Trigger (MT), semi-Central Trigger (CT1) and Central Trigger (CT2). An OR mode can also be adopted. In pp collisions, the efficiency for the detection of at least one charged particle detected in both sides is about 75% when no secondary particle is taken into account. It raises up to 84% when the environment effects are introduced [70, 71].

As mentioned above, the background estimation for pp data taking is performed with the V0 detector [65]. Given the asymmetric location of both V0 subdetectors, the signal arrival

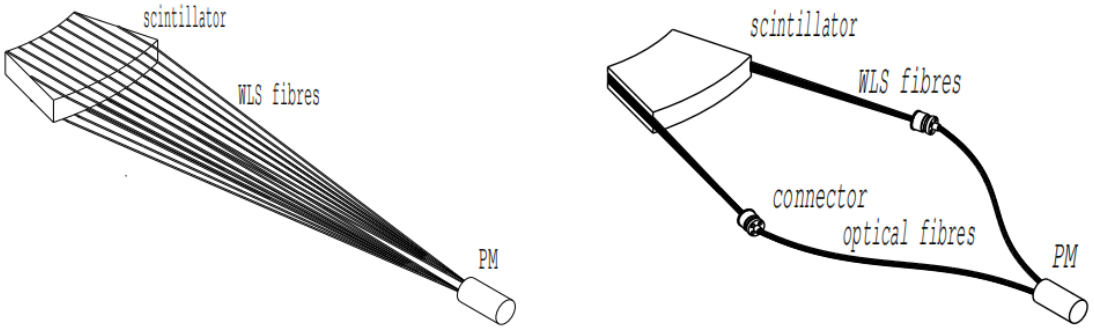

图 2.13: The Schematic design of the V0A (left) and V0C (right) detection elements. Figure taken from [61].

time in the two V0 subdetectors is used to discriminate collision events from background events originating from the passage of LHC beam particle 1 or beam particle 2. The background caused by one of the beams is produced upstream of the V0 on the side from which the beam arrives. It therefore yields an "early" signal when compared with the time corresponding to a collision in the nominal interaction point. The difference between the expected beam and background signals is about 22.6 ns in the A side and 6 ns in the C side. Figure 2.14 shows background events accumulate mainly in two peaks in the time sum – difference plane, well separated from the main (collision) peak.

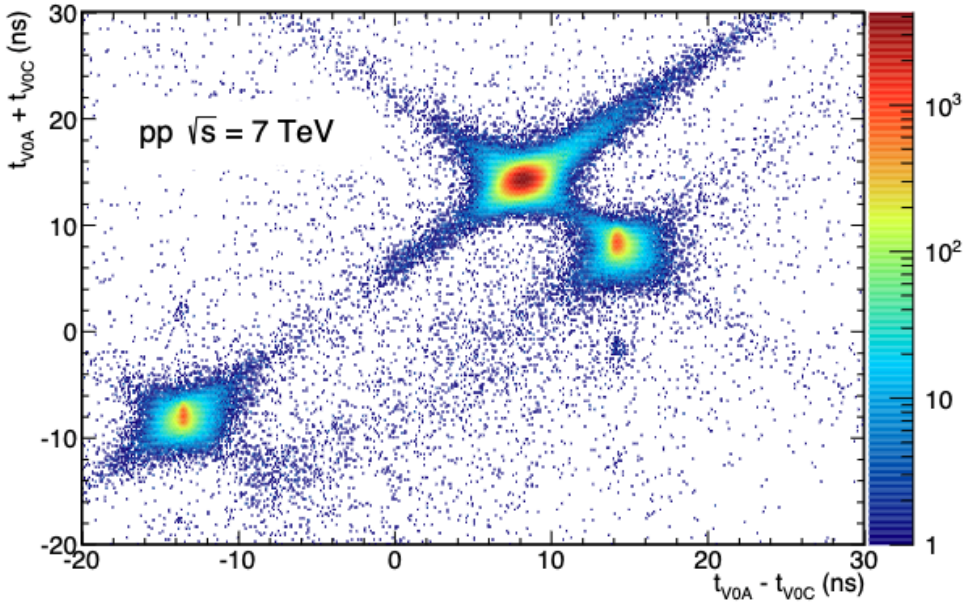

图 2.14: Correlation between the sum and difference of signal times in V0A and V0C. Figure taken from [65].

第 3 章 Data sample selection and analysis methods

3.1 Data samples

This work focuses on pp collisions at $\sqrt{s}$ = 2.76, 5.02, 7, and 13 TeV. The data were collected during the LHC runs 1 and 2, and reconstructed with the ALICE detector. For the sake of reproducibility of the results, all technical details like datasets, reconstruction passes, run list, etc., are listed below.

- The analysis for pp collisions at $\sqrt{s} = 2.76$ TeV used the following data.

  Dataset: Proton-proton collisions were collected in 2011 for a center-of-mass energy of 2.76 TeV. For ALICE readers interested in the reconstruction pass, the dataset is identified as LHC11a_pass4_with_SDD.

  Year of the data taking: 2011.

  Run list: 146746, 146747, 146748, 146801, 146802, 146803, 146804, 146805, 146806, 146807, 146817, 146824, 146856, 146858, 146859, 146860.

  MC production: The Monte Carlo production corresponding to this specific run is named as LHC12f1a_wSDD. The PYTHIA 8 event generator (version 8.145) was used to simulate minimum-bias pp collisions.

- The analysis for pp collisions at $\sqrt{s} = 5.02$ TeV used the following data.

  Dataset: The data were collected in 2015, for ALICE readers interested in the reconstruction pass, the dataset is identified as LHC15n_pass4.

  Year of the data taking: 2015.

  Run list: 244628, 244627, 244626, 244619, 244618, 244617, 244542, 244540, 244531, 244484, 244483, 244482, 244481, 244480, 244456, 244453, 244421, 244418, 244411, 244416, 244377, 244364, 244359, 244355, 244351, 244343, 244340.

  MC production: The Monte Carlo production corresponding to this specific run is named as LHC17e2. The PYTHIA 8 event generator (version 8.210, tune Monash 2013) was used to simulate minimum-bias pp collisions.

- The analysis for pp collisions at $\sqrt{s} = 7$ TeV used the following data.

  Dataset: The data were collected in 2010, for ALICE readers interested in the reconstruction pass, the dataset is identified as LHC10d_pass4.

Year of the data taking: 2010.

Run list: 122374, 122375, 124751, 125023, 125083, 125085, 125097, 125100, 125101, 125133, 125134, 125139, 125140, 125156, 125186, 125295, 125296, 125628, 125630, 125632, 125633, 125842, 125843, 125844, 125847, 125848, 125849, 125850, 125851, 125855, 126004, 126007, 126008, 126073, 126078, 126081, 126082, 126088, 126090, 126097, 126158, 126160, 126167, 126168, 126283, 126284, 126285, 126350, 126351, 126352, 126359, 126403, 126404, 126405, 126406, 126407, 126408, 126409, 126422, 126424, 126425.

MC production: The Monte Carlo production corresponding to this specific run is named as LHC14j4d. The PYTHIA 6 event generator (version 6.425, tune Perugia 2011 [72]) was used to simulate minimum-bias pp collisions.

- The analysis for pp collisions at $\sqrt{s} = 13\,\text{TeV}$ used the following data.

  Dataset: The data were collected in 2016, for ALICE readers interested in the reconstruction pass, the dataset is identified as LHC16l_pass2.

  Year of the data taking: 2016.

  Run list: 258962, 258964, 259088, 259090, 259091, 259096, 259099, 259117, 259118, 259162, 259164, 259204, 259257, 259261, 259263, 259264, 259269, 259270, 259271, 259272, 259273, 259274, 259302, 259303, 259305, 259307, 259334, 259336, 259339, 259340, 259341, 259342, 259378, 259382, 259388, 259389, 259394, 259395, 259396, 259473, 259477, 259747, 259748, 259750, 259751, 259752, 259756, 259781, 259788, 259789, 259822, 259841, 259842, 259860, 259866, 259867, 259868, 259888.

  MC production: The Monte Carlo production corresponding to this specific run is named as LHC18d8_extra. The PYTHIA 8 event generator (version 8.210, tune Monash 2013) was used to simulate minimum-bias pp collisions. The following additional runs (with respect to data) were used in this analysis: 258919, 258920, 258921, 258923, 258926, 258931, 259086, 259381, 259649, 259650, 259668, 259697, 259700, 259703, 259704, 259705, 259711, 259713, 260010, 260011, 260014.

  MC production: for systematic uncertainties due to model dependence, the MC production LHC17d20b2 was also used. Such a production corresponds to pp collisions at the corresponding centre-of-mass energy simulated with the event generator EPOS LHC. The following additional runs (with respect to data) were used in this analysis: 259713, 259711, 259705, 259704, 259703, 259700, 259697, 259668, 259650, 259649,

258923, 258919.

Only runs in which the TPC, ITS, and V0 detectors were included in the data taking were considered. The quality assurance of the used runs was marked as good according with the detector experts. An offline selection, which is called event selection, was further implemented to reduce the beam-induced background as well as the probability to have multiple pp collisions reconstructed as a single one (pileup). The details about the event and track selection are given below. The text is based on the analysis details reported in the two papers in which I participated [35, 73].

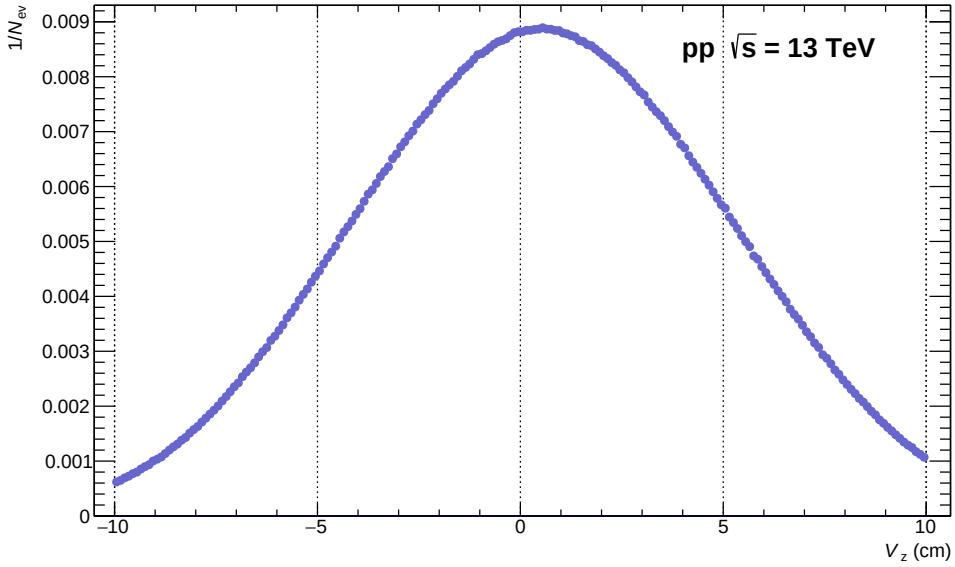

图 3.1: The reconstructed primary vertex along the beam axis in pp collisions at $\sqrt{s} = 13\,\text{TeV}$.

3.2 Event selection

The following event-selection criteria were implemented to select pp collisions with reduced beam-induced background, as well as with negligible pileup.

- The data were collected using a minimum-bias trigger, which required a signal in both V0A and V0C detectors.
- The offline event selection is improved to reject beam-induced background in all collision systems by utilising the timing signals in the two V0 detectors.
- A criterion based on the offline reconstruction of multiple primary vertices in the Silicon

Pixel Detector is applied to reduce the pileup caused by multiple interactions in the same bunch crossing [11, 32, 74].

- The collisions were selected requiring the reconstructed primary vertex along the beam axis within 10 cm ($|V_z| < 10$ cm, see Fig. 3.1).

- To ensure that a hard scattering took place in a collision, events are required to have a trigger particle with transverse momentum above a given threshold. The trigger particle is chosen in the same p_T interval (5–40 GeV/c) as used in previous publications for pp collisions at $\sqrt{s} = 13$ TeV [32, 75].

3.3 Track selection

The measurements of charged-particle multiplicity distributions focus on primary charged particles [76], i.e., particles with a average proper lifetime more than 300 ps, which are either produced directly in the interaction or from decays of particles with mean proper lifetime smaller than 30 ps. Primary charged particles are measured in the pseudorapidity interval of $|\eta| < 0.8$ and with $p_T > 0.5$ GeV. They are reconstructed by utilising the ITS and TPC detectors, which provide measurements of the transverse momentum of the track and its azimuthal angle. As this work is based on charged-particle production associated to the underlying event, two sets of track selection criteria were used: track selection for the highest transverse momentum (p_T^{trig}) charged particle (trigger particle) — defining the UE topological regions — and track selection for multiplicity distributions (associated particles).

Regarding the track selection for the trigger particle, the following selection criteria were considered in order to have high-quality tracks:

- Tracks are required to have at least two hits in the ITS, out of which at least one is in the SPD layers [32].

- The ratio of crossed pad rows to the number of findable clusters in the TPC should be more than 0.8.

- The fraction of TPC clusters shared with another track must be below 0.4.

- Tracks are required to have a number of crossed TPC pad rows larger than $0.85 \times L$, where L (in cm) represents the geometrical track length calculated in the TPC readout plane, excluding the information from pads at sector boundaries (≈ 3 cm from the sector edges).

- The number of TPC clusters associated with the track should exceed $0.7 \times L$.
- The fit quality for ITS and TPC track points must fulfil $\chi^2_{\mathrm{ITS}}/N_{\mathrm{hits}} < 36$ and $\chi^2_{\mathrm{TPC}}/N_{\mathrm{clusters}} < 4$, respectively, where N_{hits} and N_{clusters} represent the number of hits in the ITS and the number of clusters in the TPC associated with the track, respectively.
- To limit the contamination from secondary particles, a selection on the distance of closest approach (DCA) to the reconstructed vertex in the direction parallel to the beam axis (z) of $|\mathrm{DCA}_z| < 2\,\mathrm{cm}$ is applied.
- A p_{T}-dependent selection on the DCA in the transverse plane (DCA_{xy}) of the selected tracks to the primary vertex is applied ($\mathrm{DCA}_{xy} < 0.0182\,\mathrm{cm} + 0.0350\,(\mathrm{cm}\times\mathrm{GeV}/c)/p_{\mathrm{T}}^{1.01}$).
- Tracks associated with the decay products of weakly decaying kaons ("kinks") are rejected.
- To further reduce the contamination from secondary particles, the analysis only considers tracks with $\chi^2_{\mathrm{TPC-ITS}} < 36$, where $\chi^2_{\mathrm{TPC-ITS}}$ is calculated by comparing the track parameters obtained from the combined-track reconstruction (i.e., combining the track from the ITS and TPC) to those extracted only from the TPC, and is constrained by the interaction point [77].

For associated particles, in order to guarantee a uniform response in the azimuth, tracks are required to satisfy looser selection criteria. This set of selection criteria is called TPC-only track cuts. The DCA cut is loosen ($|\mathrm{DCA}_z| < 3.2\,\mathrm{cm}$ and $|\mathrm{DCA}_{xy}| < 2.4\,\mathrm{cm}$) and no restriction on the number of reconstructed points in ITS was considered. The number of clusters in the TPC should be larger than 50. The fit quality for the TPC track points also satisfies $\chi^2_{\mathrm{TPC}}/N_{\mathrm{clusters}} < 4$.

3.4 Bayesian unfolding of multiplicity distributions

The measurements of multiplicity in the trans-max, trans-min, and full transverse regions are smeared out due to the limited acceptance and finite resolution of the detector. Hence, a one-dimensional unfolding technique based on Bayes' theorem [78], correcting for these detector effects and efficiency losses, is introduced to recover the true multiplicity distribution. Here, the unfolding procedure for the measured multiplicity distributions in the full transverse region $Y(N^{\mathrm{T}}_{\mathrm{raw}})$ is taken as an example. The Bayesian unfolding technique starts with the response matrix (smearing matrix) S_1, reflecting the detector effects on the measurements,

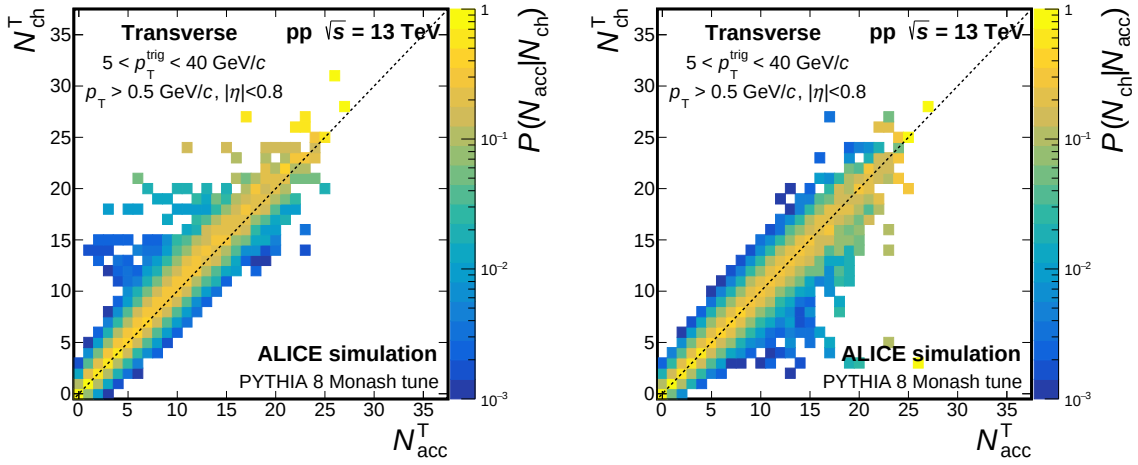

图 3.2: Response matrix S_1 (left) and M_1 matrix (right) of charged-particle multiplicity distributions in the transverse region in pp collisions at $\sqrt{s} = 13\,\text{TeV}$ (see text for details).

which can be obtained from MC simulations including the transport of particles through the detector. The response matrix encodes the conditional probability $S_1 \equiv P(N_{\text{acc}}^{\text{T}}|N_{\text{ch}}^{\text{T}})$ that an event with true multiplicity N_{ch}^{T} is measured as one with multiplicity $N_{\text{acc}}^{\text{T}}$. In the left panel of Fig. 3.2, the values along the diagonal of S_1 represent the probability that a measured event is reconstructed with the correct charged-particle multiplicity. The off-diagonal elements give the probability that fewer (more) particles are reconstructed due to detector inefficiencies (contamination of secondaries and background particles). The one-dimensional unfolded distribution $Y(N_{\text{ch}}^{\text{T}})$ is given as the linear combination between the elements of the matrix M_1 and the measured distribution,

$$Y(N_{\text{ch}}^{\text{T}}) = \sum_{N_{\text{raw}}^{\text{T}}} M_1 Y(N_{\text{raw}}^{\text{T}}), \quad \text{where} \quad M_1 = \frac{S_1 P_0(N_{\text{ch}}^{\text{T}})}{\sum_{N_{\text{ch}}^{\text{T}}} S_1 P_0(N_{\text{ch}}^{\text{T}})}. \tag{3.1}$$

$P_0(N_{\text{ch}}^{\text{T}})$ is a prior probability distribution, and the M_1 matrix represents the conditional probability $M_1 \equiv P(N_{\text{ch}}^{\text{T}}|N_{\text{acc}}^{\text{T}})$ that an event with reconstructed multiplicity $N_{\text{acc}}^{\text{T}}$ has a true multiplicity N_{ch}^{T}. By definition, the elements of the response matrix and the M_1 matrix (shown in the right panel of Fig. 3.2) fulfil the following normalisation conditions: $\sum_{N_{\text{acc}}^{\text{T}}} P(N_{\text{acc}}^{\text{T}}|N_{\text{ch}}^{\text{T}}) = 1$, $\sum_{N_{\text{ch}}^{\text{T}}} P(N_{\text{ch}}^{\text{T}}|N_{\text{acc}}^{\text{T}}) = 1$.

The unfolding technique follows an iterative process. The measured multiplicity distribution is used as the prior distribution in the first iteration. An updated prior distribution,

$$\hat{P}(N_{\rm ch}^{\rm T}) = \frac{Y(N_{\rm ch}^{\rm T})}{\sum_{N_{\rm ch}^{\rm T}} Y(N_{\rm ch}^{\rm T})}, \tag{3.2}$$

is obtained from the second iteration onwards. Hence, the unfolding matrix is optimised as the prior distribution is updated. Finally, a new unfolded distribution can be obtained using Eq. 3.1 with the updated M_1.

After each iteration, the iterative process makes the unfolded distribution closer to the true one. Meanwhile, the statistical uncertainties in the response matrix are also propagated to the unfolded distributions through M_1. Thus, the uncertainties of the response matrix enter a the new unfolded distribution as M_1 is updated. Hence, a larger number of iterations does not guarantee a better unfolded distribution as it might be eventually contaminated by statistical fluctuations [79]. In order to decide when to stop the iterations, the χ^2/ndf between the unfolded distributions in two consecutive iterations is computed. The criterion $\chi^2/\text{ndf} \lesssim 1$ is used to stop the iterative process.

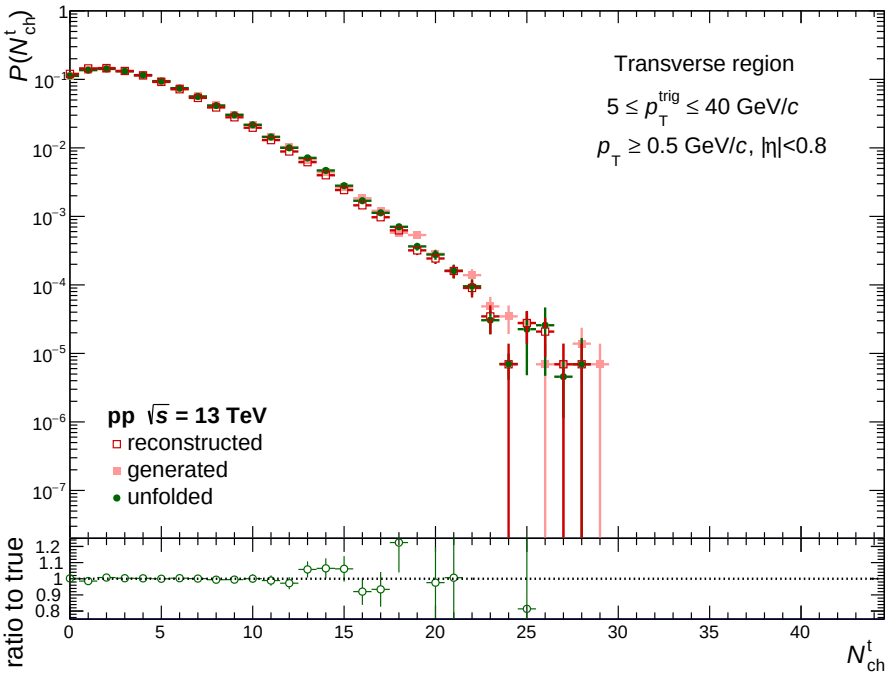

图 3.3: MC closure test of multiplicity distributions based on the official MC production in the full transverse region for pp collisions at $\sqrt{s} = 13\,\text{TeV}$.

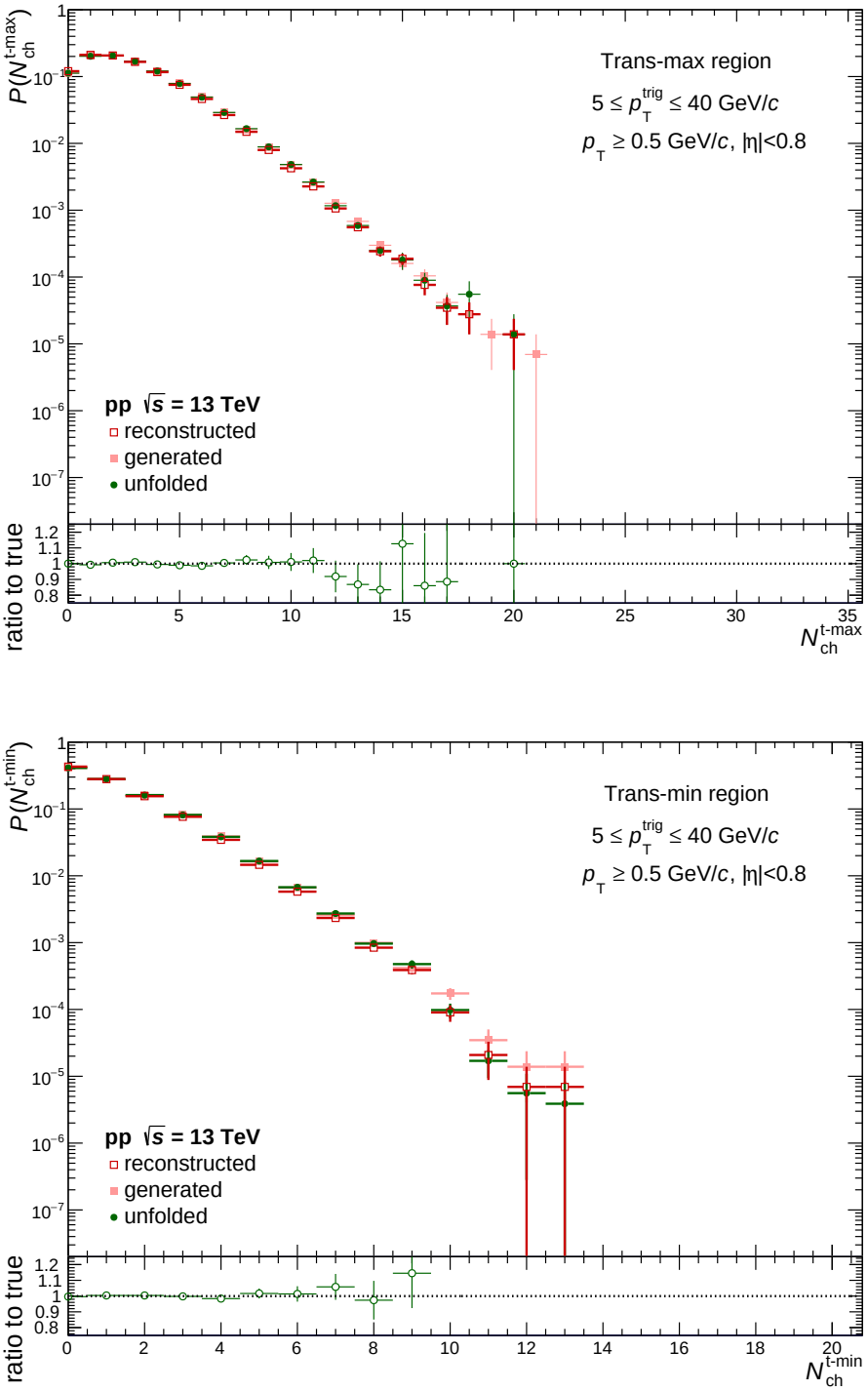

图 3.4: MC closure test of multiplicity distributions based on the official MC production in the trans-max (upper) and trans-min (bottom) regions for pp collisions at $\sqrt{s} = 13\,\text{TeV}$.

3.5 Crosschecks

During the approval of the results, the main crosschecks that were requested are listed below.

I. MC closure test for multiplicity in the full transverse, trans-max, and trans-min regions

The so called "MC closure test" is carried out by correcting the reconstructed spectra from a MC sample after full detector simulation with corrections extracted from the same generator. The correction is expected to reproduce the input MC distribution (without detector effects) within the statistical uncertainty. Any statistically significant difference between input and corrected distributions is referred to as MC non-closure. An example for MC closure test based on PYTHIA 8 (Monash 2013 tune) MC generator in pp collisions at $\sqrt{s} = 13\,\text{TeV}$ for the full transverse, trans-max, and trans-min regions is shown Fig. 3.3 and 3.4 suggesting the unfolding procedure works well within 1%. However, the statistic is limited at very high multiplicities, e.g. multiplicities larger than 10 for the full transverse region. In order to test the unfolding technique at very high multiplicities, a data driven method was used.

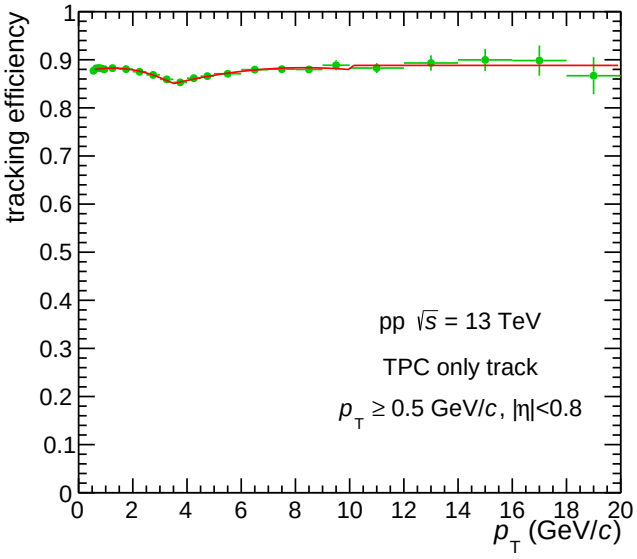

图 3.5: Tracking efficiency for TPC-only track cuts (see the text for more details). Results are presented for pp collisions at $\sqrt{s} = 13\,\text{TeV}$.

II. MC closure test for very high multiplicity using a data-driven approach

Regarding the data-driven approach, a bigger sample (2016 data) was used to verify the performance of the correction procedure at very high multiplicities. The "true" multiplicity

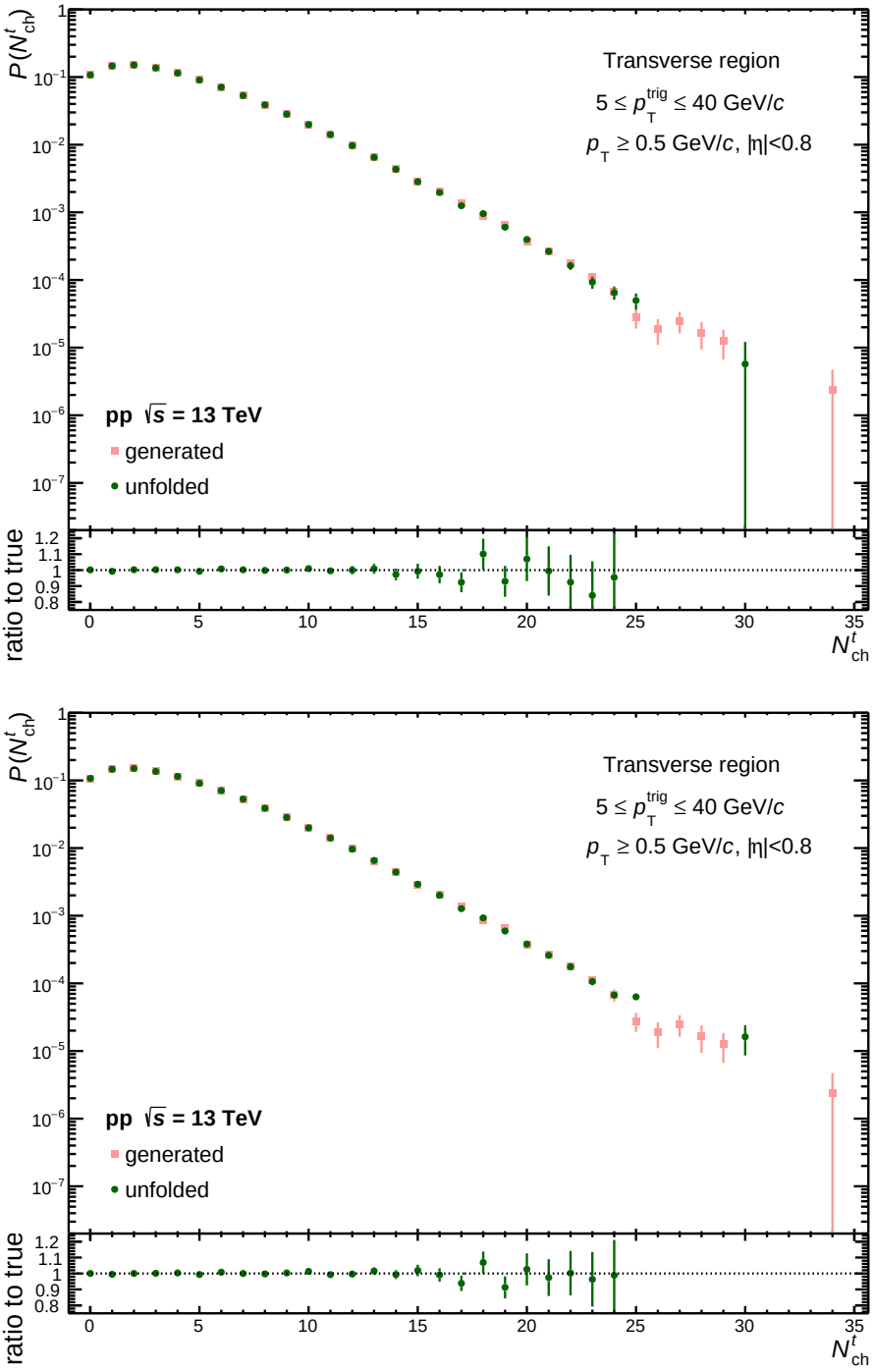

图 3.6: MC closure test of multiplicity distributions based on the data-driven method in the full transverse region for pp collisions at $\sqrt{s} = 13$ TeV. The response matrix is obtained from data (upper) and obtained from PYTHIA 8 (bottom) (see text for details).

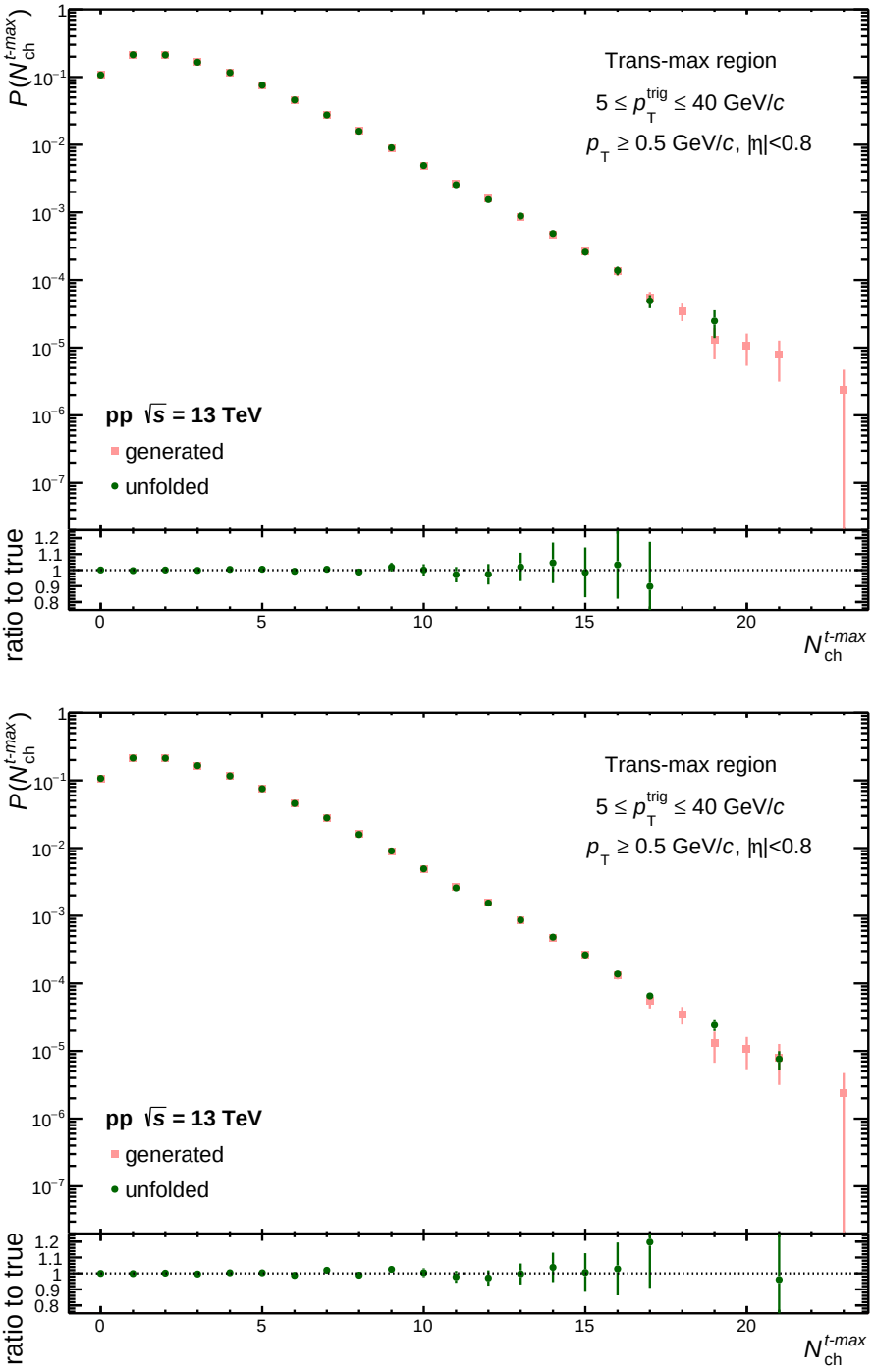

图 3.7: MC closure test of multiplicity distributions based on the data-driven method in the trans-max region for pp collisions at $\sqrt{s} = 13\,\text{TeV}$. The response matrix is obtained from data (upper) and obtained from PYTHIA 8 (bottom).

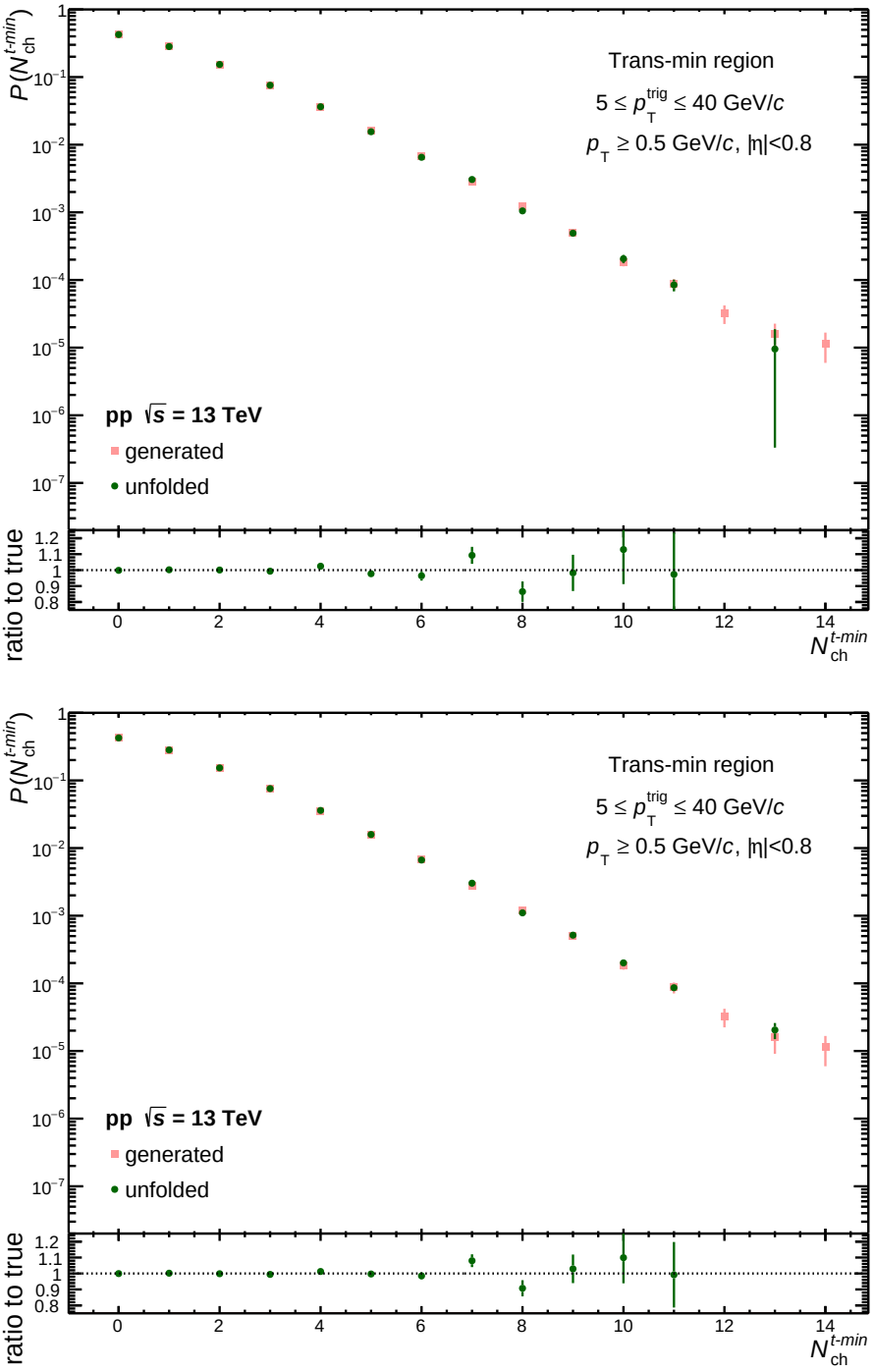

图 3.8: MC closure test of multiplicity distributions based on the data-driven method in the trans-min region for pp collisions at $\sqrt{s} = 13\,\text{TeV}$. The response matrix is obtained from data (upper) and obtained from PYTHIA 8 (bottom).

distributions were obtained considering all accepted tracks (same selection criteria as described before). In order to simulate the detector effects, the p_{T}-dependent tracking efficiency displayed in Fig. 3.5 was applied to the accepted tracks using a random number generator. The outcome corresponds to the "measured" multiplicity distribution. Therefore, for each event we know the "true" and "measured" multiplicity values, and their correlation gives a data-driven multiplicity response matrix. The same unfolding algorithm as implemented in data is applied to the data-driven "measured" distribution using the data-driven multiplicity response matrix. This allows to cross-check the stability of the unfolding procedure at very large $N_{\mathrm{ch}}^{\mathrm{T}}$, $N_{\mathrm{ch}}^{\mathrm{Tmax}}$, and $N_{\mathrm{ch}}^{\mathrm{Tmin}}$ values. The top panels of Fig. 3.6, 3.7, and 3.8 shows the MC closure test for multiplicity distributions in the transverse, trans-max, trans-min regions, respectively. With this approach, we can check the excellent performance of the method at very high multiplicities. It is worth mentioning that a similar study was performed using the PYTHIA 8 event generator, where pp collisions at generator level were used instead of 2016 pp data. With this approach, billion pp collisions were simulated, and the good performance of the method was also verified in a wide multiplicity interval, seen in Fig. 3.6, 3.7, and 3.8.

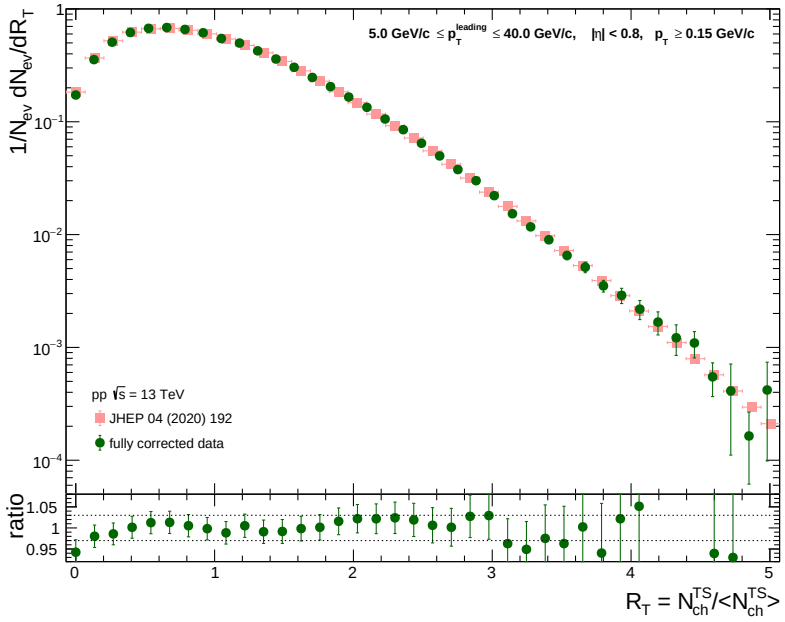

图 3.9: R_{T} distributions in the full transverse region for pp collisions at $\sqrt{s} = 13\,\mathrm{TeV}$. Our data is compared with the published result in Ref. [32].

III. Consistency with existing results

Figure 3.9 shows a comparison between the published R_{T} distribution [32] and the one mea-

sured in this analysis. Within uncertainties, our result is consistent with the published result. One has to keep in mind that the publication used more statistics than in our results. Moreover, the track selection was different, and also the unfolding strategy was different.

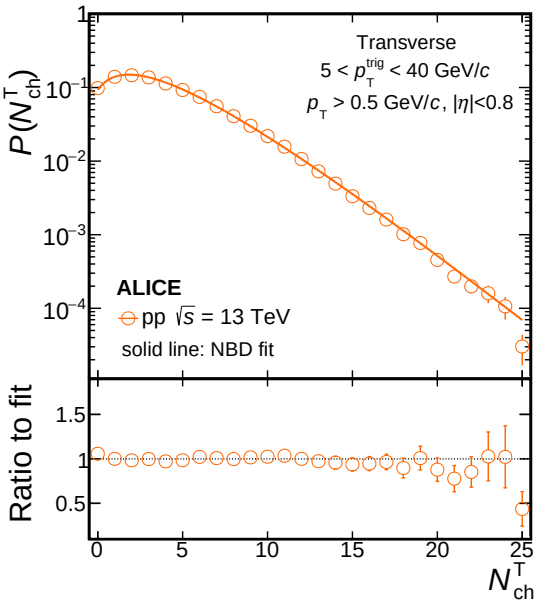

图 3.10: $N_{\mathrm{ch}}^{\mathrm{T}}$ distributions compared to single NBD fit (solid line) in pp collisions at $\sqrt{s} =$ 13 TeV. Ratios of the data to the fit is also presented. Combined systematic and statistical uncertainties are shown as bars.

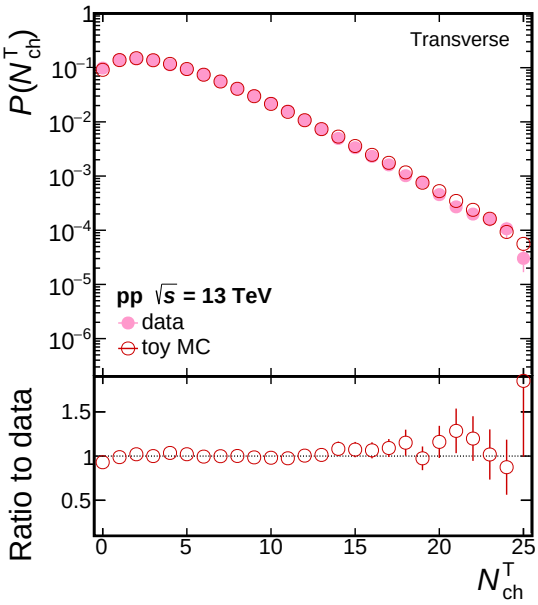

图 3.11: A comparison between data and the MC toy model for the $N_{\mathrm{ch}}^{\mathrm{T}}$ distributions in pp collisions at $\sqrt{s} = 13$ TeV. Ratios of the toy MC to the data are also presented. The statistical uncertainties are shown as bars.

IV. Impact of random correlations in the trans-min and trans-max regions

Random correlations may affect the multiplicity distributions in the trans-min and trans-max regions. In order to investigate the impact of this effect in the multiplicity distributions, a toy Monte Carlo was developed. The aim is discarding random correlations as a possible source of the observed differences between data in the trans-max and trans-min regions.

The toy MC worked as follows. The multiplicity distribution measured in the transverse side was parameterised with a single negative binomial distribution (NBD). As it will be discussed later, the model successfully describes the $N_{\rm ch}^{\rm T}$ distributions. Figure 3.10 shows an example of the NBD fit to data.

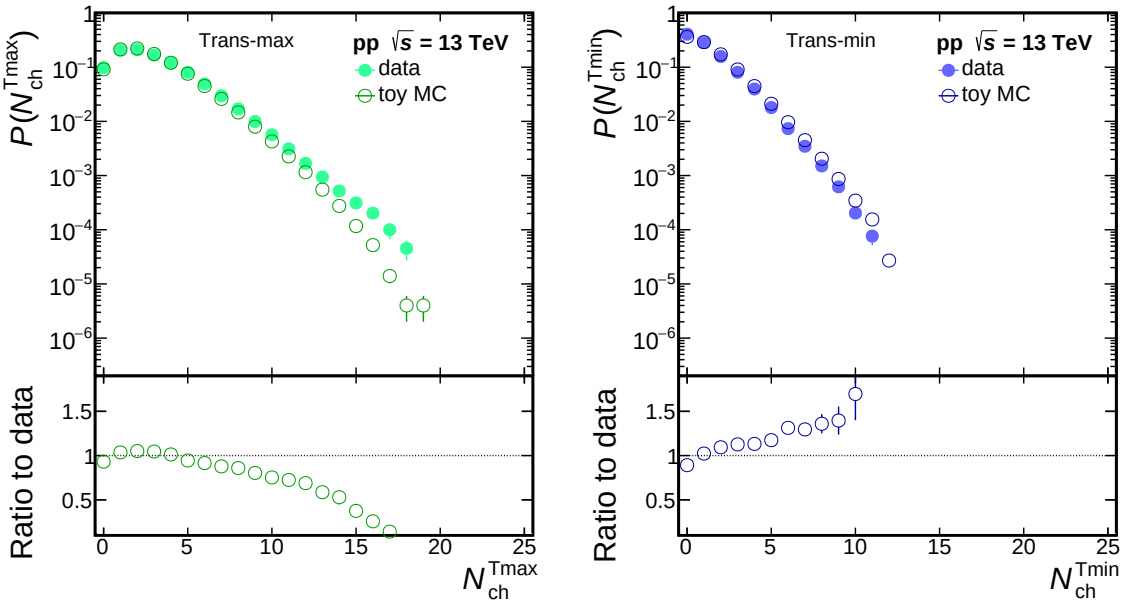

图 3.12: A comparison between data and the MC toy model for the $N_{\rm ch}^{\rm Tmax}$ (left) and $N_{\rm ch}^{\rm Tmin}$ (right) distributions in pp collisions at $\sqrt{s} = 13\,\text{TeV}$. Ratio of the toy MC to the data is also presented. The statistical uncertainties are shown as bars.

Then, the parameterised curve was used to generate integer random numbers. This gives the multiplicity in the transverse region ("number of pseudoparticles"). Then, half of the pseudoparticles was randomly assigned to the transverse I region and the rest to the transverse II region. With this information, even-by-event the multiplicity in the trans-min and trans-max regions were defined. Figures 3.11 and 3.12 show some examples for pp collisions at $\sqrt{s} = 13\,\text{TeV}$. A comparison between data and the MC toy model is shown. As expected, data and the toy MC are fully consistent as it should be. However, it is clear that the random

correlations can not explain the results for the trans-max and trans-min regions, suggesting that physics and not random correlations can explain the data. In data, the trans-max is believed to capture the fragments from jets originated from hard gluon radiation, whereas, the trans-min is more sensitive to multi parton interactions. Similar results are obtained for other energies.

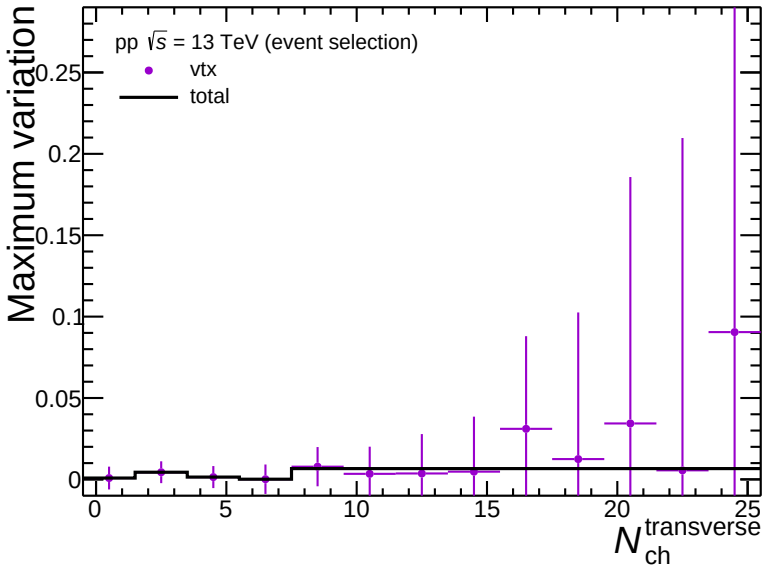

图 3.13: Systematic uncertainty for $N_{\mathrm{ch}}^{\mathrm{T}}$ due to event selection in pp collisions at $\sqrt{s} = 13\,\mathrm{TeV}$.

3.6 Systematic uncertainties

The systematic uncertainties for multiplicity distributions include the variation of event and track selection criteria, MC non-closure uncertainties, and the uncertainties from model dependence for the unfolding technique. Figure 3.13, 3.14, 3.15, and 3.16 shows systematic uncertainty for $N_{\mathrm{ch}}^{\mathrm{T}}$ due to these five sources for pp collisions at $\sqrt{s} = 13\,\mathrm{TeV}$.

– *Event selection*: this source of uncertainty is estimated by selecting collisions within different vertex position along the z axis. The maximum deviation of the results obtained by varying the vertex position (5 and 15 cm) with respect to the result obtained using the default cut (10 cm) is regarded as systematic uncertainty (seen in Fig. 3.13).

– *Track selection for the trigger particle*: this source of uncertainty is estimated by running the full analysis and varying one track selection criterion at a time [80,81]. The variations are similar to the ones described in Ref. [80]. For instance, the minimum value for

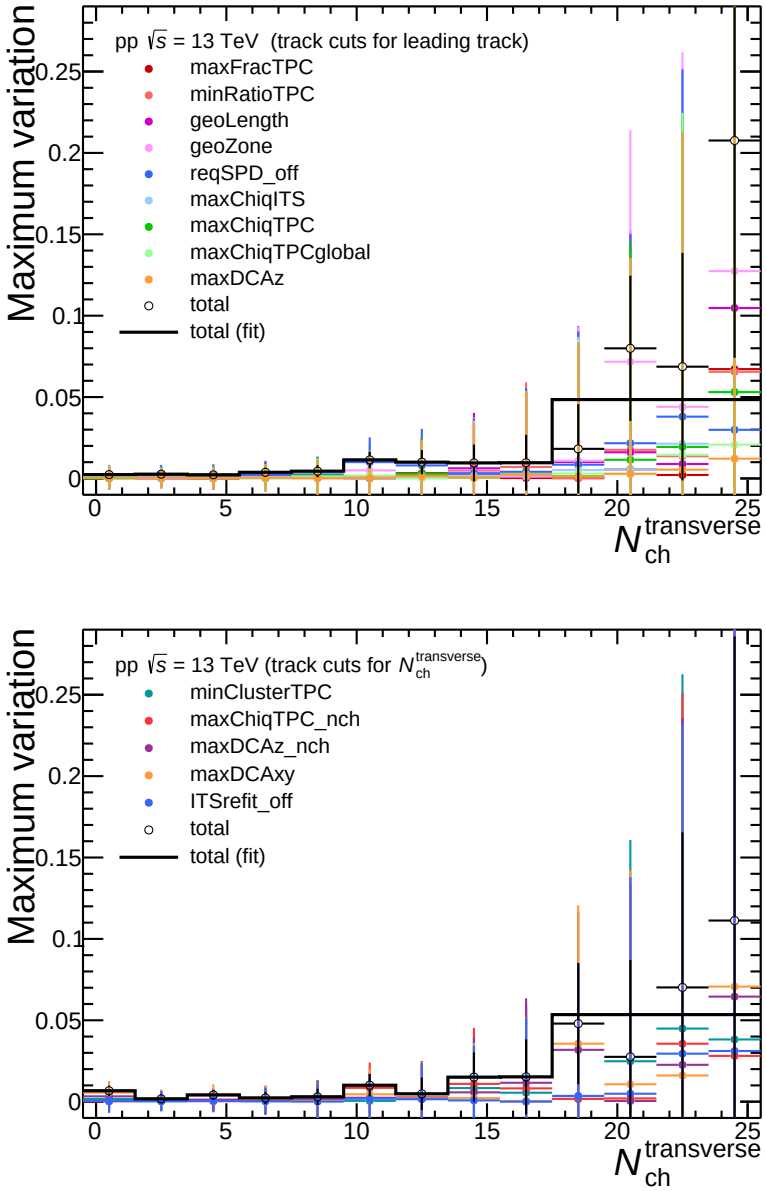

图 3.14: Systematic uncertainty for $N_{\mathrm{ch}}^{\mathrm{T}}$ due to track selection of the trigger particle (upper) and the associated particles (bottom) in pp collisions at $\sqrt{s} = 13\,\mathrm{TeV}$.

crossed pad rows in TPC over the number of findable clusters in TPC is set to 0.7 and 0.9 (the nominal is 0.8), and the maximum fraction of TPC clusters shared with another track is set to 0.2 and 1.0 (the nominal is 0.4). The track fit quality in the ITS and TPC quantified by the $\chi^2_{\mathrm{ITS}}/N_{\mathrm{hits}}$ and the $\chi^2_{\mathrm{TPC}}/N_{\mathrm{clusters}}$ must not exceed 25 and 49 (the nominal is 36), and 3 and 5 (the nominal is 4), respectively. The maximum distance of closest approach to the vertex along the beam axis (DCA_z) is set to 1 and

5 cm (the nominal is 2 cm). The maximum difference between the results obtained with the tighter and looser selections with respect to the nominal values is quantified. The total systematic uncertainty on track reconstruction and selection is given as the sum in quadrature of the differences obtained from the variations of the various selections (seen in Fig. 3.14).

– *Track selection for multiplicity distributions*: this source of uncertainty is also estimated by running the full analysis and varying one track selection criterion at a time. In particular, DCA_z is set to 2.0 and 4.0 cm (the nominal is 3.2 cm), and DCA_{xy} is set to 1.0 and 4.0 cm (the nominal is 2.4 cm). The number of clusters in the TPC is set to 30 and 70 (the nominal is 50). The track fit quality in the TPC quantified by the $\chi^2_{\mathrm{TPC}}/N_{\mathrm{clusters}}$ must not exceed 3 and 5 (the nominal is 4). The maximum difference between the results obtained with the tighter and looser selections with respect to the nominal values is quantified. The total systematic uncertainty on track reconstruction and selection is given as the sum in quadrature of the differences obtained from the variations of the various selections (seen in Fig. 3.14).

– *MC non-closure*: a test is carried out by correcting the reconstructed spectra from a MC sample after full detector simulation with corrections extracted from the same generator. The correction is expected to reproduce the input MC distribution (without detector effects) within the statistical uncertainty. Any statistically significant difference between input and corrected distributions is referred to as MC non-closure. This difference is assigned as systematic uncertainty due to MC non-closure (seen in Fig. 3.15).

– *MC model dependence*: the unfolding technique to correct multiplicity distributions is based on a response matrix obtained from MC simulations. In order to evaluate the model dependence, two sets of simulations are used, and they were carried out with PYTHIA 8 and EPOS LHC event generators, respectively. Then, two sets of corrections obtained from each MC sample are used to correct the data. The ratio of the fully corrected distribution obtained either using PYTHIA 8 or EPOS LHC is regarded as systematic uncertainty. The model dependence is only tested for pp collisions at $\sqrt{s} = 13$ TeV and the same uncertainty is assumed for lower centre-of-mass energies. (seen in Fig. 3.16)

The summary of systematic uncertainties for multiplicity distributions in the transverse, trans-max and trans-min regions for pp collisions at $\sqrt{s} = 2.76$, 5.02, 7, and 13 TeV is shown

in Fig. 3.17 and 3.18. The systematic uncertainties of KNO variables are calculate based on the uncertainties of multiplicity distributions, seen in Tab. 3.1, 3.2, and 3.3. Such as R_{T}, the maximum deviation of $\langle N_{\mathrm{ch}}^{\mathrm{T}}\rangle P(N_{\mathrm{ch}}^{\mathrm{T}})$ is used to estimate the systematic uncertainty for R_{T} due to the above five sources. Table 3.4 and 3.5 summaries the systematic uncertainties for $\langle N_{\mathrm{ch}}^{\mathrm{T}}\rangle$, $\langle N_{\mathrm{ch}}^{\mathrm{Tmax}}\rangle$, and $\langle N_{\mathrm{ch}}^{\mathrm{Tmin}}\rangle$ in pp collisions at $\sqrt{s} = 2.76$, 5.02, 7, and 13 TeV.

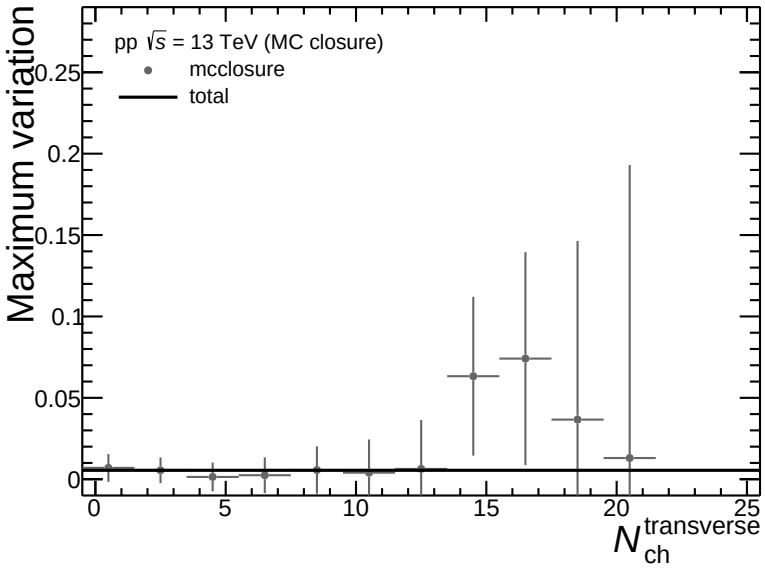

图 3.15: Systematic uncertainty for $N_{\mathrm{ch}}^{\mathrm{T}}$ due to MC non-closure in pp collisions at $\sqrt{s} = 13$ TeV.

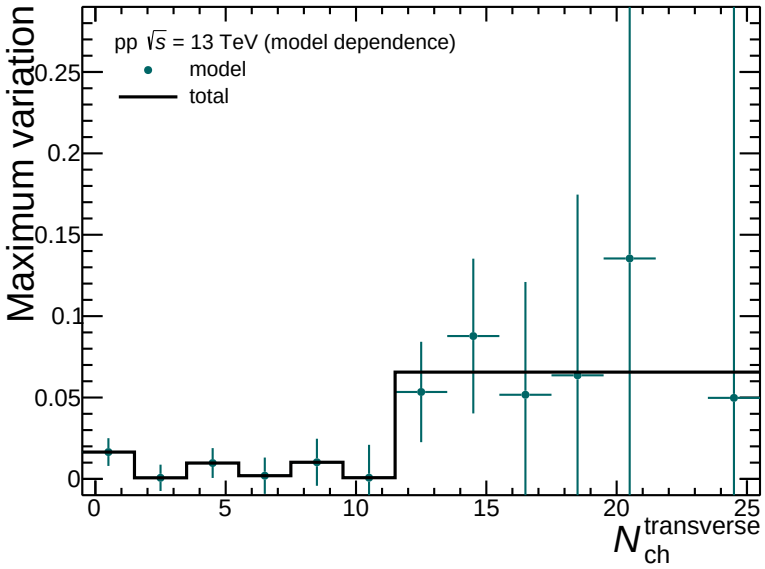

图 3.16: Systematic uncertainty for $N_{\mathrm{ch}}^{\mathrm{T}}$ due to MC model dependence in pp collisions at $\sqrt{s} = 13$ TeV.

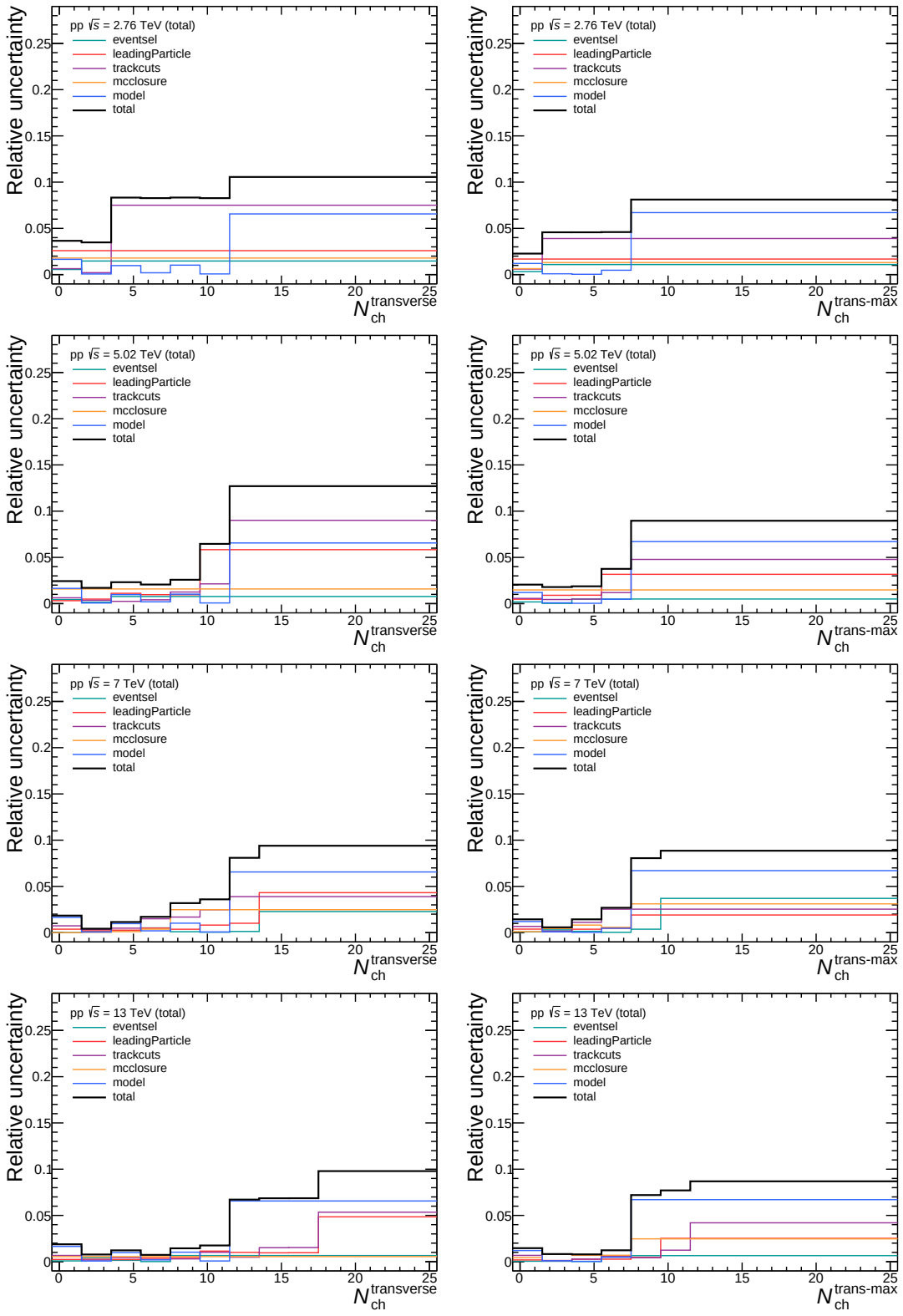

图 3.17: Summary of systematic uncertainties for multiplicity in the transverse (left) and trans-max (right) regions. Results for pp collisions at $\sqrt{s}$ = 2.76, 5.02, 7, and 13 TeV are shown.

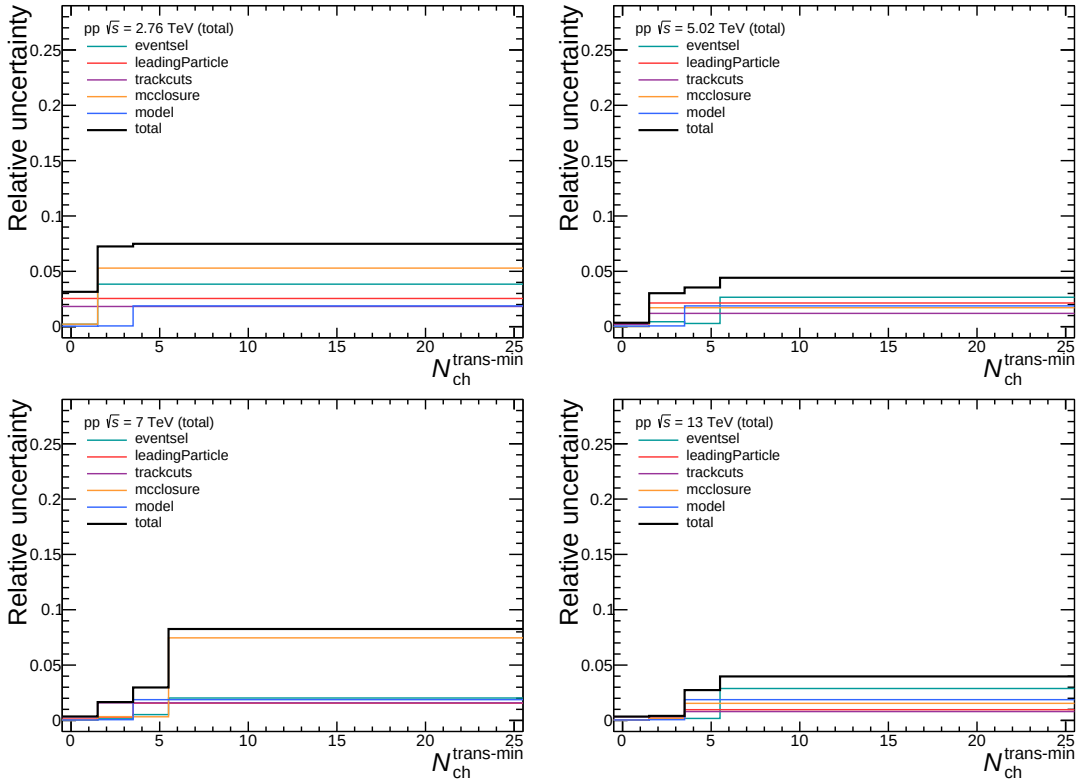

图 3.18: Summary of systematic uncertainties for multiplicity in the trans-min region. Results for pp collisions at $\sqrt{s}$ = 2.76 (upper left), 5.02 (upper right), 7 (bottom left), and 13 TeV (bottom right) are shown.

Source	uncertainty (%)											
	2.76 TeV			5.02 TeV			7 TeV			13 TeV		
R_{T}	0.5	2.5	5.0	0.5	2.5	5.0	0.5	2.5	5.0	0.5	2.5	5.0
event selection	1.5	1.5	1.5	0.3	0.8	0.8	0.1	0.2	2.3	0.4	0.8	0.8
track selection for $p_{\mathrm{T}}^{\mathrm{trig}}$	2.8	2.8	2.8	0.4	1.4	1.4	0.3	0.5	2.4	0.2	1.1	1.2
track selection for $N_{\mathrm{ch}}^{\mathrm{T}}$	2.7	7.0	7.0	0.3	1.0	4.3	0.4	2.7	2.7	0.1	1.1	5.3
MC non-closure	1.2	2.8	2.8	1.6	1.6	1.6	0.1	2.2	2.5	0.6	0.6	0.6
model dependence	0.9	1.2	6.5	0.9	0.6	7.4	0.9	0.3	7.4	0.9	0.8	7.4
Total	4.4	8.3	10.4	1.9	2.6	8.9	1.0	3.5	8.9	1.2	2.0	9.2

表 3.1: Summary of the systematic uncertainties for R_{T} at different R_{T} values for pp collisions at $\sqrt{s}$ = 2.76, 5.02, 7, and 13 TeV.

Source	uncertainty (%)											
	2.76 TeV			5.02 TeV			7 TeV			13 TeV		
$R_{\mathrm{T}}^{\mathrm{max}}$	0.5	2.5	5.0	0.5	2.5	5.0	0.5	2.5	5.0	0.5	2.5	5.0
event selection	1.0	1.0	1.0	negl.	0.4	0.4	0.2	0.1	1.3	0.1	0.7	0.7
track selection for $p_{\mathrm{T}}^{\mathrm{trig}}$	1.0	2.8	2.8	0.6	1.7	1.7	0.1	0.6	2.0	0.2	0.4	2.6
track selection for $N_{\mathrm{ch}}^{\mathrm{Tmax}}$	2.1	7.7	7.7	0.3	1.0	4.8	0.4	2.4	2.4	0.2	0.6	4.2
MC non-closure	0.6	1.4	1.4	1.5	1.5	1.5	0.2	0.9	0.9	0.6	1.3	2.4
model dependence	0.4	1.2	3.4	0.5	2.2	3.4	0.5	2.8	3.4	0.6	3.4	3.4
Total	2.9	8.5	9.1	1.8	3.4	6.3	0.7	3.9	4.9	0.1	3.9	6.5.q

表 3.2: Summary of the systematic uncertainties for $R_{\mathrm{T}}^{\mathrm{max}}$at different $R_{\mathrm{T}}^{\mathrm{max}}$values for pp collisions at $\sqrt{s} = 2.76$, 5.02, 7, and 13 TeV.

Source	uncertainty (%)											
	2.76 TeV			5.02 TeV			7 TeV			13 TeV		
$R_{\mathrm{T}}^{\mathrm{min}}$	0.5	2.5	5.0	0.5	2.5	5.0	0.5	2.5	5.0	0.5	2.5	5.0
event selection	2.7	2.7	2.7	negl.	0.2	0.3	0.1	negl.	0.6	0.2	0.4	2.3
track selection for $p_{\mathrm{T}}^{\mathrm{trig}}$	6.4	6.4	6.4	0.4	2.2	2.8	0.2	0.3	1.7	0.1	0.4	1.1
track selection for $N_{\mathrm{ch}}^{\mathrm{Tmin}}$	8.3	8.3	8.3	0.3	1.2	3.1	0.8	2.7	2.9	0.2	0.6	0.6
MC non-closure	2.0	2.0	2.0	0.9	0.9	0.9	0.1	0.3	0.4	0.1	0.4	1.4
model dependence	0.2	0.2	0.5	0.2	0.2	1.1	0.2	0.2	1.4	0.2	0.5	2.9
Total	11.0	11.0	11.0	1.0	2.7	4.5	0.8	2.7	3.8	0.3	1.1	6.1

表 3.3: Summary of the systematic uncertainties $R_{\mathrm{T}}^{\mathrm{min}}$at different $R_{\mathrm{T}}^{\mathrm{min}}$values for pp collisions at $\sqrt{s} = 2.76$, 5.02, 7, and 13 TeV.

Source (pp, 13 TeV)	uncertainty (%)		
	$\langle N_{\rm ch}^{\rm T}\rangle$	$\langle N_{\rm ch}^{\rm Tmax}\rangle$	$\langle N_{\rm ch}^{\rm Tmin}\rangle$
event selection	0.1	0.1	0.3
track selection for trigger particle	0.1	0.1	0.1
track selection for associated particles	0.2	0.2	0.3
MC non-closure	negl.	0.1	0.1
model dependence	0.8	1.1	0.1
Total	0.8	1.1	0.5

Source (pp, 7 TeV)	uncertainty (%)		
	$\langle N_{\rm ch}^{\rm T}\rangle$	$\langle N_{\rm ch}^{\rm Tmax}\rangle$	$\langle N_{\rm ch}^{\rm Tmin}\rangle$
event selection	negl.	negl.	0.1
track selection for trigger particle	0.2	0.2	0.2
track selection for associated particles	0.9	0.9	1.3
MC non-closure	negl.	negl.	negl.
model dependence	0.8	1.1	0.1
Total	1.2	1.4	1.3

Source (pp, 5.02 TeV)	uncertainty (%)		
	$\langle N_{\rm ch}^{\rm T}\rangle$	$\langle N_{\rm ch}^{\rm Tmax}\rangle$	$\langle N_{\rm ch}^{\rm Tmin}\rangle$
event selection	negl.	negl.	negl.
track selection for trigger particle	0.1	0.3	0.8
track selection for associated particles	0.2	0.2	0.6
MC non-closure	negl.	0.3	0.7
model dependence	0.8	1.1	0.1
Total	0.8	1.2	1.2

表 3.4: Summary of the systematic uncertainties for the average multiplicities in the full transverse, trans-max, and trans-min regions for pp collisions at $\sqrt{s} = 5.02$, 7, and 13 TeV.

Source (pp, 2.76 TeV)	uncertainty (%)		
	$\langle N_{\rm ch}^{\rm T}\rangle$	$\langle N_{\rm ch}^{\rm Tmax}\rangle$	$\langle N_{\rm ch}^{\rm Tmin}\rangle$
event selection	1.2	0.8	2.9
track selection for trigger particle	1.7	0.6	6.5
track selection for associated particles	4.4	4.1	8.8
MC non-closure	0.7	0.2	1.5
model dependence	0.8	1.1	0.1
Total	5.0	4.4	11.4

表 3.5: Summary of the systematic uncertainties for the average multiplicities in the full transverse, trans-max, and trans-min regions for pp collisions at $\sqrt{s} = 2.76\,\text{TeV}$.

3.7 Analysis details underlying event in pp and p-Pb collisions

During the development of the analysis, the author also contributed to the ALICE paper that reported the underlying event properties in pp and p–Pb collisions at $\sqrt{s_{\rm NN}} = 5.02\,\text{TeV}$. The topic was directly connected with the present thesis because the paper reported the average charged particle density as a function of $p_{\rm T}^{\rm trig}$ for the three topological regions, whereas, in this thesis the multiplicity distributions is reported. Below a summary of this paper [73] can be found. Keep in mind that results for $p_{\rm T} > 0.5\,\text{GeV}/c$ are presented, similar conclusions are obtained for the other $p_{\rm T}$ cutoffs.

Measurements of the event activity as a function of $p_{\rm T}^{\rm trig}$ in pp and p–Pb collisions at the same centre-of-mass energy per nucleon pair ($\sqrt{s_{\rm NN}} = 5.02\,\text{TeV}$) were reported. The event activity for each topological region (see the introduction) in p–Pb collisions is compared with that in pp collisions at the same $p_{\rm T}^{\rm trig}$. The results from pp collisions are compared to predictions from the EPOS tune LHC [54] and PYTHIA 8.244 Monte Carlo event generators.

Since the simulations details of EPOS LHC were already presented, here the general aspects of PYTHIA 8 simulations of p–Pb collisions are briefly mentioned. p–Pb collisions were simulated using Angantyr [82], a model that extrapolates the pp physics implemented in Pythia to p–Pb collisions. Inspired by the Fritiof model [83] and the notion of "wounded" or "participating" nucleons, the collisions involving nuclei is generalised in this model, where a hot thermalised medium is not formed. The calculation of the number of wounded nucleons is performed in the Glauber model in impact parameter space. Given these assumptions, the general final-state properties could be well described by the model, e.g., multiplicity and

transverse momentum distributions of charged particles in p–Pb collisions.

The measurement of event activity as a function of $p_{\mathrm{T}}^{\mathrm{trig}}$ in each topological region is quantified with the primary charged-particle number density:

$$\left\langle \frac{\mathrm{d}^2 N_{\mathrm{ch}}}{\mathrm{d}\eta \mathrm{d}\varphi} \right\rangle (p_{\mathrm{T}}^{\mathrm{trig}}) = \frac{1}{\Delta\eta\Delta\varphi} \frac{1}{N_{\mathrm{ev}}(p_{\mathrm{T}}^{\mathrm{trig}})} N_{\mathrm{ch}}(p_{\mathrm{T}}^{\mathrm{trig}}), \tag{3.3}$$

and summed transverse-momentum density:

$$\left\langle \frac{\mathrm{d}^2 \sum p_{\mathrm{T}}}{\mathrm{d}\eta \mathrm{d}\varphi} \right\rangle (p_{\mathrm{T}}^{\mathrm{trig}}) = \frac{1}{\Delta\eta\Delta\varphi} \frac{1}{N_{\mathrm{ev}}(p_{\mathrm{T}}^{\mathrm{trig}})} \sum p_{\mathrm{T}}(p_{\mathrm{T}}^{\mathrm{trig}}), \tag{3.4}$$

with $N_{\mathrm{ev}}(p_{\mathrm{T}}^{\mathrm{trig}})$ being the number of events in a given $p_{\mathrm{T}}^{\mathrm{trig}}$ interval, $N_{\mathrm{ch}}(p_{\mathrm{T}}^{\mathrm{trig}})$ and $\sum p_{\mathrm{T}}(p_{\mathrm{T}}^{\mathrm{trig}})$ being the multiplicity and sum of the p_{T} of all reconstructed tracks in a given $p_{\mathrm{T}}^{\mathrm{trig}}$ interval for each topological regions, respectively. And $\Delta\eta$ ($\Delta\varphi$) is the 1.6 ($2\pi/3$).

The correction of the transverse momentum spectra (p_{T}) as a function of $p_{\mathrm{T}}^{\mathrm{trig}}$ are calculated for all $p_{\mathrm{T}}^{\mathrm{trig}}$ intervals in each topological region. Then the number and the summed transverse-momentum densities are corrected based on the p_{T} spectra. The p_{T} spectra is corrected following the standard procedure of the ALICE collaboration [84, 85]. The correction of the raw yields considers two aspects: efficiency and contamination from secondary particles. For the efficiency, it is corrected using MC simulations involving the propagation properties of particles obtained from GEANT 3 [86]. In this case, the correction factors are calculated using PYTHIA 8 and EPOS LHC MC event generators for pp and p–Pb collisions, respectively. Also, the efficiency obtained from the simulations is re-weighted according with the primary charged-particle composition measured by ALICE [87] since the relative abundance of various charged-particle species differs in the data and the simulations, as described in Ref. [85]. For the contamination from secondary particles, it is estimated by a fit to the measured d_{xy} distributions, which combines the d_{xy} distributions (templates) of primary and secondary particles obtained from the simulations.

As the UE observables rely on the event topology defined by the leading particle in each individual event, the misidentification of the leading particle, resulting from the limited acceptance and efficiency of the detector, is taken into account. Namely, the leading particle is not detected, which results in the sub-leading particle (or sub-sub-leading particle) with lower p_{T} assigned as the trigger particle. In one case, the misidentified leading particle holds a similar direction to the true leading particle, which leads to little impact on the UE

observables [27]. In another case, the misidentified leading particle has a markedly various direction than the true one, thus the event topology will be rotated and the UE observables will be biased. Consequently, a data-driven procedure described in detail in Ref. [27] is used to correct the number and summed transverse-momentum densities for these two effects. A minor correction on the limited vertex reconstruction efficiency is also implemented in the UE observables.

The systematic uncertainties consider six sources. However, the uncertainties due to "event selection" and "track selection" are calculated following the same procedure implemented in estimating these two sources of uncertainties in the analysis of multiplicity distributions. Note that the "track selection" uses the same selection criteria as the "track selection for trigger particle" in the analysis of multiplicity distributions. Below, another four sources are discussed in detail.

- Secondary contamination: fit the d_{xy} distributions, in various fit ranges (i.e., $-1 < d_{\mathrm{xy}} < 1$ cm to $-2 < d_{\mathrm{xy}} < 2$ cm), using templates derived from the simulations. The systematic uncertainty is quantified by the maximum deviation relative to the result obtained with the default fit interval ($-3 < d_{\mathrm{xy}} < 3$ cm).

- Correction method: given flaws in the correction procedure, a possible bias introduced due to this effect can be evaluated by analysing a MC sample of pp collisions generated using a specific event generator. In this case, the reconstructed quantities in a given event generator are corrected using the correction factors extracted from simulations of the same event generator, which followed the same procedure implemented in the data. One expects, within statistical uncertainty, to reproduce the generated yields using this approach, though, this assumption can be held only if each correction estimated using variables sensitive to a certain correction. The total systematic uncertainty is calculated by the sum in quadrature of any statistically remarkable differences between input and corrected distributions. Moreover, this uncertainty is unique for each topological region.

- ITS-TPC track matching efficiency: this uncertainty results from matching the TPC tracks to ITS hits. It can be estimated according with the difference of this matching efficiency in data and simulations.

- Leading-particle misidentification bias: this source of uncertainty is evaluated according with the deviation between two correction results: data-driven correction and simulation correction where the true leading particle is able to identify.

第 4 章 Results and discussion: energy dependence of the underlying event in pp collisions

In this chapter, we report the energy dependence of multiplicity distributions in the transverse ($N_{\rm ch}^{\rm T}$), trans-max ($N_{\rm ch}^{\rm Tmax}$), and trans-min ($N_{\rm ch}^{\rm Tmin}$) regions for pp collisions at $\sqrt{s} = 2.76$, 5.02, 7, and 13 TeV. Data are fully corrected for detector effect following the strategy discussed in the previous section. As mentioned in Sec. 1.5, the results of ALICE measurements of multiplicity distributions of charged primary particles in INEL>0 (events with at least one charged particle in the pseudorapidity interval $|\eta| < 1$) pp collisions concluded that at $\sqrt{s} = 0.9$ TeV multiplicity distributions, of which no shoulder structure at high multiplicities was observed, could be described by a single NBD within uncertainties. However, above 2 TeV, a shoulder structure at high multiplicities was observed in multiplicity distributions, which could no longer be represented by a single NBD. Instead, a double NBD gave a good representation of the data. Hence, we explore whether a single NBD is enough to describe our result of $N_{\rm ch}^{\rm T}$ distributions and, for the first time, extend this discussion to the multiplicity distributions of the trans-max and trans-min regions. Based on the multiplicity distributions in the three regions, we study the energy dependence of KNO variables for the first time. In the context of this work, KNO variables refer to: $R_{\rm T} = N_{\rm ch}^{\rm T}/\langle N_{\rm ch}^{\rm T}\rangle$, $R_{\rm T}^{\rm max} = N_{\rm ch}^{\rm Tmax}/\langle N_{\rm ch}^{\rm Tmax}\rangle$, and $R_{\rm T}^{\rm min} = N_{\rm ch}^{\rm Tmin}/\langle N_{\rm ch}^{\rm Tmin}\rangle$, with $\langle N_{\rm ch}^{\rm T}\rangle$, $\langle N_{\rm ch}^{\rm Tmax}\rangle$, and $\langle N_{\rm ch}^{\rm Tmin}\rangle$ being the average multiplicity in the transverse, trans-max , and trans-min regions, respectively. We also report the centre-of-mass energy dependence of the average multiplicity density in the transverse and, for the first time, extend the observation to the trans-max and trans-min regions at LHC energies. In addition, the comparison of data to MC models (PYTHIA 8/Monash and EPOS LHC) are discussed.

4.1 Energy dependence of multiplicity distributions

Figure 4.1 shows the $N_{\rm ch}^{\rm T}$ distributions for pp collisions at $\sqrt{s} = 2.76$, 5.02, 7, and 13 TeV. For $N_{\rm ch}^{\rm T} < 5$, the multiplicity distributions are energy independent within $\sim 25\%$. A strong energy dependence is observed at higher $N_{\rm ch}^{\rm T}$ values, we also observe that the higher multiplicity reach is achieved at higher energies. It is worth noting that the distributions do not show a bump at high $N_{\rm ch}^{\rm T}$ values as seen in the inclusive multiplicity distributions reported in MB pp collisions at the LHC energies [88]. The inclusive MB multiplicity distributions were successfully described with a sum of two negative binomial distributions (NBD). The NBD is

defined as [47]:

$$P_{\mathrm{NBD}}(n) = \frac{\Gamma(n+k)}{\Gamma(k)\Gamma(n+1)} \left(\frac{\langle n\rangle}{k+\langle n\rangle}\right)^{n} \left(\frac{k}{k+\langle n\rangle}\right)^{k}, \tag{4.1}$$

where n is the multiplicity, $\langle n\rangle$ is the average multiplicity, and k is the relative dispersion.

Inspired by Giovannini and Ugoccioni [52], the two components are needed to describe the soft (e.g. diffractive physics) and hard components of the sample. They can be understood as events with and without parton-parton scatterings, respectively. Moreover, at the LHC energies the multiplicity distributions exhibit a peak at low multiplicity values (< 5), and a bump structure at higher multiplicity values. The bump structure can be understood as a consequence of fluctuations on impact parameter. This was discussed for the first time in this Ref. [19].

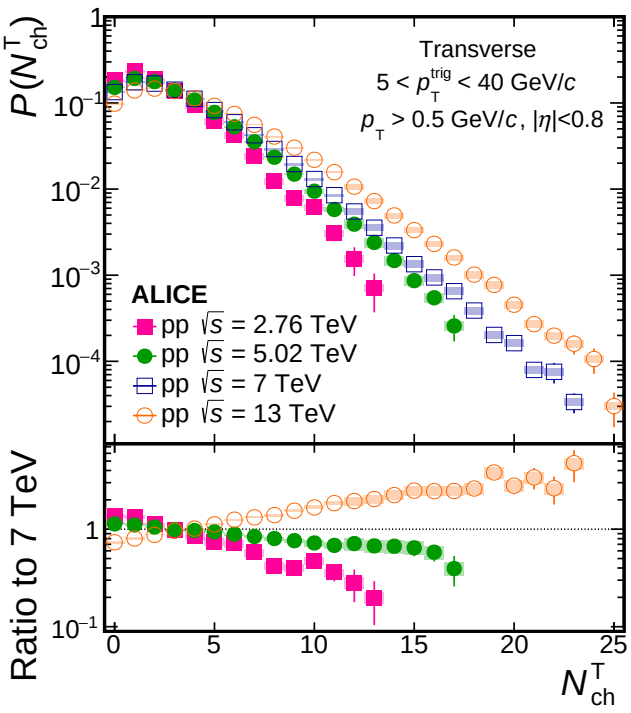

图 4.1: Top: $N_{\mathrm{ch}}^{\mathrm{T}}$ distributions measured in pp collisions for different centre-of-mass energies $\sqrt{s} = 2.76$, 5.02, 7, and 13 TeV. Bottom: $N_{\mathrm{ch}}^{\mathrm{T}}$ distributions normalised to that for pp collisions at $\sqrt{s} = 7$ TeV. The boxes and bars around the data points correspond to the systematic and statistical uncertainties, respectively. The pp sample at $\sqrt{s} = 13$ TeV is smaller than that used for pp collisions at $\sqrt{s} = 7$ TeV.

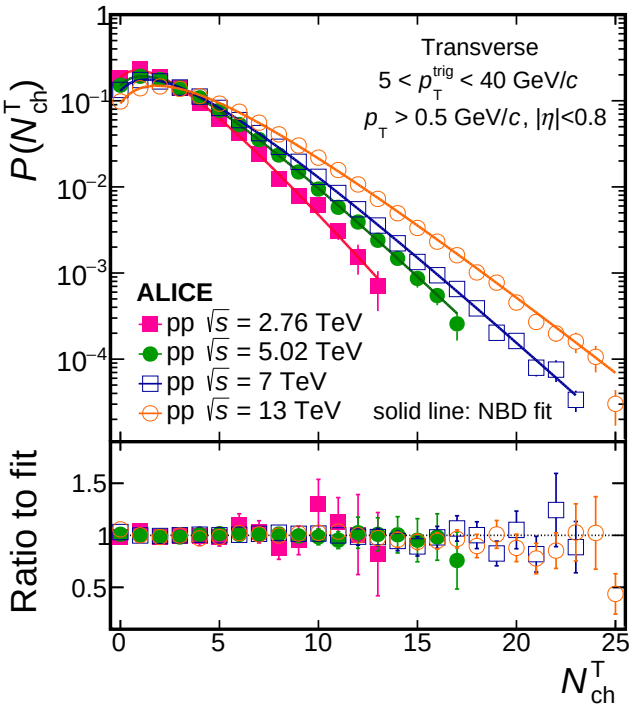

图 4.2: $N_{\mathrm{ch}}^{\mathrm{T}}$ distributions compared to single NBD fits (solid lines) in pp collisions for different centre-of-mass energies $\sqrt{s} = 2.76$, 5.02, 7, and 13 TeV. Ratios of the data to the fits are also presented. Combined systematic and statistical uncertainties are shown as bars.

Therefore, one would expect that by reducing the fluctuations in impact parameter then one can remove the double peak structure. This is something that one can achieve by selecting events with $p_{\mathrm{T}}^{\mathrm{trig}}$ above 5 GeV/c, which guarantees that the average impact parameter of the sample is relatively small (close to zero) reducing the fluctuations on that quantity. Motivated by this observation, the $N_{\mathrm{ch}}^{\mathrm{T}}$ distributions were fitted with NBD. We found that a single NBD was enough to describe the data. A similar observation was done at lower centre-of-mass energies (up to $\sqrt{s} = 540$ GeV by UA5 [47]), whereas, for much higher energies like the LHC ones, two NBD were needed [88]. Figure 4.2 shows the data along with the fitted single NBD. The result is in agreement with the interpretation that the transverse side mostly considers particles produced by the underlying event (mini-jets=MPI), i.e., the hard component was explicitly excluded from the multiplicity estimator. However, the jet fragments from hard ISR-FSR can pollute the transverse side affecting the $N_{\mathrm{ch}}^{\mathrm{T}}$ distribution. In order to separate the ISR-FSR component from the UE to a certain extent, the transverse side was further subdivided in two regions, defined according to their relative multiplicities: trans-max (the

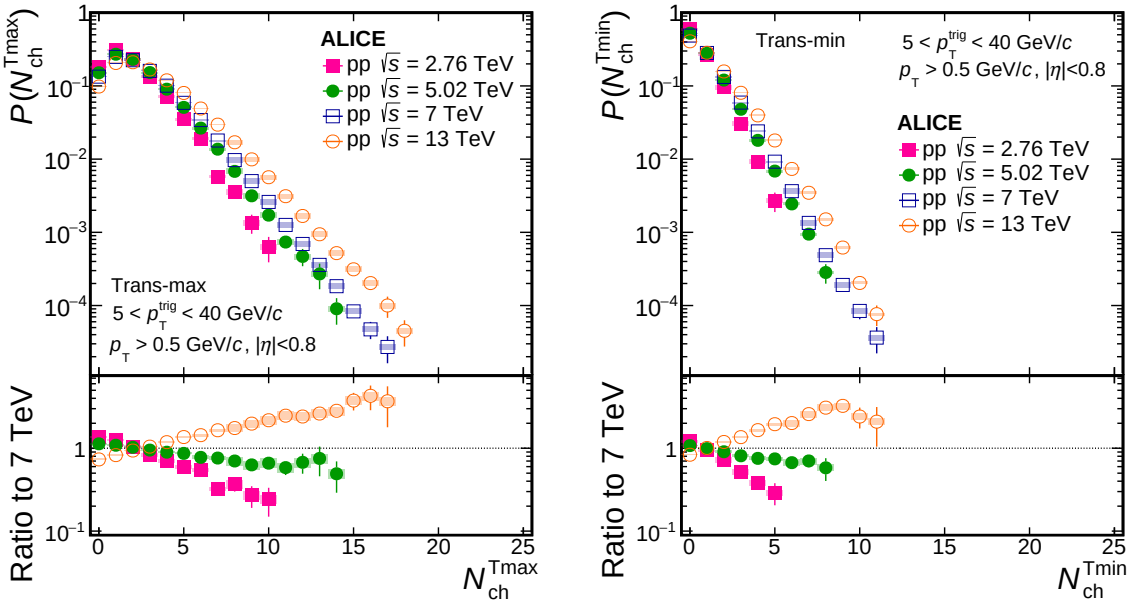

图 4.3: $N_{\mathrm{ch}}^{\mathrm{Tmax}}$ (left) and $N_{\mathrm{ch}}^{\mathrm{Tmin}}$ (right) distributions measured in pp collisions for different centre-of-mass energies $\sqrt{s} = 2.76$, 5.02, 7, and 13 TeV. The bottom panels show multiplicity distributions normalised to that for pp collisions at $\sqrt{s} = 7$ TeV. The boxes and bars around the data points correspond to the systematic and statistical uncertainties, respectively.

sub-transverse region with the larger multiplicity) and trans-min (the sub-transverse region with the smaller multiplicity) regions which have an enhanced sensitivity to ISR-FSR and UE, respectively.

The analysis of UE properties is done for the two sub-transverse regions. The multiplicity distributions in the trans-max and trans-min regions are shown in Fig. 4.3, a smaller energy dependence of $N_{\mathrm{ch}}^{\mathrm{Tmin}}$ distributions than that for the $N_{\mathrm{ch}}^{\mathrm{Tmax}}$ distributions is observed, especially for the first bin. For the sake of further understanding the properties of the two regions, the $N_{\mathrm{ch}}^{\mathrm{Tmax}}$ and $N_{\mathrm{ch}}^{\mathrm{Tmin}}$ were fitted with single NBDs.

The left-hand side of Fig. 4.4 shows that $N_{\mathrm{ch}}^{\mathrm{Tmax}}$ distributions cannot be described with single NBDs, specially at high $N_{\mathrm{ch}}^{\mathrm{Tmax}}$ values. One has to keep in mind that in this case hard physics (ISR-FSR) gets enhanced but the UE contribution is still there. Moreover, Fig. 4.5 displays the centre-of-mass energy dependence of the parameters $\langle n \rangle$ and k obtained from the fits. To estimate the systematic uncertainties of the parameters k and $\langle n \rangle$, we considered two sources as following:

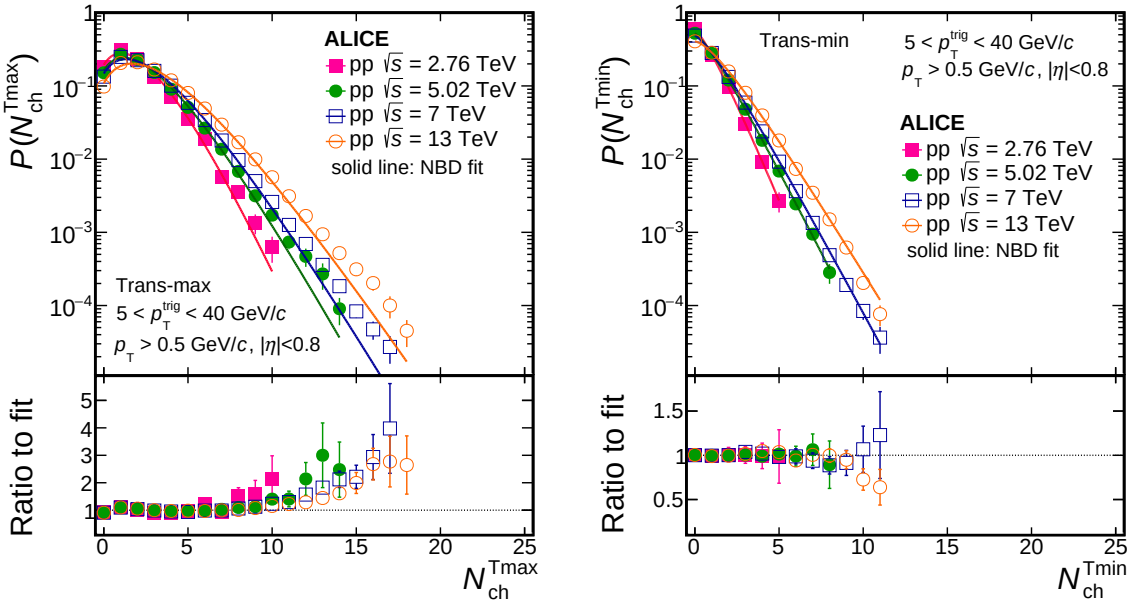

图 4.4: $N_{\mathrm{ch}}^{\mathrm{Tmax}}$ (left) and $N_{\mathrm{ch}}^{\mathrm{Tmin}}$ (right) distributions compared to single NBD fits (solid lines) in pp collisions for different centre-of-mass energies $\sqrt{s} = 2.76$, 5.02, 7, and 13 TeV. Ratios of the data to the fits are also presented. Combined systematic and statistical uncertainties are shown as bars.

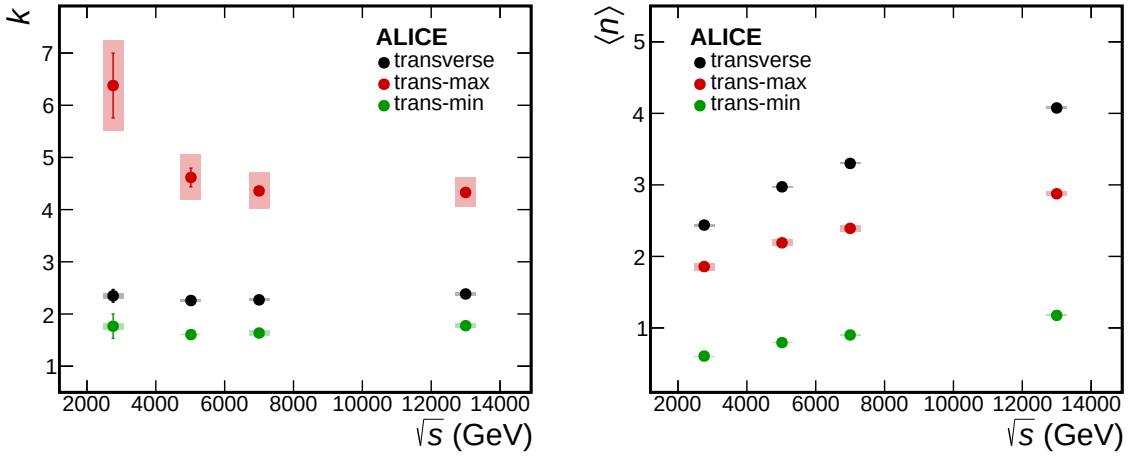

图 4.5: The centre-of-mass energy dependence of the relative dispersion k (left) and the average multiplicity $\langle n \rangle$ (right) in the transverse, trans-max, and trans-min regions for pp collisions at different centre-of-mass energies $\sqrt{s} = 2.76$, 5.02, 7, and 13 TeV. The boxes and bars around the data points correspond to the systematic and statistical uncertainties, respectively.

– *Varying the fitting range*: fit the data excluding the first point (the last three points) with the single NBD. The maximum deviation between the parameters obtained from the single NBDs of these two cases with respect to default one obtained from the original multiplicity distribution is regarded as systematic uncertainty.

– *Varying the distribution's shape based on itself systematic uncertainties*: decrease (increase) the values for the first two points and increase (decrease) the values for the last three points of the data according with the corresponding systematic uncertainties of each data point of the original multiplicity. The maximum deviation between the parameters obtained from the single NBDs of these two cases with respect to default one obtained from the original multiplicity distribution is regarded as systematic uncertainty.

For the trans-max region, the average multiplicity $\langle n \rangle$ increases with $\sqrt{s}$ and the relative dispersion k decreases with $\sqrt{s}$, which could be also attributed to the presence of hard physics that is more important at high energies. A similar behaviour was observed in inclusive multiplicity measurements of high-energy collisions [89].

On the other hand, for the trans-min region, the $N_{\mathrm{ch}}^{\mathrm{Tmin}}$ distributions are well described with single NBDs, suggesting that the MPI-component dominates in the trans-min region. Moreover, in terms of the relative dispersion, Fig. 4.5 shows that it is approximately a constant with increasing $\sqrt{s}$ in the trans-min region (as well as the transverse region), i.e., $N_{\mathrm{ch}}^{\mathrm{Tmin}}$ ($N_{\mathrm{ch}}^{\mathrm{T}}$) follows the KNO scaling [47]. This is verified with the R_{T} distributions discussed in the next section.

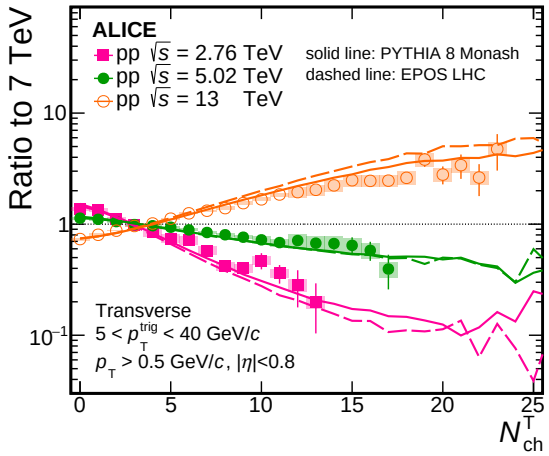

图 4.6: $N_{\mathrm{ch}}^{\mathrm{T}}$ distributions normalised to that for pp collisions at $\sqrt{s} = 7\,\mathrm{TeV}$. Results (markers) are compared to the PYTHIA 8/Monash (solid lines) and EPOS LHC (dashed lines) calculations. The boxes and bars around the data points correspond to the systematic and statistical uncertainties for data, respectively.

Figures 4.6 and 4.7 show the multiplicity distributions for pp collisions at $\sqrt{s}$ = 2.76, 5.02, and 13 TeV normalised to the corresponding multiplicity distribution at 7 TeV. Data are compared to PYTHIA 8/Monash and EPOS LHC predictions. Both models describe $N_{\mathrm{ch}}^{\mathrm{T}}$, $N_{\mathrm{ch}}^{\mathrm{Tmax}}$, and $N_{\mathrm{ch}}^{\mathrm{Tmin}}$ well at low multiplicity. For higher multiplicities, both models describe the data within 1–2 sigmas, and a better agreement is observed at higher energies. It is important to mention that PYTHIA 8/Monash does slightly better than EPOS LHC for all the energies.

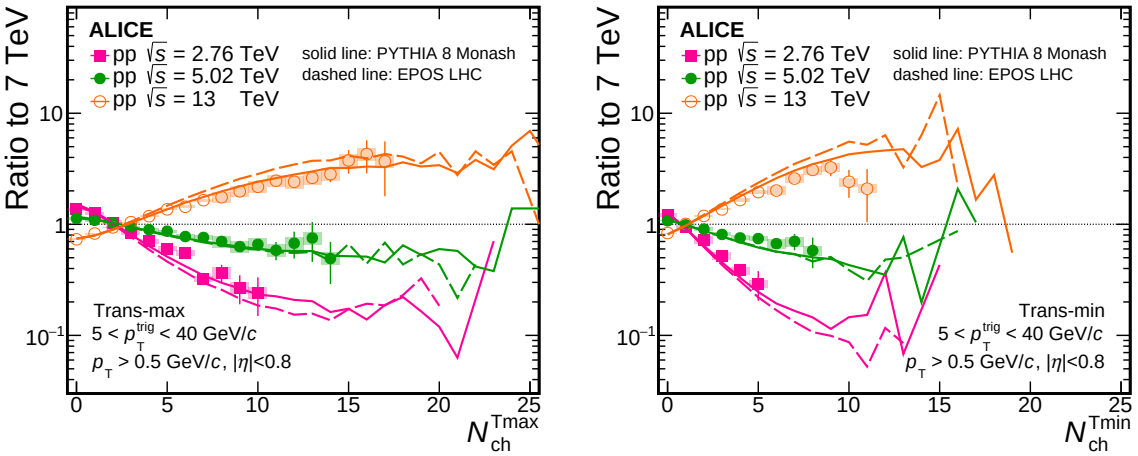

图 4.7: $N_{\mathrm{ch}}^{\mathrm{Tmax}}$ (left) and $N_{\mathrm{ch}}^{\mathrm{Tmin}}$ (right) distributions normalised to that for pp collisions at $\sqrt{s}$ = 7 TeV. Results (markers) are compared to the PYTHIA 8/Monash (solid lines) and EPOS LHC (dashed lines) calculations. The boxes and bars around the data points correspond to the systematic and statistical uncertainties, respectively.

4.2 Energy dependence of KNO variables

Motivated by the behaviour of k as a function of centre-of-mass energy in the transverse and trans-min regions discussed above, where k is approximately a constant with $\sqrt{s}$ indicating a KNO scaling, we also study the multiplicity distributions in KNO variables to further assess the validity of KNO scaling.

Figure 4.8 shows the R_{T} distributions for pp collisions at $\sqrt{s}$ = 2.76, 5.02, 7, and 13 TeV. For low R_{T} values ($0 < R_{\mathrm{T}} < 3$), the R_{T} distributions are found to be approximately (within 20%) energy independent, which indicates a KNO-like scaling [36]. For higher R_{T} values ($R_{\mathrm{T}} > 3$), a large deviation of the ratios from unity is observed. A similar effect is observed in PYTHIA 8 [36, 90]. From an analysis aimed at measuring the MPI, it was observed that for

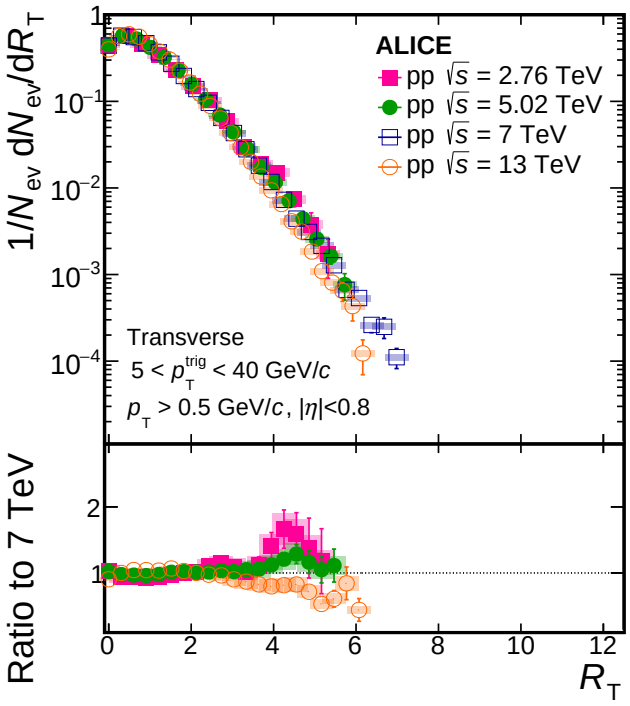

图 4.8: Top: R_{T} distributions in pp collisions for different centre-of-mass energies $\sqrt{s} = 2.76$, 5.02, 7, and 13 TeV. Bottom: R_{T} distributions normalised to that for pp collisions at $\sqrt{s} =$ 7 TeV. The ratio is calculated using a linear interpolation between adjacent points. The boxes and bars around the data points correspond to the systematic and statistical uncertainties, respectively. The pp sample at $\sqrt{s} = 13$ TeV is smaller than that used for pp collisions at $\sqrt{s} = 7$ TeV.

$N_{\mathrm{ch}}/\langle N_{\mathrm{ch}}\rangle$ >3–4, the number of MPI as a function of $N_{\mathrm{ch}}/\langle N_{\mathrm{ch}}\rangle$ deviates from the linear trend suggesting the presence of high-multiplicity jets [29,34]. The presence of high-multiplicity jets may also explain the breaking of KNO-like scaling properties observed at high R_{T} in Fig. 4.8.

Moreover, in terms of the inclusive multiplicity ($N_{\mathrm{ch}}^{\mathrm{incl}}$) for the sum of the toward, away, and transverse regions, we expect that relation to hold: $N_{\mathrm{ch}}^{\mathrm{incl}} = N_{\mathrm{ch}}^{\mathrm{T}} + N_{\mathrm{ch}}^{\mathrm{NS}} + N_{\mathrm{ch}}^{\mathrm{AS}}$, with $N_{\mathrm{ch}}^{\mathrm{NS}}$ ($N_{\mathrm{ch}}^{\mathrm{AS}}$) being the multiplicity from the toward (away) region. For "unbaised" pp collisions, the UE activity is isotropic, hence $N_{\mathrm{ch}}^{\mathrm{incl}} = N_{\mathrm{ch}}^{\mathrm{UE}} + N_{\mathrm{ch}}^{\mathrm{jet,NS}} + N_{\mathrm{ch}}^{\mathrm{jet,AS}}$, where $N_{\mathrm{ch}}^{\mathrm{UE}} \approx 3N_{\mathrm{ch}}^{\mathrm{T}}$, $N_{\mathrm{ch}}^{\mathrm{UE}}$ is the multiplicity from the UE, and $N_{\mathrm{ch}}^{\mathrm{jet,NS}}$ ($N_{\mathrm{ch}}^{\mathrm{jet,AS}}$) is the multiplicity from the fragments of the jet in the toward (away) region. While normalising to $\langle N_{\mathrm{ch}}^{\mathrm{T}}\rangle$, the above relation can be

written as:

$$\frac{N_{\mathrm{ch}}^{\mathrm{incl}}}{\langle N_{\mathrm{ch}}^{\mathrm{T}}\rangle} \approx 3\frac{N_{\mathrm{ch}}^{\mathrm{T}}}{\langle N_{\mathrm{ch}}^{\mathrm{T}}\rangle} + \frac{N_{\mathrm{ch}}^{\mathrm{jet,NS}}}{\langle N_{\mathrm{ch}}^{\mathrm{T}}\rangle} + \frac{N_{\mathrm{ch}}^{\mathrm{jet,AS}}}{\langle N_{\mathrm{ch}}^{\mathrm{T}}\rangle}. \tag{4.2}$$

For "biased" pp collisions, e.g., $R_{\mathrm{T}} = 0$, there is no UE activity in the transverse region, and since UE is believed to be isotropic, there is no UE activity in the toward and away regions. The UE activity starts to increase up to the limit $R_{\mathrm{T}} \sim 3$, corresponding to the case in which the jets yields in the toward and away are negligible in comparison to UE. Namely, $R_{\mathrm{T}} \sim 3$ bias selection on events with "pure UE", i.e. there are only MPIs. And the azimuthal correlation between the trigger particle and the associated particles is almost flat, especially for the toward and away regions where almost no bump is observed.

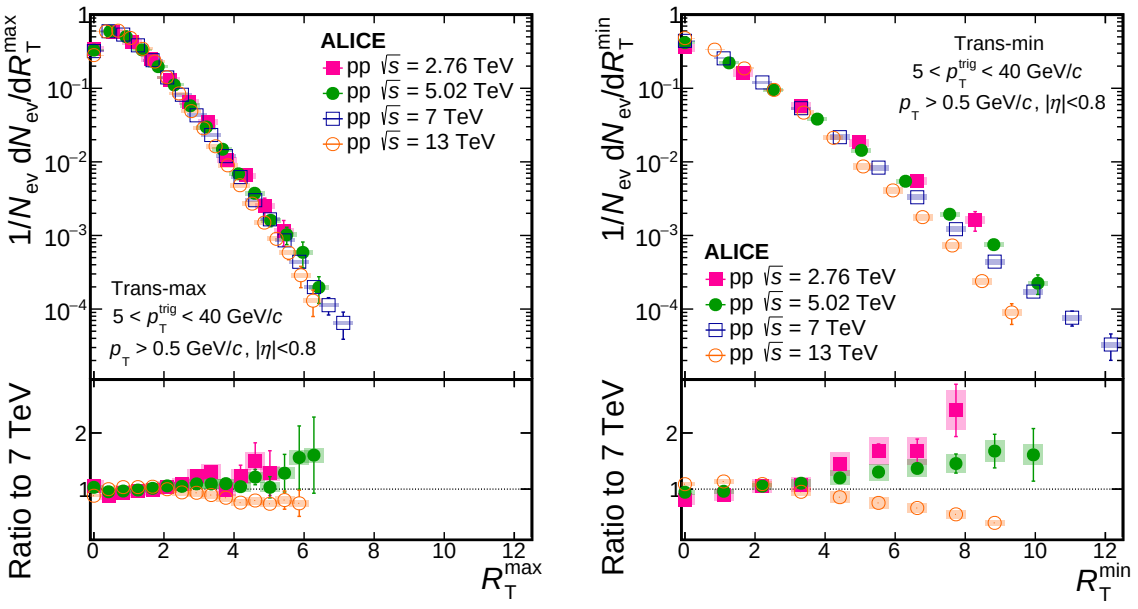

图 4.9: $R_{\mathrm{T}}^{\mathrm{max}}$(left) and $R_{\mathrm{T}}^{\mathrm{min}}$(right) distributions in pp collisions for different centre-of-mass energies $\sqrt{s} = 2.76$, 5.02, 7, and 13 TeV. The bottom panels show KNO variables normalised to that for pp collisions at $\sqrt{s} = 7$ TeV. The ratio is calculated using a linear interpolation between adjacent points. The boxes and bars around the data points correspond to the systematic and statistical uncertainties, respectively. The pp sample at $\sqrt{s} = 13$ TeV is smaller than that used for pp collisions at $\sqrt{s} = 7$ TeV.

For $R_{\mathrm{T}} > 3$, the assumption that the UE activity is well represented by the multiplicity in the transverse region does not hold anymore. Actually, the azimuthal correlation exhibits

some bumps that start appearing in the transverse region. One has to keep in mind that requiring high charged-particle multiplicity in the transverse region biases the sample towards hard pp collisions. The jets originate from hard Bremsstrahlung ISR-FSR radiation), their fragments can contribute to the particle multiplicity in the transverse region breaking the KNO-like scaling at high R_{T}.

The KNO variables are also studied on the trans-max and trans-min regions seen in the Fig. 4.9, suggesting that the $R_{\mathrm{T}}^{\mathrm{max}}$distributions are qualitatively similar to those observed for the transverse region. On the other hand, for the trans-min region, the KNO-like scaling holds in a wider R_{T} interval ($0 < R_{\mathrm{T}} < 4$) with a better agreement, whereas for $R_{\mathrm{T}}^{\mathrm{min}} > 4$ the KNO-like scaling is still broken seen in Fig. 4.9. Moreover, a higher reach is achieved, especially for $R_{\mathrm{T}}^{\mathrm{min}} > 6$, a larger violation is observed which might also be attributed by high-multiplicity jets.

Figures 4.10 and 4.11 show the KNO distributions for pp collisions at $\sqrt{s} = 2.76$, 5.02, and 13 TeV normalised to the corresponding KNO distribution at 7 TeV. Data are compared to PYTHIA 8/Monash and EPOS LHC predictions. The level of agreement between KNO variables and two models is similar to that for multiplicity distributions and models.

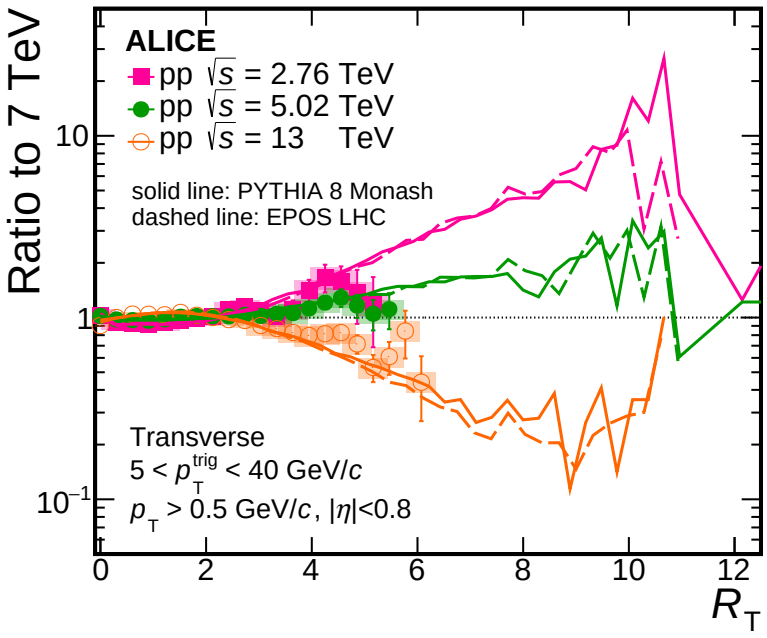

图 4.10: R_{T} distributions normalised to that for pp collisions at $\sqrt{s} = 7$ TeV. Results (markers) are compared to the PYTHIA 8/Monash (solid lines) and EPOS LHC (dashed lines) calculations. The boxes and bars around the data points correspond to the systematic and statistical uncertainties, respectively.

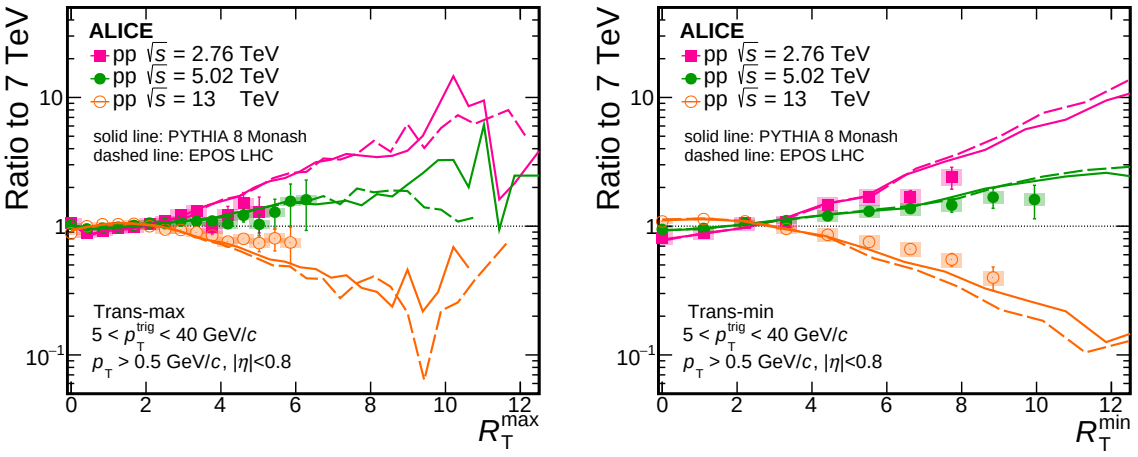

图 4.11: $R_{\mathrm{T}}^{\mathrm{max}}$(left) and $R_{\mathrm{T}}^{\mathrm{min}}$(right) distributions normalised to that for pp collisions at $\sqrt{s} =$ 7 TeV. Results (markers) are compared to the PYTHIA 8/Monash (solid lines) and EPOS LHC (dashed lines) calculations. The boxes and bars around the data points correspond to the systematic and statistical uncertainties, respectively.

4.3 Centre-of-mass energy dependence of average multiplicity densities

We also interest in the centre-of-mass energy $\sqrt{s}$ dependence of average multiplicity densities. Figure 4.12 shows the average multiplicity densities in the transverse region at the plateau for various experiments at RHIC [25], Tevatron [42, 91], LHC [26–28, 30–32, 73] and an additional ALICE data point in pp collisions at $\sqrt{s} = 2.76$ TeV from this analysis. It is obvious that our result, at 2.76 TeV, is consistent with the trend of existing measurements, which can be described by the parameterisation of the form $s^{0.27} + 0.14\log(s)$ [90].

For the trans-max and trans-min regions, our data (in open triangles) in pp collisions at $\sqrt{s} = 2.76$, 5.02, 7, and 13 TeV following the trend reported by the CDF collaboration is seen in Fig. 4.13. Based on the extrapolation of CDF data to LHC energies, the average multiplicity densities seem to increase like a power of the centre-of-mass energy in the trans-min region (more sensitive to MPI). This power-law behaviour is consistent with the centre-of-mass energy dependence of the parameter which regulates MPI in event generators like PYTHIA [18]. However, for the trans-max region (more sensitive to ISR-FSR), the average multiplicity densities seem to increase logarithmically with the centre-of-mass energy.

Figures 4.14 and 4.15 show comparisons between data and models for the centre-of-mass energy dependence of $\langle N_{\mathrm{ch}}^{\mathrm{T}} \rangle$, $\langle N_{\mathrm{ch}}^{\mathrm{Tmax}} \rangle$, and $\langle N_{\mathrm{ch}}^{\mathrm{Tmin}} \rangle$ at the plateau in pp collisions at

$\sqrt{s} = 2.76$, 5.02, 7, and 13 TeV. For the transverse and trans-max regions, PYTHIA 8/Monash describes the average multiplicity densities within one sigma, especially for low energies, while EPOS LHC deviates from data except for the data point at 13 TeV. For the trans-min region, both models describe data quite well among different centre-of-mass energies.

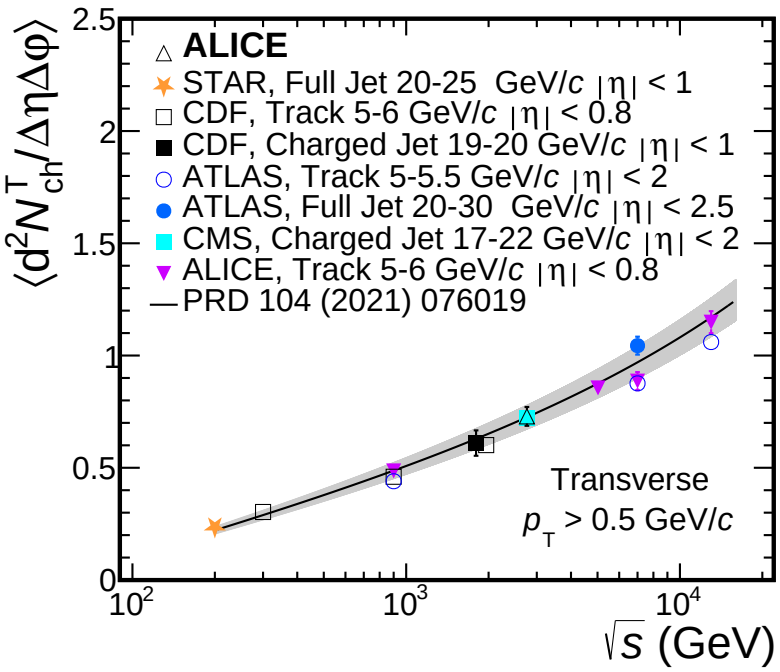

图 4.12: Centre-of-mass energy dependence of the average multiplicity density in the transverse region at the plateau in pp and/or p$\bar{\text{p}}$ collisions. Results from various experiments at RHIC [25], Tevatron [42, 91], LHC [26–28, 30–32, 73] and an additional ALICE data point in pp collisions at $\sqrt{s} = 2.76$ TeV in this analysis are shown. Data are compared with a parameterisation of the form $s^{0.27} + 0.14\log(s)$ [90]. The shaded areas indicate the one sigma systematic uncertainty. Combined systematic and statistical uncertainties are shown as bars.

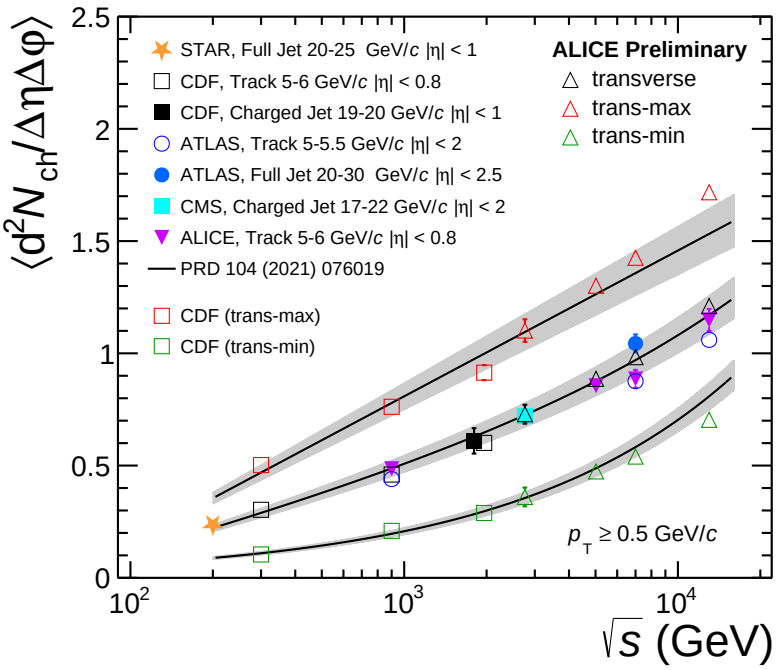

图 4.13: Centre-of-mass energy dependence of the average multiplicity density in the transverse, trans-max and trans-min regions at the plateau in pp and/or p$\bar{\text{p}}$ collisions. The ALICE data points of this work in pp collisions at $\sqrt{s}$ = 2.76, 5.02, 7, and 13 TeV are shown in open triangle markers. Results from various experiments at RHIC [25], Tevatron [42, 91], LHC [26–28, 30–32, 73] are shown in other makers. Data are compared with a parameterisation of the form $s^{0.27} + 0.14\log(s)$ [90]. The shaded areas indicate the one sigma systematic uncertainty. Combined systematic and statistical uncertainties are shown as bars.

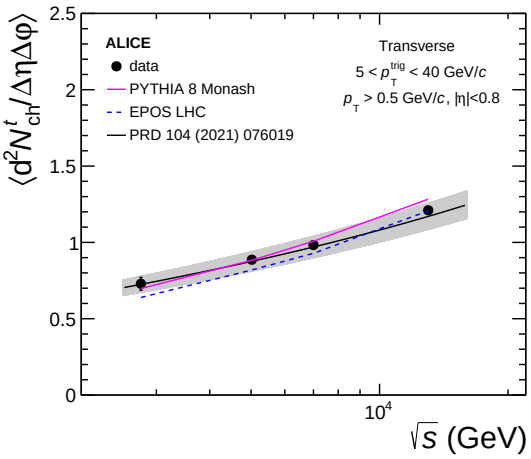

图 4.14: Centre-of-mass energy dependence of the average multiplicity density in the transverse region at the plateau in pp collisions at $\sqrt{s}$ = 2.76, 5.02, 7, and 13 TeV. The results (full circles) are compared to the PYTHIA 8/Monash (solid lines) and EPOS LHC (dashed lines) calculations, as well as a parameterisation [90].The shaded areas indicate the one sigma systematic uncertainty. Combined systematic and statistical uncertainties are shown as bars.

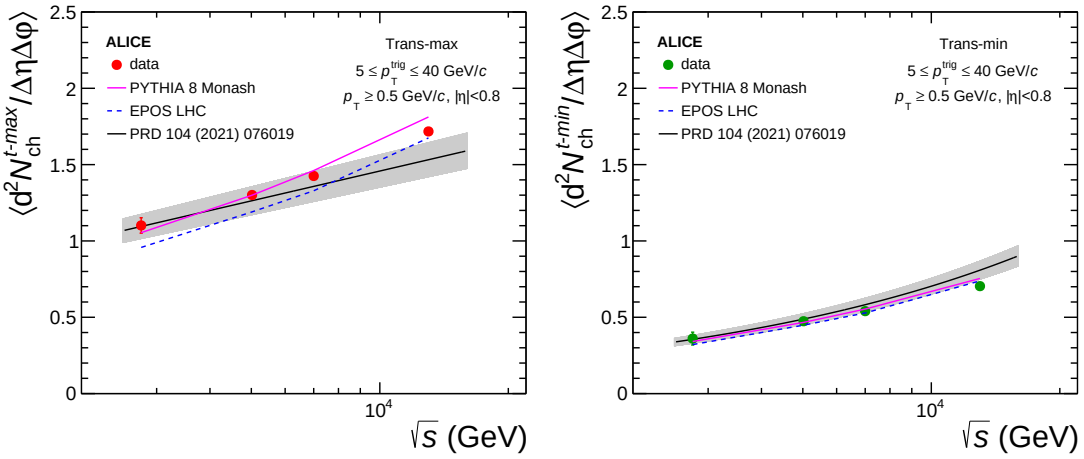

图 4.15: Centre-of-mass energy dependence of the average multiplicity density in the trans-max (left) and trans-min (right) regions at the plateau in pp collisions at $\sqrt{s}$ = 2.76, 5.02, 7, and 13 TeV. The results (full circles) are compared to the PYTHIA 8/Monash (solid lines) and EPOS LHC (dashed lines) calculations, as well as a parameterisation [90]. The shaded areas indicate the one sigma systematic uncertainty. Combined systematic and statistical uncertainties are shown as bars.

第 5 章 Results and discussion: underlying-event properties in pp and p–Pb collisions

In this chapter, we investigate the similarities of UE properties for pp and p–Pb collisions at $\sqrt{s_{\rm NN}} = 5.02\,\text{TeV}$ in the toward, away, and transverse regions. It is worth noting that the UE properties are studied in p–Pb collisions for the first time. Data are fully corrected for detector effect following the strategy discussed in the previous section. The studies are performed in the UE observables (as a function of $p_{\rm T}^{\rm trig}$): the number density

$$\left\langle \frac{{\rm d}^2 N_{\rm ch}}{{\rm d}\eta {\rm d}\varphi} \right\rangle (p_{\rm T}^{\rm trig}) = \frac{1}{\Delta\eta\Delta\varphi} \frac{1}{N_{\rm ev}(p_{\rm T}^{\rm trig})} N_{\rm ch}(p_{\rm T}^{\rm trig}), \tag{5.1}$$

and the summed-$p_{\rm T}$ density

$$\left\langle \frac{{\rm d}^2 \sum p_{\rm T}}{{\rm d}\eta {\rm d}\varphi} \right\rangle (p_{\rm T}^{\rm trig}) = \frac{1}{\Delta\eta\Delta\varphi} \frac{1}{N_{\rm ev}(p_{\rm T}^{\rm trig})} \sum p_{\rm T}(p_{\rm T}^{\rm trig}). \tag{5.2}$$

These results are also compared to MC models: for pp collisions using PYTHIA 8/Monash and EPOS LHC, and for p–Pb collisions using PYTHIA 8/Angantyr and EPOS LHC.

Figure 5.1 shows the comparison between pp and p–Pb collisions at $\sqrt{s_{\rm NN}} = 5.02\,\text{TeV}$ in the number density of charged particles as a function $p_{\rm T}^{\rm trig}$ for the transverse region. The results are discussed considering three various $p_{\rm T}$ thresholds ($0.15\,\text{GeV}/c$, $0.5\,\text{GeV}/c$, $1\,\text{GeV}/c$), exhibiting a similar behaviour for both systems. Namely, the number density sharply rises with increasing the $p_{\rm T}^{\rm trig}$ up to $5\,\text{GeV}/c$ where the distributions tend to flat. This saturation is expected in models including an impact parameter dependence such that the requirement of the presence of a high-$p_{\rm T}$ particle in both systems bias the selection of collisions towards those with a smaller impact parameter [92]. For higher $p_{\rm T}^{\rm trig}$ ($> 5\,\text{GeV}/c$, the so called plateau region), the number density in p–Pb collisions is larger than the one observed in pp collisions by about a factor of 2. A similar observation, the inclusive charged-particle multiplicity densities (${\rm d}N_{\rm ch}/{\rm d}\eta$), measured in the non-single-diffractive event from pp to p–Pb collisions at the same centre-of-mass energy per nucleon pair [93] suggested a larger increase with respect to our result. It is worth noting that, at the plateau region, for pp collisions little $p_{\rm T}^{\rm trig}$ dependence of the number density is observed, which is related with the hard ISR-FSR polluting the transverse region. While varying the $p_{\rm T}$ threshold from $0.15\,\text{GeV}/c$ to $1.0\,\text{GeV}/c$, this dependence is enhanced. In the case of $p_{\rm T} > 0.15\,\text{GeV}/c$, the number density is around

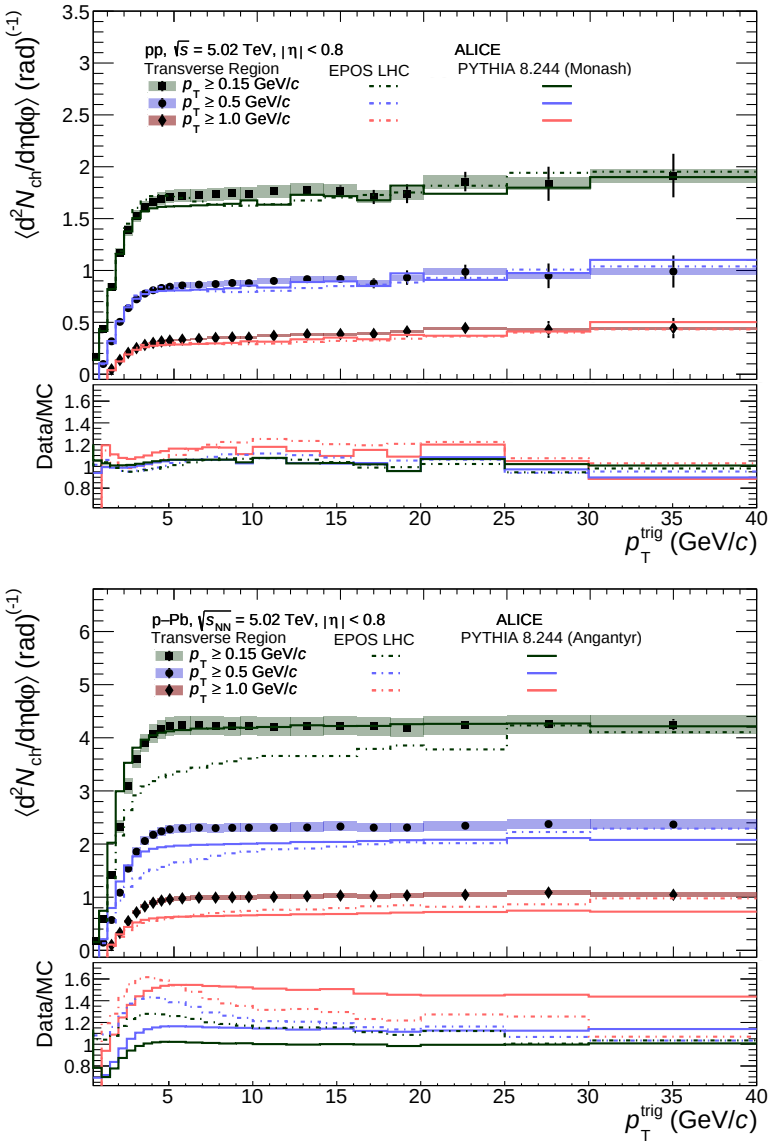

图 5.1: Number density as a function of $p_{\mathrm{T}}^{\mathrm{trig}}$ in the transverse region for pp (top) and p–Pb (bottom) collisions at $\sqrt{s_{\mathrm{NN}}} = 5.02\,\mathrm{TeV}$, considering three various p_{T} cutoffs (0.15 GeV/c, 0.5 GeV/c, and 1 GeV/c). Data (markers) are compared to PYTHIA 8 (solid lines) and EPOS LHC (dashed lines) predictions. The boxes and error bars around the data points correspond to the systematic and statistical uncertainties, respectively.

1.7 (1.9) at $p_{\mathrm{T}}^{\mathrm{trig}} = 5\,\mathrm{GeV}/c$ ($p_{\mathrm{T}}^{\mathrm{trig}} = 40\,\mathrm{GeV}/c$), i.e., the event activity increases by about a factor of 12%. For the highest p_{T} cutoff ($p_{\mathrm{T}} > 1\,\mathrm{GeV}/c$), the increase is around 50% (from 0.3 to 0.45 corresponding to the interval in 5–40 GeV/c). On the contrary, for p–Pb collisions, the distributions are obviously flat at the plateau region for all the three given p_{T} cutoff.

This $p_{\mathrm{T}}^{\mathrm{trig}}$ independence behaviour indicating that the pollution of hard ISR-FSR from the hard proton-proton scattering to the transverse region is smaller in p–Pb collisions than in pp collisions.

The measurements of number density are also compared to the predictions of event generators, seen in Fig. 5.1. In pp collisions, EPOS LHC gives a better description of the number density with respect to p–Pb collisions, though, a bump appears at low $p_{\mathrm{T}}^{\mathrm{trig}}$ ($\approx 3\,\mathrm{GeV}/c$) in this model prediction. That bump structure is not observed in data and not expected in PYTHIA 8/Monash. For p–Pb collisions, EPOS LHC remarkably underestimates the data and fails to capture the number density shape. Instead, PYTHIA 8/Angantyr qualitatively captures the measured densities in p–Pb collisions, for $p_{\mathrm{T}} > 0.15\,\mathrm{GeV}/c$ the model reproduces the data at the plateau region, whereas for higher p_{T} cutoff it underestimates the data at the plateau region. Below, a set of results on the measurements considering $p_{\mathrm{T}} > 0.5\,\mathrm{GeV}/c$ for pp and p–Pb collisions at $\sqrt{s_{\mathrm{NN}}} = 5.02\,\mathrm{TeV}$ are discussed.

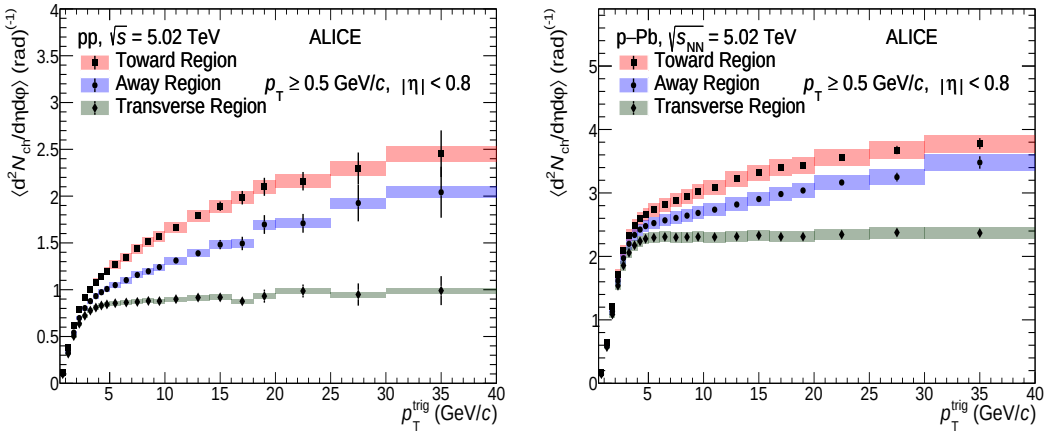

图 5.2: Number density as a function of $p_{\mathrm{T}}^{\mathrm{trig}}$ in the toward, away, as well as transverse regions for pp (left) and p–Pb collisions (right) at $\sqrt{s_{\mathrm{NN}}} = 5.02\,\mathrm{TeV}$. The boxes and error bars around the data points correspond to the systematic and statistical uncertainties, respectively.

Figure 5.2 shows the number density in the toward and away regions with respect to the transverse region for both pp and p–Pb collisions. As to pp collisions, for $p_{\mathrm{T}}^{\mathrm{trig}} \gtrsim 5\,\mathrm{GeV}/c$, in the transverse region the number density almost saturates with increasing $p_{\mathrm{T}}^{\mathrm{trig}}$, as already mentioned above, whereas for both toward and away regions the distributions still rise but less steeply. This continuous rise behaviour can be explained by the particle production in these two regions which are dominated by the fragments of jets, although they also includes contributions from UE. Keep in mind that more particles are produced from jets while increas-

ing $p_{\mathrm{T}}^{\mathrm{trig}}$. For p–Pb collisions, in the toward and away regions the number density also keeps rising with increasing $p_{\mathrm{T}}^{\mathrm{trig}}$ at the plateau region, though, the relative increase of the event activity in the $p_{\mathrm{T}}^{\mathrm{trig}}$ interval 5–40 GeV/c is smaller than that in pp collisions. For instance, the number density at $p_{\mathrm{T}}^{\mathrm{trig}} = 40\,\mathrm{GeV}/c$ is around 1.4 (2) times of the one at $p_{\mathrm{T}}^{\mathrm{trig}} = 5\,\mathrm{GeV}/c$ in p–Pb (pp) collisions. On the other hand, in consideration of the UE contribution to the toward and away regions, the contribution of the event activity in the transverse region to the toward (away) region is around 40% and 60% (∼50% and ∼65%) in pp and p–Pb collisions, respectively. This result can be interpreted as more MPI produced in p–Pb collisions relative to pp collisions at the same centre-of-mass energy per nucleon pair.

Figure 5.3 shows the summed-p_{T} density as well as the number density for the toward, away, and transverse regions in pp collisions, which are also compared to MC predictions. Both PYTHIA 8/Monash and EPOS LHC give a qualitative description of the particle densities in the three regions, even though the two models consider different mechanisms to model the UE. As regards the away region, within uncertainties, PYTHIA 8/Monash does better than EPOS LHC in predicting the data for the full $p_{\mathrm{T}}^{\mathrm{trig}}$ range. The discrepancy between EPOS LHC and data for the number density (summed-p_{T} density) is ∼10% (∼20%) for $5 < p_{\mathrm{T}}^{\mathrm{trig}} < 15\,\mathrm{GeV}/c$. For the toward region, at high $p_{\mathrm{T}}^{\mathrm{trig}}$ (>5 GeV/c) PYTHIA 8/Monash is consistent with data, but for lower $p_{\mathrm{T}}^{\mathrm{trig}}$ the data is overestimated by the model by about a factor of 10%. EPOS LHC exhibits an opposite behaviour relative to PYTHIA 8/Monash in describing the data, i.e., at high $p_{\mathrm{T}}^{\mathrm{trig}}$ the particle densities is remarkably underestimated by EPOS LHC, but for lower $p_{\mathrm{T}}^{\mathrm{trig}}$ the model reproduces the data.

Figure 5.4 shows the summed-p_{T} density as well as the number density for the three topological regions in p–Pb collisions, which are also compared to MC predictions. For the transverse region, only the data-to-model comparison in the summed-p_{T} density is discussed since such comparison in the number density has been mentioned above. The summed-p_{T} density is underestimated at high $p_{\mathrm{T}}^{\mathrm{trig}}$ (>5 GeV/c) by more than 20% in both PYTHIA 8/Angantyr and EPOS LHC. The deviation between PYTHIA 8/Angantyr and data is almost a constant since $p_{\mathrm{T}}^{\mathrm{trig}} \approx 3\,\mathrm{GeV}/c$, whereas EPOS LHC deviates from data by about a factor of 50% at $p_{\mathrm{T}}^{\mathrm{trig}} \approx 3\,\mathrm{GeV}/c$. For another two regions, the number and summed-p_{T} densities cannot be described by PYTHIA 8/Angantyr, especially for $1 < p_{\mathrm{T}}^{\mathrm{trig}} < 5\,\mathrm{GeV}/c$, where a steeper rise of the event activity is observed in data than in PYTHIA 8/Angantyr. For $5 < p_{\mathrm{T}}^{\mathrm{trig}} < 10\,\mathrm{GeV}/c$, the ratio of data to PYTHIA 8/Angantyr becomes flat, suggesting that the model deviates from data in the number and summed-p_{T} densities by around 10% and 30%, respectively. As

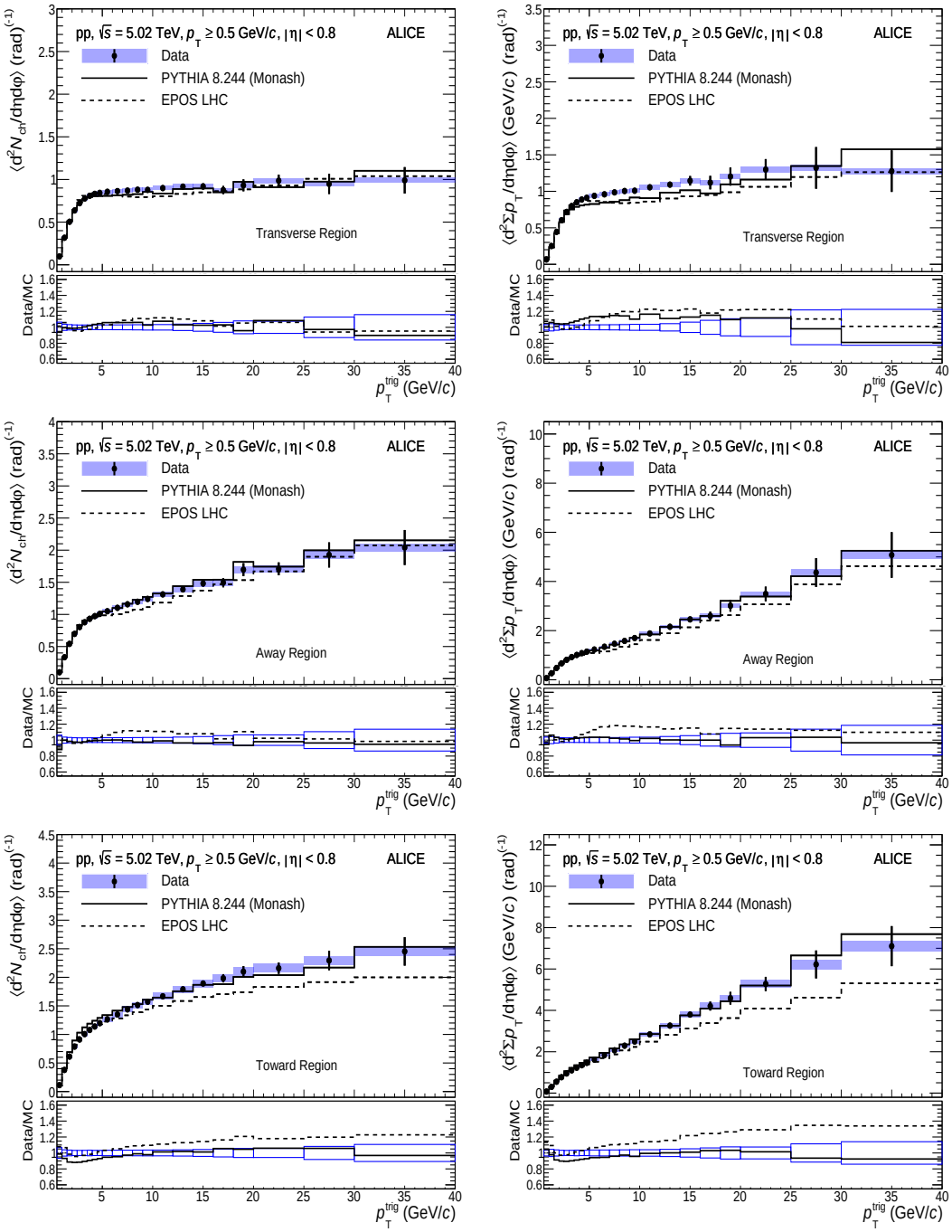

图 5.3: Number (left) and summed-p_{T} (right) densities as a function of $p_{\mathrm{T}}^{\mathrm{trig}}$ in pp collisions at $\sqrt{s} = 5.02\,\mathrm{TeV}$. Data are compared to PYTHIA 8/Monash (solid line) and EPOS LHC (dashed line) predictions for the transverse (top), away (middle), as well as toward (bottom) regions. The boxes and error bars around the data points correspond to the systematic and statistical uncertainties, respectively. Note that in the ratio the boxes around unity correspond to the combined statistical and systematic uncertainties.

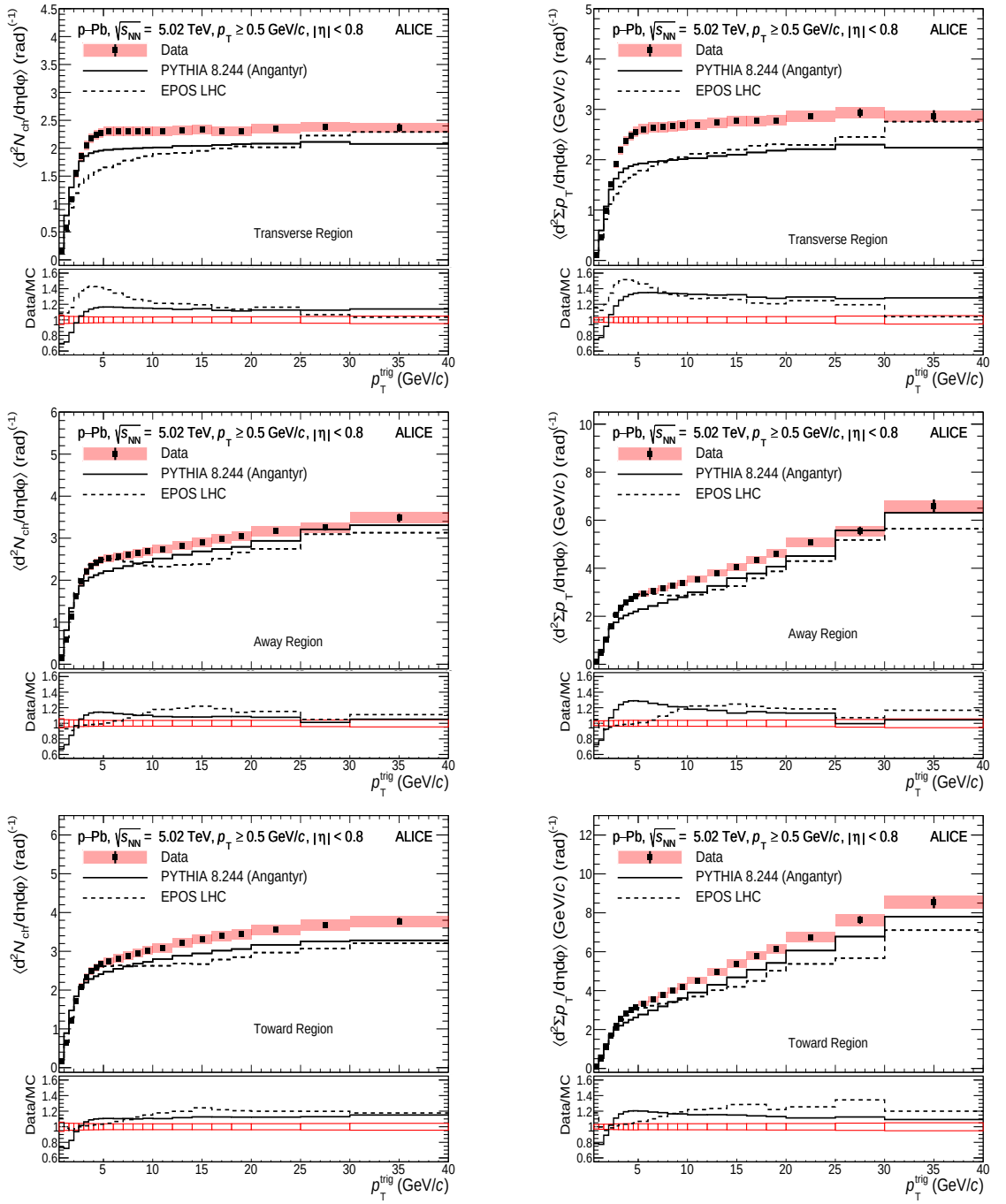

图 5.4: Number (left) and summed-p_{T} (right) densities as a function of $p_{\mathrm{T}}^{\mathrm{trig}}$ in p–Pb collisions at $\sqrt{s_{\mathrm{NN}}} = 5.02\,\mathrm{TeV}$. Data are compared to PYTHIA 8/Monash (solid line) and EPOS LHC (dashed line) predictions for the transverse (top), away (middle), as well as toward (bottom) regions. The boxes and error bars around the data points correspond to the systematic and statistical uncertainties, respectively. Note that in the ratio the boxes around unity correspond to the combined statistical and systematic uncertainties.

regards EPOS LHC, it describes data slightly better relative to PYTHIA 8/Angantyr at low $p_{\mathrm{T}}^{\mathrm{trig}}$ ($<$8 GeV/c), in which interval bump structures occur in the toward and away regions and are not observed in data. For higher $p_{\mathrm{T}}^{\mathrm{trig}}$, the event activity is overestimated by EPOS LHC.

Therefore, these data, used as input in future MC tunes, will contribute to the precise modelling of UE in pp and p–Pb collisions, and they will also help further understand the collectivity effect observed in small system.

第 6 章 Monte-Carlo study of a novel observable aiming at the future analysis

In this section we discuss a recent proposal about an event activity classifier that could be more powerful than R_{T} in order to classify the pp collisions as a function of the underlying event. As discussed in the previous section, with R_{T} we could only explore multiplicities up to $R_{\mathrm{T}} \approx 3$. Higher multiplicities are strongly affected by selection biases. In order to have a better control on the biases towards multi-jet final states, we proposed the measurement of charged particle flattenicity. A MC study can be found below. The section is based on this peer review publication [37].

High-multiplicity pp and p–Pb collisions, at ultra-relativistic energies have unveiled similarities with heavy-ion collisions [4,8,10]. The origin of these effects in small-collision systems is still an open question in the heavy-ion community, where there is no evidence of jet quenching in such collisions [9]. According to event generators like PYTHIA 8, a high-activity at midpseudorapidity (high-multiplicity pp collisions) can be originated by two mechanisms. Either by several semi-hard parton-parton interactions occurring within the same pp collision, a phenomenon that is known as MPI [19], or by multi-jet final states [17]. Since the goal of the study is to establish whether a small drop of strongly-interacting quark-gluon plasma (sQGP) is formed in small collision systems, one has to isolate high-multiplicity pp collisions originated by soft partonic processes.

Multi-partonic interactions offer an alternative approach to explain the observed fluid-like phenomena in high-multiplicity pp collisions. For instance, CR can mimic radial flow patterns in pp collisions with a large number of MPI (N_{mpi}). Models based on the QCD theory of MPI can partially explain collectivity from interference effects in hadronic collisions with N_{mpi} parton-parton scatterings. PYTHIA 8 with the rope hadronization model, which assumes the formation of ropes due to overlapping of strings in a high-multiplicity environment (high N_{mpi}), describes the strangeness enhancement. Regarding the phenomena at large transverse momentum (p_T), the model also produces some features that are present in data from heavy-ion collisions.

One of the most common event classifiers in ALICE is based on the measurement of the charged-particle multiplicity in a different pseudorapidity interval to that where the observable of interest is measured. Different charged-particle multiplicity classes are defined based on the total charge deposited in the V0 detector, hereinafter referred to as V0M multiplicity. The V0

consists of two arrays of scintillating tiles placed on each side of the interaction point covering the full azimuthal acceptance and the pseudorapidity intervals of $2.8 < \eta < 5.1$ (V0A) and $-3.7 < \eta < -1.7$ (V0C). With this approach, the strangeness enhancement was discovered in pp collisions.

Alternative studies that use event shape observables like transverse sphericity, transverse spherocity [94], and the relative transverse activity classifier [36] have tried to isolate the soft particle production. However, these event shape observables are still sensitive to biases originating due to hard gluon radiation which makes it difficult to interpret the results [44]. Another event shape called event isotropy has been introduced recently in ref. [95], designed to robustly identify isotropic radiation patterns in collider event which needs to be explored in the future. Moreover, given that they rely on tracking and with the existing experiments it is only possible at mid-pseudorapidity, the event selection based on charged-particle activity in a narrow pseudorapidity interval at mid-rapidity biases the charge-particle yield due to the auto-correlation [11]. This effect has been studied by the ALICE collaboration [11] and this motivated the use of a multiplicity estimator based on the activity in the forward region. With this approach, the reduction of the biases was notable, however other biases towards multi-jet final states were found. For example, the attempt to search for jet quenching effects in pp collisions has not been successful [38, 96]. Although a significant broadening is observed in the acoplanarity distribution of high-multiplicity events, consistent with jet quenching, the same effect is present in models that do not include the effects of a medium. The simulations suggest that the enhanced acoplanarity results from the bias induced by the high-multiplicity selection towards multi-jet final states.

6.1 The PYTHIA 8 event generator: Monash vs CR mode 2

PYTHIA 8 simulations with the models Monash and the QCD-based color reconnection mode 2 (CR2) are used in the present study. The main features of the models are briefly described in this section.

PYTHIA 8 [97] is one of the most widely used Monte Carlo event generators for high-energy collider physics with particular emphasis on physics related to small collision systems such as pp collisions. It is a parton-based microscopic event generator, where the main event of a pp collision is represented with hard parton scatterings via $2 \rightarrow 2$ matrix elements defined at leading order. It is then complemented by the leading-logarithm approximation of parton showers that includes initial- and final-state radiation. The underlying event is

formed by particles originating from MPI as well as from beam remnants. The hadronisation from partons is performed using the Lund string fragmentation model [98]. In the color reconnection (CR) picture [99], the strings between partons can be rearranged in a way that the total string length is reduced; by which the total charged-particle multiplicity of the event is also reduced. The Monash 2013 tune of PYTHIA 8 [53], created for a better description of minimum-bias and underlying-event observables in pp collisions at the LHC energies, includes the MPI-based colour-reconnection scheme. In this scheme, the colour flow relies on the parton shower-like colour configuration of the beam remnants, and partons are classified based on their origin from the MPI system. However, the colour rules of QCD in the beam remnant are not considered in the MPI-based CR scheme. Recently, a newer QCD-based CR scheme is introduced, which encompasses the minimisation of the string length as well as the colour rules from QCD [100]. This new CR scheme introduces several tuneable parameters and it has been recently shown that the baryon-to-meson ratio from pp collisions at the LHC is better explained by a set of parameters, referred to as CR2 [100–102].

6.2 Flattenicity

Inspired by the recently introduced flattenicity [103], proposed as a new observable to be measured in the next-generation heavy-ion experiment at CERN (ALICE 3) in the LHC Run 5 [104], the present work explores the feasibility of flattenicity measurement using the existing experiments at RHIC and at the LHC. For the definition of flattenicity, the $\eta-\varphi$ phase space was divided into $\mathrm{N_{cell}} = 80$ elementary cells. Given the expected tracking capabilities of ALICE 3, charged particles within $|\eta| < 4$ and $p_{\mathrm{T}} > 0.15\,\mathrm{GeV}/c$ were considered in the calculation of flattenicity. In the cell i, the average transverse momentum was calculated ($p_{\mathrm{T}}^{\mathrm{cell},i}$). Event-by-event, the relative standard deviation defines flattenicity as follows:

$$\rho = \frac{\sqrt{\sum_i (p_{\mathrm{T}}^{\mathrm{cell},i} - \langle p_{\mathrm{T}}^{\mathrm{cell}} \rangle)^2 / \mathrm{N_{cell}}}}{\langle p_{\mathrm{T}}^{\mathrm{cell}} \rangle}, \tag{6.1}$$

Events with jet signals on top of the underlying event are expected to have a large spread in the $p_{\mathrm{T}}^{\mathrm{cell},i}$ values, the opposite is expected in the case in which particles with lower momenta would be isotropically distributed.

However, the main LHC experiments, and even the STAR experiment at RHIC, only have tracking detectors at the central pseudorapidity region. The absence of these detectors in the forward pseudorapidity makes it impossible to use the definition provided in equation (6.1).

Moreover, the calculation of both the event activity (or event shape) and the observable of interest within the same narrow pseudorapidity interval introduces selection biases. The biases are reduced if the activity is determined at forward pseudorapidity [11]. Since most of the experiments can measure the charged particle multiplicity at forward pseudorapidity, the aim of this work is to redefine flattenicity in such a way that it can be measured using the existing detectors. Therefore, charged-particle multiplicity is used instead of the average transverse momentum per cell. In order to guarantee values of flattenicity between 0 and 1, like the standard event shapes (see e.g. [105]), the event shape is defined as follows:

$$\rho_{\mathrm{nch}} = \frac{\sqrt{\sum_i (N_{\mathrm{ch}}^{\mathrm{cell},i} - \langle N_{\mathrm{ch}}^{\mathrm{cell}} \rangle)^2 / \mathrm{N}_{\mathrm{cell}}^2}}{\langle N_{\mathrm{ch}}^{\mathrm{cell}} \rangle}, \tag{6.2}$$

where, $N_{\mathrm{ch}}^{\mathrm{cell},i}$ is the average multiplicity in the elementary cell i and $\langle N_{\mathrm{ch}}^{\mathrm{cell}} \rangle$ is the average of $N_{\mathrm{ch}}^{\mathrm{cell},i}$ in the event. Flattenicity is calculated in the pseudorapidity intervals specified along the paper and using primary charged particles with $p_{\mathrm{T}} > 0$. The additional factor $1/\sqrt{\mathrm{N}_{\mathrm{cell}}}$ guarantees flattenicity to be smaller than unity. Moreover, in order to have a similar meaning of the limits of the new event shape to those used so far (e.g. spherocity), this paper reports results as a function of $1 - \rho_{\mathrm{nch}}$. In such a way that events with $1 - \rho_{\mathrm{nch}} \to 1$ are associated with the isotropic topology, whereas those with $1 - \rho_{\mathrm{nch}} \to 0$ are associated with jet topologies.

In the following studies, the so-called reference flattenicity was calculated considering 16 bins in pseudorapidity (bin size 0.5) and 8 bins in φ (bin size $2\pi/8 \approx 0.79\,\mathrm{rad}$). In order to check the stability of flattenicity with the change of the cell size, a comparison between the reference flattenicity and two variations was cross-checked. The wide cell case consists of 8 and 6 equal-sized intervals in pseudorapidity ($-4 < \eta < 4$) and φ ($0 < \varphi < 2\pi$), respectively. For the narrow cell case, 32 and 25 equal-sized intervals were considered for η and φ, respectively. Figure 6.1 shows the correlation between the flattenicity obtained using a narrow (or wide) binning in $\eta - \varphi$ and the reference flattenicity. Results for non-diffractive pp collisions at $\sqrt{s} = 13.6\,\mathrm{TeV}$ simulated with PYTHIA 8 tune Monash [53] are shown. The relative spread is within 5%, and the average values are consistent within a few percentages. This result shows the stability of flattenicity against variations in the size of the cells. This makes feasible the flattenicity measurement in experiments like ALICE, which would rely on detectors with a given segmentation in η and φ.

Regarding the current capabilities of ALICE, several results as a function of the V0M charged-particle multiplicity have been reported. Each V0 subdetector is segmented into

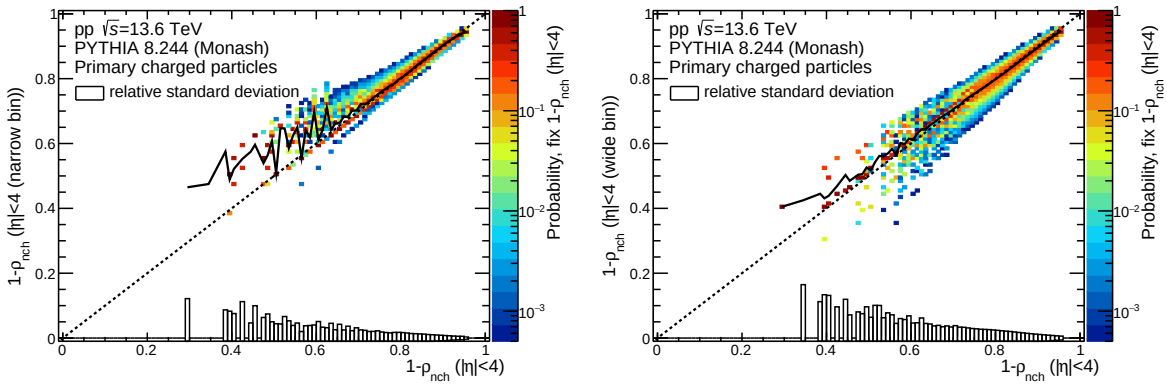

图 6.1: One minus flattenicity calculated using a narrow (wide) binning in $\eta - \varphi$ (read the text for more details) as a function of the reference one minus flattenicity. Results for pp collisions at $\sqrt{s} = 13.6$ TeV simulated with PYTHIA 8 are displayed. The coloured region represents the distribution of events whereas the solid black line is the average value of the y variable over all events with a particular value of the x variable. The boxes around zero indicate the relative standard deviation as a function of the reference flattenicity.

表 6.1: Pseudorapidity intervals covered by the different rings of the V0 detector of ALICE.

Ring	V0C	V0A
1	$-3.7 < \eta < -3.2$	$4.5 < \eta < 5.1$
2	$-3.2 < \eta < -2.7$	$3.9 < \eta < 4.5$
3	$-2.7 < \eta < -2.2$	$3.4 < \eta < 3.9$
4	$-2.2 < \eta < -1.7$	$2.8 < \eta < 3.4$

four rings covering the pseudorapidity intervals listed in Table 6.1. Each ring is divided into eight equal-sized intervals in the azimuth. This yields 64 sectors and the multiplicity in each sector can be used to calculate flattenicity. In addition, the charged-particle multiplicity at mid-pseudorapidity ($|\eta| < 0.8$) which is measured using the TPC of ALICE can be used to constrain the flattenicity of the events. Therefore, a grid defined by the 64 V0 sectors can be complemented with an additional grid within $|\eta| < 0.8$ and $0 < \varphi < 2\pi$ formed by 32 equal-sized cells of side length 0.5 in pseudorapidity and $2\pi/8$ rad in azimuth.

Figure 6.2 shows the correlation between the flattenicity obtained using such a segmentation ($-3.7 < \eta < -1.7$, $|\eta| < 0.8$ and $2.8 < \eta < 5.1$) and the reference flattenicity ($|\eta| < 4$). The experimentally accessible flattenicity is shifted by up to 5% with respect to the reference

flattenicity. For a fixed value of reference flattenicity, the relative standard deviation goes from 10% to less than 1% from low to high $1 - \rho_{\mathrm{nch}}$ values.

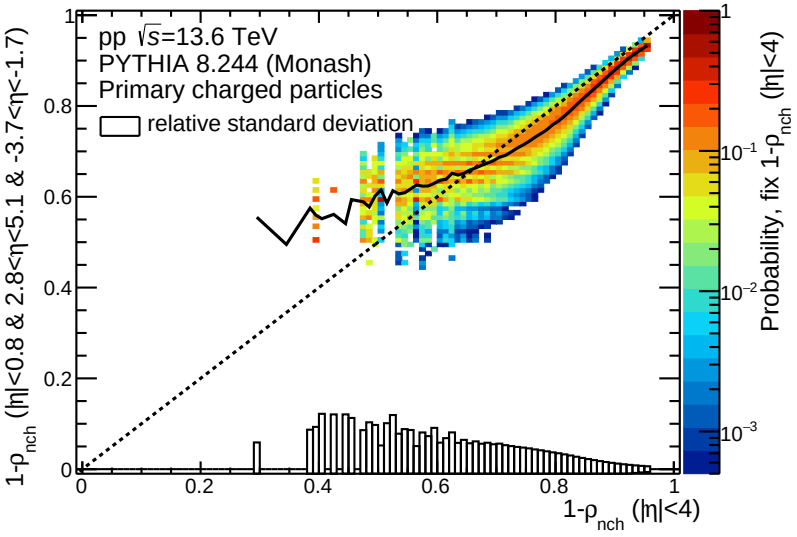

图 6.2: One minus flattenicity calculated using the experimental accessible segmentation of ALICE ($-3.7 < \eta < -1.7$, $|\eta| < 0.8$ and $2.8 < \eta < 5.1$) as a function of the reference one minus flattenicity. Results for pp collisions at $\sqrt{s} = 13.6\,\mathrm{TeV}$ simulated with PYTHIA 8 are displayed. The boxes around zero indicate the relative standard deviation as a function of the reference flattenicity.

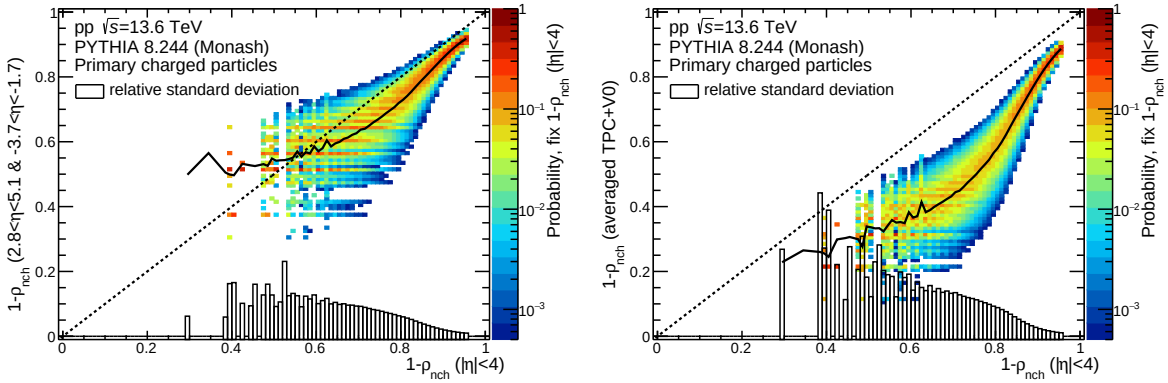

图 6.3: Left (right): one minus flattenicity calculated in the pseudorapidity interval covered by the ALICE V0 (TPC) detector (read the text for more details) as a function of one minus reference flattenicity. Results for pp collisions at $\sqrt{s} = 13.6\,\mathrm{TeV}$ simulated with PYTHIA 8 are displayed. The boxes around zero indicate the relative standard deviation as a function of the reference flattenicity.

The measurement of flattenicity using the segmentation previously defined can be a bit tricky, because the V0 detector provides charge amplitude. Of course, one can develop a strategy to combine the information from the two detectors. However, it would be straightforward to determine flattenicity in a detector-independent way. To this end, Fig. 6.3 explores the correlation between flattenicity calculated in the pseudorapidity region covered by the V0 detector and the reference flattenicity. The figure also displays the situation in which flattenicity is calculated at midpseudorapidity and V0. The combined flattenicity is given by the average of the flattenicity values obtained in each case and it is termed as average TPC+V0. The average flattenicity values obtained in the acceptance of the V0 (V0 +TPC) detector are shifted down by up to 10% (40%) with respect to the reference flattenicity values. On the other hand, for low $1-\rho_{\rm nch}$ values obtained in the acceptance of the V0 (V0 +TPC) detector the relative standard deviation is around 10% (40%) and decreases to less than 1% at high $1-\rho_{\rm nch}$. The effect is explained as due to a bias towards hard pp collisions when the event activity is calculated at midpseudorapidity. In this case, most of the events are associated with multi-jet final states [106]. The result suggests that a measurement of flattenicity in the V0 acceptance would be the best to enhance the sensitivity to the global event shape. This is the approach that is followed in the present work.

6.3 V0M vs flattenicity

Given the definition of flattenicity, the event classifier is expected to be strongly multiplicity dependent. This means that the limit $1-\rho_{\rm nch} \to 1$ can be easily reached by high-multiplicity events, whereas for jet-like events, $1-\rho_{\rm nch} \to 0$ would be easily reached by low-multiplicity events.

This feature of flattenicity is illustrated in Fig. 6.4 where the correlation between $1-\rho_{\rm nch}$ and multiplicity is shown for pp collisions simulated with PYTHIA 8 tune Monash. As in the previous sections, for a fixed multiplicity value the relative standard deviation is displayed. If the multiplicity is determined in pseudorapidity interval covered by the V0 detector, $1-\rho_{\rm nch}$ exhibits a rise even at high multiplicities, where it reaches values above 0.9. The dependence with multiplicity at midpseudorapidity shows saturation at $1-\rho_{\rm nch} = 0.9$ which is reached for intermediate multiplicities ($\mathrm{d}N_{\rm ch}/\mathrm{d}\eta \approx 38$). However, in this case the distribution is slightly wider. The effects can be factorized by performing an analysis both as a function of multiplicity and flattenicity.

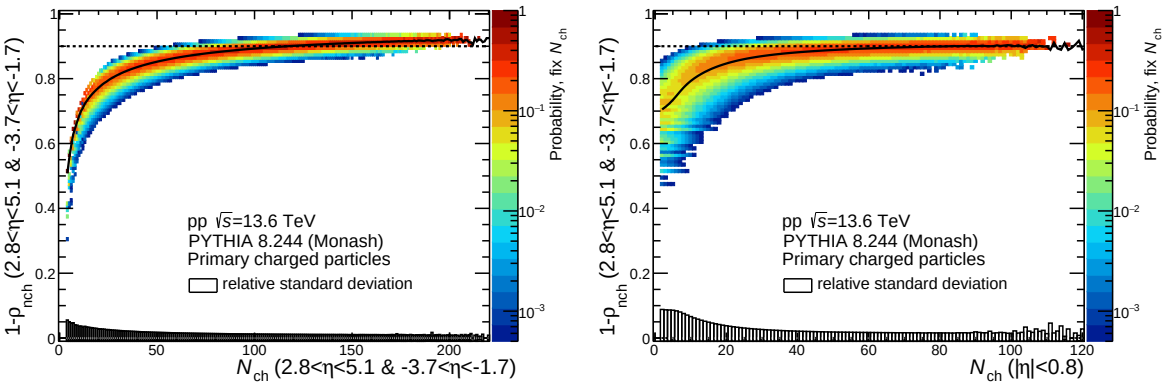

图 6.4: One minus flattenicity calculated in the pseudorapidity region covered by the V0 detector. The event shape is plotted as a function of the charged-particle multiplicity in the same pseudorapidity interval (left) and at midpseudorapidity (right). The width of the distribution is shown as boxes around zero.

表 6.2: Average charged-particle multiplicity density ($\langle \mathrm{d}N_{\mathrm{ch}}/\mathrm{d}\eta \rangle$) at midpseudorapidity ($|\eta| < 0.8$) for different percentile classes defined using flattenicity and V0M.

Event class	$\mathbf{1-\rho_{nch}}$	**V0M**
0-1%	25.0	27.1
1-5%	22.9	23.0
5-10%	18.4	18.7
10-20%	15.6	15.3

Different event classes will be studied based on percentiles of either multiplicity or flattenicity both of them calculated in the pseudorapidity region covered by the V0 detector of ALICE. Table 6.2 shows the average charged-particle multiplicity density at midpseudorapidity for different event classes defined with flattenicity or V0M multiplicity classes. Here, the notation 0-1% means the 1% of the events with the largest values of $1-\rho_{\mathrm{nch}}$ or V0M. For similar percentiles, the average multiplicity values are very close to each other. However, as it will be shown later, the characteristics of the events are very different.

Table 6.2 hints that one can select pp collisions with similar charged-particle multiplicity at midpseudorapidity but originated from different processes. The left-hand side plot shown in Fig. 6.5 displays the correlation between the average number of multi-partonic interactions and the charged-particle multiplicity density at $|\eta| < 0.5$. A comparison of the correlation obtained either using event selection based on flattenicity or V0M multiplicity is displayed. In

both cases, the average number of multi-partonic interactions increases with the increase of the event activity estimator (V0M multiplicity or $1-\rho_{\rm nch}$). Moreover, both selections give a very similar linear correlation, however, slightly higher $\langle N_{\rm mpi}\rangle$ values are observed when the event selection is done with flattenicity. In order to study the "hardness" of the samples, the right-hand side of Fig. 6.5 shows the average transverse momentum of the primary parton-parton scattering ($\hat{p}_{\rm T}$) as a function of the charged-particle multiplicity density. For $\langle {\rm d}N_{\rm ch}/{\rm d}\eta\rangle < 15$ both estimators give the same result. In both cases a fast increase of $\langle\hat{p}_{\rm T}\rangle$ is observed for multiplicity densities below 5, this behavior is followed by a reduction in the slope of $\langle\hat{p}_{\rm T}\rangle$ as a function of the multiplicity density. However, for higher multiplicities a clear deviation is observed between the two event classifiers. The selection in terms of V0M gives a steeper rise of $\langle\hat{p}_{\rm T}\rangle$ with the charged-particle density than that observed for the selection based on flattenicity. The average $\hat{p}_{\rm T}$ is expected to increase with the increase of the multi-parton interaction activity. The more the number of semi-hard scatterings the higher the probability to pick a slightly harder parton-parton scattering. At $\langle {\rm d}N_{\rm ch}/{\rm d}\eta\rangle = 30$ the average hard $p_{\rm T}$ is 16% higher for events selected with V0M than that for events selected with flattenicity. The difference seems to increase at higher multiplicity densities. The results suggest that V0M and flattenicity are nearly equally sensitive to MPI, but flattenicity reduces the bias towards hard pp collisions.

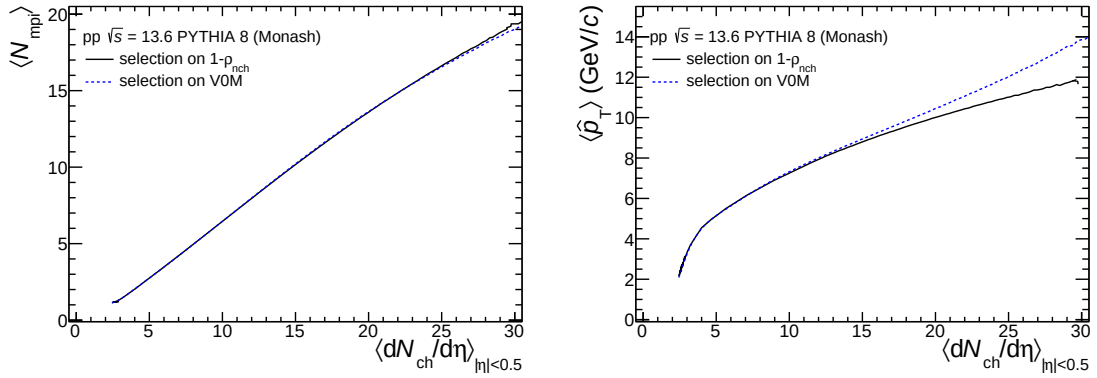

图 6.5: The average number of multi-partonic interactions (transverse momentum of the primary partonic scattering) as a function of the charged-particle multiplicity density at midpseudorapidity, $|\eta| < 0.5$, is shown in the left (right) hand side panel. Results for pp collisions at $\sqrt{s} = 13.6$ TeV simulated with PYTHIA 8 tune Monash are displayed. The solid line indicates the correlation when the event selection is done in $1-\rho_{\rm nch}$ classes, whereas, the dotted line indicate the correlation when the event classification is performed as a function of the V0M estimator.

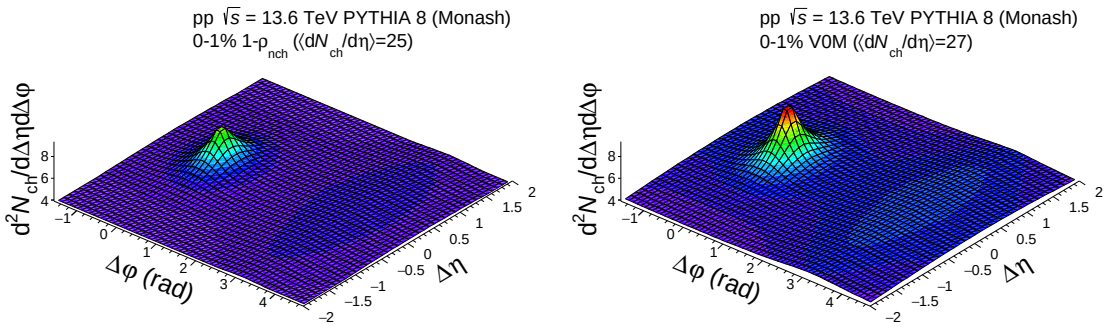

图 6.6: Angular correlations between associated charged particles and the leading charged particle. The charged-particle yield is presented as a function of the angular separation $\Delta\varphi$ and $\Delta\eta$ for pp collisions at $\sqrt{s} = 13.6\,\text{TeV}$ simulated with PYTHIA 8 tune Monash. The correlation for the 0-1% $1 - \rho_{\text{nch}}$ (V0M) event class is shown in the left (right) panel.

Figure 6.6 shows the angular correlations between the leading particle and associated particles. The leading particle is the one with the largest transverse momentum of the event. If $p_{\text{T}}^{\text{trig}}$ is the transverse momentum of the leading particle, then the associated particles are all those charged particles whose transverse momentum is lower than $p_{\text{T}}^{\text{trig}}$. In Fig. 6.6, the charged-particle yield is reported as a function of $\Delta\varphi = \varphi - \varphi^{\text{trig}}$ and $\Delta\eta = \eta - \eta^{\text{trig}}$, where η and φ are the pseudorapidity and azimuthal angle of the associated particles, respectively. The left-hand (right-hand) side plot shows the angular correlation for the 0-1% $1-\rho_{\text{nch}}$ (V0M) class in pp collisions at $\sqrt{s} = 13.6\,\text{TeV}$. According to table 6.2, the charged-particle multiplicity density at midpseudorapidity is around 26 for these event classes. While the selection based on V0M gives prominent jet structures at $\Delta\varphi = 0$ and $\Delta\varphi = \pi$, for the pp sample selected with flattenicity, the near- and away-side peaks are significantly smaller than those observed when the selection is done in terms of V0M. This result is consistent with the isolation of more isotropic pp collisions in flattenicity classes than in V0M classes. Therefore, the event classifier is able to select high multiplicity pp collisions originated by several soft parton-parton scatterings producing a nearly homogeneous distribution of particles in both $\Delta\eta$ and $\Delta\varphi$. In PYTHIA 8 there are always $2 \to 2$ processes, therefore rather small near- and away-side peaks are observed. The size of the peaks are significantly smaller than those observed for pp collisions with similar charged-particle multiplicities but originated from harder processes.

In summary, the sensitivity to MPI is still kept if multiplicity is used instead of average transverse momentum in the calculation of flattenicity. Moreover, with the actual detectors

of the ALICE experiment, the analysis as a function of flattenicity seems to be feasible. In the next section, the light- and heavy-flavored hadron productions are studied for different $1 - \rho_{\rm nch}$ event classes.

6.4 Light- and heavy-flavor hadron production as a function of flattenicity

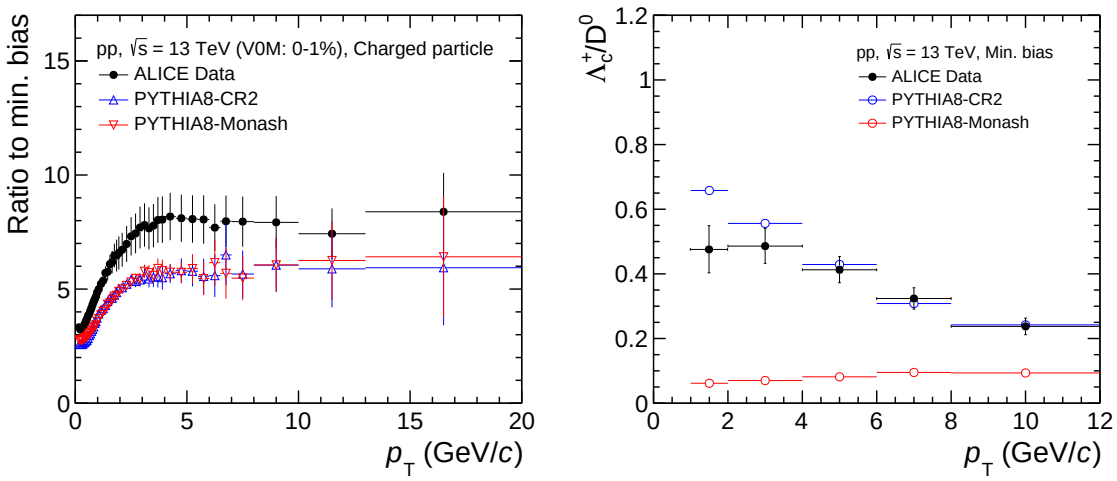

图 6.7: The ratio of charged particle spectra in $0 - 1\%$ V0M class to minimum bias in pp collisions with ALICE at $\sqrt{s} = 13$ TeV are compared with the Pythia 8 Monash and CR2 predictions (left). The $\Lambda_{\rm c}^{+}/{\rm D}^{0}$ ratios in pp collisions with ALICE are compared to Pythia 8 Monash and CR2 tunes (right).

In this section, results using the color reconnection mode 2 of PYTHIA 8 is used to generate pp collisions at the LHC energies. This model is chosen given that it better describes the identified particle production than the Monash tune. The CR2 model includes junctions, which fragment into baryons, leading to an increased baryon production as compared to Monash tune. For example, figure 6.7 left panel shows the ratio between the $p_{\rm T}$ spectrum of charged particles in the 0-1% V0 multiplicity class to the one measured in minimum bias pp collisions at $\sqrt{s} = 13$ TeV by ALICE [81]. The data are compared with predictions from Pythia 8 Monash and color reconnection mode 2 (CR2). Both the models qualitatively reproduce the data very well, which shows the evolution of the spectral shape up to $p_{\rm T} \simeq 5$ GeV/c and the ratio is flat at high $p_{\rm T}$. Figure 6.7 right panel shows the measured $p_{\rm T}$-differential $\Lambda_{\rm c}^{+}/{\rm D}^{0}$ ratio in minimum bias collisions [107] along with model predictions. In particular, the CR2

model shows a very good agreement with the data.

Figure 6.8 shows the charged-pion p_{T} spectrum in the 0-1% V0M multiplicity class normalized to the charged-pion p_{T} spectrum in minimum-bias collisions.

A comparison with the 0-1% $1-\rho_{\mathrm{nch}}$ class is shown. While at low transverse momentum the ratios are very close to each other showing an increase up to $p_{\mathrm{T}} \approx 2\,\mathrm{GeV}/c$, at higher transverse momentum the ratios follow different trends. On one hand, the ratio for the 0-1% V0M class exhibits a continuous rise with increasing p_{T}; on the other hand, the ratio for the 0-1% $1-\rho_{\mathrm{nch}}$ class reaches a maximum that is followed by a reduction reaching a constant value of around 6. The ratios as a function of $1-\rho_{\mathrm{nch}}$ show a similar behavior as those reported as a function of the number of multi-partonic interactions [33]. The effect has been attributed to color reconnection, which according to Ref. [108] should originate a mass effect. The mass effect is tested using protons instead of pions. Figure 6.8 shows analogous ratios for protons. For similar event classes the effect gets significantly enhanced. Moreover, for the 0-1% $1-\rho_{\mathrm{nch}}$ class a prominent bump structure is observed at intermediate transverse momentum. The effect is hidden in the 0-1% V0M class given the presence of harder processes that produce a small increase of the ratio for $p_{\mathrm{T}} > 6\,\mathrm{GeV}/c$. The bump structure has not been observed in data since all the analyses have been performed so far as a function of the V0M multiplicity.

Last but not least, it has been reported that the p_{T}-differential baryon-to-meson ratios including $\Lambda_{\mathrm{c}}^{+}/\mathrm{D}^{0}$, p/π and $\Lambda/\mathrm{K}_{\mathrm{s}}^{0}$ exhibit remarkable similarities. The ratios show a clear decrease with increasing p_{T} in both pp and p–Pb collisions in the range $2 < p_{\mathrm{T}} < 12\,\mathrm{GeV}/c$. At low p_{T}, predictions that include additional color-reconnection mechanisms beyond the leading-color approximation (CR2) describe rather well the overall features [109]. Figure 6.9 shows the p/π, $\Lambda/\mathrm{K}_{\mathrm{s}}^{0}$ and $\Lambda_{\mathrm{c}}^{+}/\mathrm{D}^{0}$ ratios as a function of the transverse momentum using V0M and 1-ρ_{nch} classes. All these ratios exhibit remarkably similar characteristics with a decreasing trend after $p_{\mathrm{T}} \geq$ 2-3 GeV/c. With the selection of 0-5% V0M or 1-ρ_{nch}, we see an enhancement of these ratios at intermediate p_{T} that is around 18%, 20%, and 35% higher for p/π, $\Lambda/\mathrm{K}_{\mathrm{s}}^{0}$ and $\Lambda_{\mathrm{c}}^{+}/\mathrm{D}^{0}$ as compared to minimum-bias pp collisions, respectively. One of the interesting observations is the shift of the peak structure towards higher momentum, which is often attributed to the radial flow effect for light-flavor particle production [110]. The 0-1% 1-ρ_{nch} class for the highest 0-5% V0M classes selects events with an isotropic event topology. From Fig. 6.9, a clear picture is evolved where the baryon to meson ratio is further enhanced and for the first time, we observe a clear peak structure for $\Lambda_{\mathrm{c}}^{+}/\mathrm{D}^{0}$ for pp collisions, which

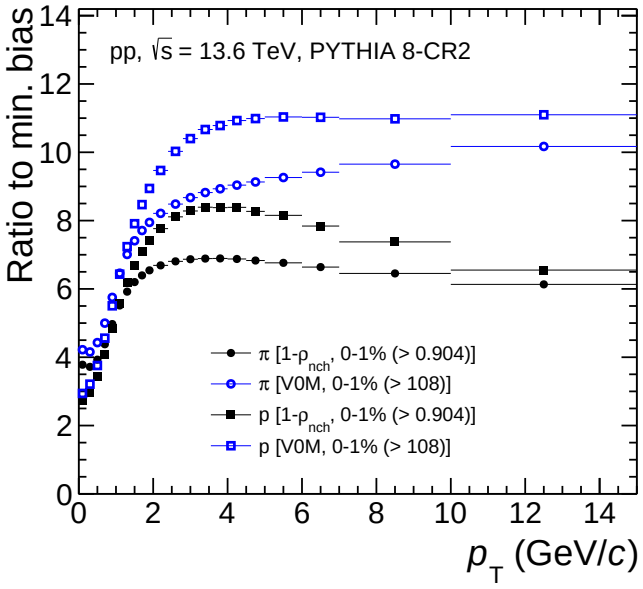

图 6.8: Transverse momentum differential yield in the 0-1% 1-$\rho_{\rm nch}$ (full markers) and 0-1% V0M multiplicity (empty markers) class normalized to the yield in minimum-bias pp collisions. Results for pions and protons are displayed in round and square markers, respectively. The $p_{\rm T}$ spectra were calculated at mid-rapidity ($|y| < 0.5$) in pp collisions at $\sqrt{s} = 13.6$ TeV simulated with PYTHIA 8.

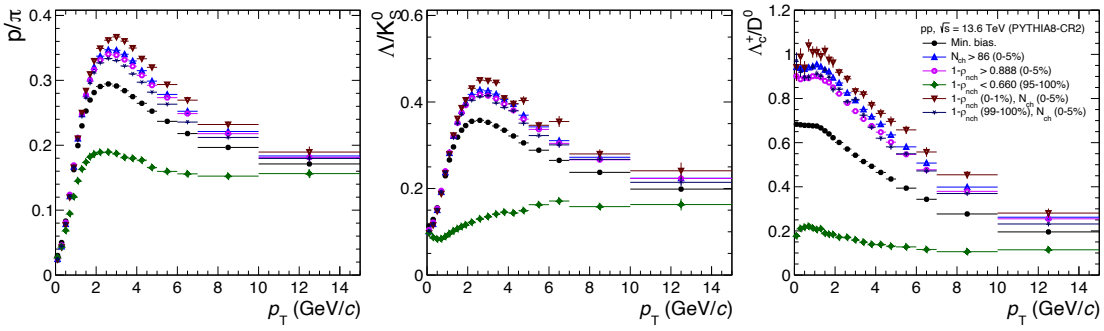

图 6.9: $p_{\rm T}$-differential baryon to meson ratios for particles containing light, strange and charm quarks, respectively. The selection of events is based on V0M multiplicity and 1-$\rho_{\rm nch}$ classes.

is earlier observed in p–Pb collisions by ALICE collaboration [109]. This enhancement is suppressed for p/π ratio for the 95-100% 1-$\rho_{\rm nch}$ event class that corresponds to jet topologies, whereas for $\Lambda/{\rm K}^0_{\rm s}$ and $\Lambda^+_{\rm c}/{\rm D}^0$ the peak structure at intermediate $p_{\rm T}$ is completely absent.

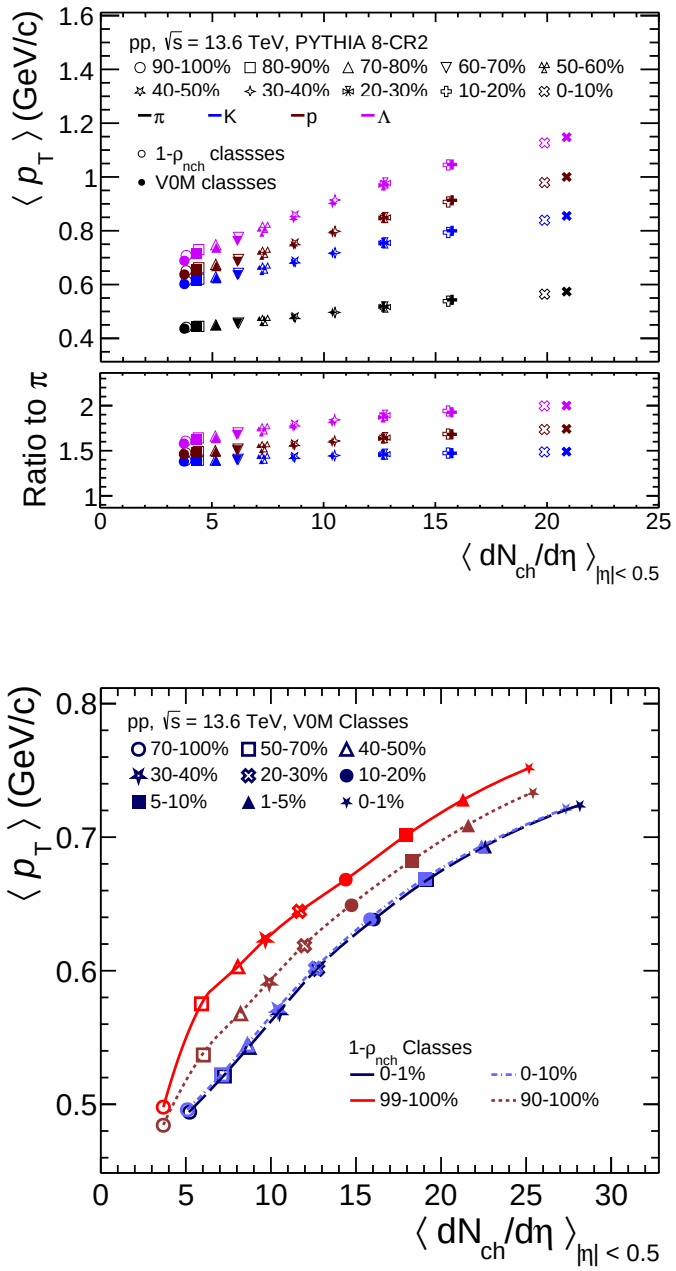

图 6.10: Mean transverse momentum of identified particles calculated in $|y| < 0.8$ as a function of the charged-particle multiplicity at mid-rapidity (top). Here, we consider both V0M and 1-$\rho_{\rm nch}$ classes to see the effect of the mass-ordering of $\langle p_{\rm T} \rangle$ on multiplicity and event-shape variable. The mean transverse momentum of the charged particles in V0M classes is shown as a function of the charged-particle multiplicity in the mid-rapidity, $|\eta| < 0.5$ for 1% and 10% top and bottom events in 1-$\rho_{\rm nch}$ classes (bottom).

The section of hard events (95-100% 1-$\rho_{\rm nch}$) shows a similar trend for $\Lambda/\mathrm{K}^0_\mathrm{s}$ ratio in jets as a function of p_T [111]. The selection of events based on charged-particle multiplicity or event topology should reflect on the $\langle p_\mathrm{T}\rangle$ of the identified particles. The left panel of Fig. 6.10 shows the $\langle p_\mathrm{T}\rangle$ of π, K, p and Λ as a function of charged-particle multiplicity at mid-rapidly ($|y| < 0.8$) in the V0M and 1-$\rho_{\rm nch}$ event classes. A clear mass dependant evolution of $\langle p_\mathrm{T}\rangle$ is observed as a function of charged-particle multiplicity. However, we do not see a strong dependence on V0M or 1-$\rho_{\rm nch}$ event classes although we see harder spectra in the case of V0M event classes for π and p in Fig. 6.8. This is because the spectral shape doesn't significantly change at lower p_T, which is the dominant factor in the evaluation of the $\langle p_\mathrm{T}\rangle$. We further extend this study for charged particles by selecting 0-1% and 0-10% 1- $\rho_{\rm nch}$ event classes together with V0M selection. The $\langle p_\mathrm{T}\rangle$ of charged particles are quite similar for both subclasses and there is mild spread on the charged-particle multiplicity at mid-rapidity as seen from Fig. 6.10. However, by selecting 99-100% and 90-100% 1- $\rho_{\rm nch}$ event classes, a higher $\langle p_\mathrm{T}\rangle$ is observed with the bottom 1%, which is in agreement with the interpretation of selecting hard events.

第 7 章 Conclusions

The $N_{\rm ch}^{\rm T}$, $N_{\rm ch}^{\rm Tmax}$, and $N_{\rm ch}^{\rm Tmin}$ distributions have been measured in pp collisions at $\sqrt{s}$ = 2.76, 5.02, 7, and 13 TeV. In the transverse region, for $N_{\rm ch}^{\rm T} < 5$, the $N_{\rm ch}^{\rm T}$ distributions are energy independent within $\sim$ 25%. A strong energy dependence is observed at higher $N_{\rm ch}^{\rm T}$ values, we also observe that the higher multiplicity reach is achieved at higher energies. For the other two regions, a smaller energy dependence of $N_{\rm ch}^{\rm Tmin}$ distributions than that for the $N_{\rm ch}^{\rm Tmax}$ distributions is observed, especially for the first bin.

In order to understand the particle production in the three regions, the multiplicity distributions were fitted with NBD. For the transverse region, we found that a single NBD was enough to describe the data. On one hand, a bump structure, which can be understood as a consequence of fluctuations on impact parameter, is not observed at high $N_{\rm ch}^{\rm T}$ for our result, compared to the inclusive multiplicity distributions in MB pp collisions. It is consistent with our expectation of removing double peaks by selecting events with $p_{\rm T}^{\rm trig}$ above 5 GeV/c which guarantees a relatively small average impact parameter (close to zero) of the sample and thus reduces the fluctuations on impact parameter. On the other hand, the result corroborates the interpretation that the transverse region mostly considers particles produced by UE (mini-jets=MPI), i.e., the hard component was explicitly exclude the multiplicity estimator.

The $N_{\rm ch}^{\rm Tmax}$ distributions cannot be described with single NBDs at high $N_{\rm ch}^{\rm Tmax}$ values, which is consistent with the enhancement of hard physics (ISR-FSR) in the trans-max region. Moreover, according with the parameterisation of $N_{\rm ch}^{\rm Tmax}$, the average multiplicity $\langle n \rangle$ increases with $\sqrt{s}$ and the relative dispersion k decreases with $\sqrt{s}$, which could be also attributed to the presence of hard physics that is more important at high energies.

In contrast, the $N_{\rm ch}^{\rm Tmin}$ distributions are well described with single NBDs, even with a better agreement than the parameterisation of $N_{\rm ch}^{\rm T}$ distributions, suggesting that the MPI-component dominates in the trans-min region. In terms of the relative dispersion, it is approximately a constant with $\sqrt{s}$ in the trans-min region (as well as the transverse region), i.e., $N_{\rm ch}^{\rm Tmin}$ ($N_{\rm ch}^{\rm T}$) follows the KNO scaling.

To further assess the validity of KNO scaling, the multiplicity distributions in KNO variables are also studied. In the transverse region, a KNO-like scaling holds for $0 < R_{\rm T} < 3$, whereas for higher $R_{\rm T}$ values ($R_{\rm T} > 3$), the KNO-like scaling is broken. From an analysis aimed at measuring the MPI, it was observed that for $N_{\rm ch}/\langle N_{\rm ch} \rangle$ >3–4, the number of MPI as a function of $N_{\rm ch}/\langle N_{\rm ch} \rangle$ deviates from the linear trend suggesting the presence of high-multiplicity jets. The presence of high-multiplicity jets may also explain the violation of

KNO-like scaling. This result can be interpreted that, for $R_{\mathrm{T}} < 3$, UE is isotropic in the transverse, toward, and away regions, while for $R_{\mathrm{T}} > 3$ — UE is not isotropic — amounts of "hard ISR-FSR" are induced around di-jets to achieve high multiplicity in a event since the probability to produce high-multiplicity events is quite small in a given transverse momentum transfer.

For the trans-max region, the $R_{\mathrm{T}}^{\mathrm{max}}$distributions are qualitatively similar to those observed for the transverse region. On the other hand, for the trans-min region, the KNO-like scaling holds in a wider $R_{\mathrm{T}}^{\mathrm{min}}$interval ($0 < R_{\mathrm{T}}^{\mathrm{min}} < 4$) with a better agreement, whereas for $R_{\mathrm{T}}^{\mathrm{min}} > 4$ the KNO-like scaling is still broken. Moreover, a higher reach is achieved, especially for $R_{\mathrm{T}}^{\mathrm{min}} > 6$, a larger violation is observed which might also be attributed by high-multiplicity jets.

The centre-of-mass energy dependence of average multiplicity densities is also discussed. In the transverse region, our results in pp collisions at $\sqrt{s} = 2.76$, 5.02, 7, and 13 TeV follow the trend of existing data points from various experiments, which can be described by the parameterisation of the form $s^{0.27} + 0.14\log(s)$. The power-law term and the logarithmic term describe the MPI- and ISR-FSR-sensitive topological region of the collision, respectively. This power-law behaviour is consistent with the centre-of-mass energy dependence of the parameter which regulates MPI in event generators like PYTHIA.

Overall, for multiplicity distributions and KNO variables, PYTHIA 8/Monash and EPOS LHC describe data well at low multiplicity. For higher multiplicities, both models describe the data within 1–2 sigmas, and a better agreement is observed at higher energies. It is important to mention that PYTHIA 8/Monash does slightly better than EPOS LHC for all the energies. As to the average multiplicity densities as a function of $\sqrt{s}$, for the transverse and trans-max regions, PYTHIA 8/Monash describes data within one sigma, especially for low energies, while EPOS LHC deviates from data except for the data point at 13 TeV. For the trans-min region, both models describe data quite well among different centre-of-mass energies.

Regarding the UE analysis in pp and p–Pb collisions at the same centre-of-mass energy per nucleon pair ($\sqrt{s_{\mathrm{NN}}} = 5.02$ TeV). For pp collisions, the UE observables behave in the same way as reported at lower and higher centre-of-mass energies. For instance, the number density sharply rises with increasing $p_{\mathrm{T}}^{\mathrm{trig}}$ up to 5 GeV/c and subsequently flattens at higher $p_{\mathrm{T}}^{\mathrm{trig}}$. In terms of the data-to-model comparisons, PYTHIA 8/Monash are able to capture the $p_{\mathrm{T}}^{\mathrm{trig}}$ dependence of particle densities in the three topological regions (toward, away, and

transverse regions). However, EPOS LHC gives a distinct prediction at $p_{\mathrm{T}}^{\mathrm{trig}} \approx 3\,\mathrm{GeV}/c$ where a bump exits in the three regions, but it does not appear in data.

For p–Pb collisions, the UE observables exhibit a similar behaviour as seen in pp collisions. In the transverse region, the number density also saturates since $p_{\mathrm{T}}^{\mathrm{trig}} \approx 5\,\mathrm{GeV}/c$. PYTHIA 8/Angantyr captures the saturation shape, while EPOS LHC fails to predict this saturation effect. And the number density is underestimated in both models. Regarding the toward and away regions, the relative increase of the event activity in the $p_{\mathrm{T}}^{\mathrm{trig}}$ interval 5–40 GeV/c is smaller than that in pp collisions. For $p_{\mathrm{T}}^{\mathrm{trig}} > 8\,\mathrm{GeV}/c$, the number density is underestimated by PYTHIA 8/Angantyr and EPOS LHC. For $p_{\mathrm{T}}^{\mathrm{trig}} < 3\,\mathrm{GeV}/c$, the number density is qualitatively described by EPOS LHC, whereas it is overestimated in PYTHIA 8/Angantyr by up to 30%. In addition, a bump structure is predicted at $p_{\mathrm{T}}^{\mathrm{trig}} \approx 4\,\mathrm{GeV}/c$ in EPOS LHC, which does not appear in data.

Concerning the plans for future analyses. Charged-particle flattenicity was proposed as a new event activity classifier with reduced sensitivity towards final state multi-jet typologies. The first analysis using this tool is ongoing, and it is expected to be used as a tool to classify the collisions in terms of the average impact parameter of the collision.

参考文献

[1] Siegfried Bethke. α_s 2002. *Nucl. Phys. B Proc. Suppl.*, 121:74–81, 2003.

[2] Zhongbao Yin. *High p_T Physics in Heavy Ion Collisions at $\sqrt{s_{NN}} = 200$ GeV*. PhD thesis, Bergen U., 2004.

[3] F. Karsch. Lattice QCD at high temperature and density. *Lect. Notes Phys.*, 583:209–249, 2002.

[4] Wit Busza, Krishna Rajagopal, and Wilke van der Schee. Heavy Ion Collisions: The Big Picture, and the Big Questions. *Ann. Rev. Nucl. Part. Sci.*, 68:339–376, 2018.

[5] The ALICE experiment – A journey through QCD. 11 2022.

[6] Renu Bala, Irais Bautista, Jana Bielcikova, and Antonio Ortiz. Heavy-ion physics at the LHC: Review of Run I results. *Int. J. Mod. Phys. E*, 25(07):1642006, 2016.

[7] Jaroslav Adam et al. Anisotropic flow of charged particles in Pb-Pb collisions at $\sqrt{s_{\rm NN}} =$ 5.02 TeV. *Phys. Rev. Lett.*, 116(13):132302, 2016.

[8] Jaroslav Adam et al. Enhanced production of multi-strange hadrons in high-multiplicity proton-proton collisions. *Nature Phys.*, 13:535–539, 2017.

[9] James L. Nagle and William A. Zajc. Small System Collectivity in Relativistic Hadronic and Nuclear Collisions. *Ann. Rev. Nucl. Part. Sci.*, 68:211–235, 2018.

[10] Vardan Khachatryan et al. Evidence for collectivity in pp collisions at the LHC. *Phys. Lett. B*, 765:193–220, 2017.

[11] Shreyasi Acharya et al. Multiplicity dependence of light-flavor hadron production in pp collisions at $\sqrt{s} = 7$ TeV. *Phys. Rev. C*, 99(2):024906, 2019.

[12] Antonio Ortiz Velasquez, Peter Christiansen, Eleazar Cuautle Flores, Ivonne Maldonado Cervantes, and Guy Paić. Color Reconnection and Flowlike Patterns in *pp* Collisions. *Phys. Rev. Lett.*, 111(4):042001, 2013.

[13] Tim Martin, Peter Skands, and Sinead Farrington. Probing Collective Effects in Hadronisation with the Extremes of the Underlying Event. *Eur. Phys. J. C*, 76(5):299, 2016.

[14] Antonio Ortiz and Lizardo Valencia Palomo. Probing color reconnection with underlying event observables at the LHC energies. *Phys. Rev. D*, 99(3):034027, 2019.

[15] Valentina Zaccolo. Particle production as a function of underlying-event activity measured with ALICE at the LHC. *Springer Proc. Phys.*, 250:245–248, 2020.

[16] Adrian Nassirpour. Probing strangeness production in small systems through new multi-differential measurements with ALICE at the LHC. *J. Phys. Conf. Ser.*, 1602(1):012007, 2020.

[17] Gyula Bencédi, Antonio Ortiz, and Sushanta Tripathy. Apparent modification of the jet-like yield in proton-proton collisions with large underlying event. *J. Phys. G*, 48(1):015007, 2020.

[18] Rick Field. The Underlying Event in Hadronic Collisions. *Ann. Rev. Nucl. Part. Sci.*, 62(1):453–483, 2012.

[19] Torbjorn Sjostrand and Maria van Zijl. A Multiple Interaction Model for the Event Structure in Hadron Collisions. *Phys. Rev. D*, 36:2019, 1987.

[20] T. Åkesson et al. Double Parton Scattering in pp Collisions at $\sqrt{s} = 63\,\mathrm{GeV}$. *Z. Phys. C*, 34:163, 1987.

[21] F. Abe et al. Double parton scattering in $\overline{p}p$ collisions at $\sqrt{s} = 1.8\,\mathrm{TeV}$. *Phys. Rev. D*, 56:3811–3832, Oct 1997.

[22] V. M. Abazov et al. Double parton interactions in γ+3 jet events in $p\bar{p}$ collisions $\sqrt{s} = 1.96\,\mathrm{TeV}$. *Phys. Rev. D*, 81:052012, 2010.

[23] D. Acosta et al. The underlying event in hard interactions at the Tevatron $\bar{p}p$ collider. *Phys. Rev. D*, 70:072002, 2004.

[24] T. Aaltonen et al. Studying the Underlying Event in Drell-Yan and High Transverse Momentum Jet Production at the Tevatron. *Phys. Rev. D*, 82:034001, 2010.

[25] Jaroslav Adam et al. Underlying event measurements in $p + p$ collisions at $\sqrt{s} = 200$ GeV at RHIC. *Phys. Rev. D*, 101(5):052004, 2020.

[26] Georges Aad et al. Measurement of underlying event characteristics using charged particles in pp collisions at $\sqrt{s} = 900GeV$ and 7 TeV with the ATLAS detector. *Phys. Rev. D*, 83:112001, 2011.

[27] Betty Abelev et al. Underlying Event measurements in pp collisions at $\sqrt{s} = 0.9$ and 7 TeV with the ALICE experiment at the LHC. *JHEP*, 07:116, 2012.

[28] Georges Aad et al. Measurement of the underlying event in jet events from 7 TeV proton-proton collisions with the ATLAS detector. *Eur. Phys. J. C*, 74(8):2965, 2014.

[29] Betty Abelev et al. Multiplicity dependence of two-particle azimuthal correlations in pp collisions at the LHC. *JHEP*, 09:049, 2013.

[30] Vardan Khachatryan et al. Measurement of the underlying event activity using charged-particle jets in proton-proton collisions at sqrt(s) = 2.76 TeV. *JHEP*, 09:137, 2015.

[31] Morad Aaboud et al. Measurement of charged-particle distributions sensitive to the underlying event in $\sqrt{s} = 13$ TeV proton-proton collisions with the ATLAS detector at the LHC. *JHEP*, 03:157, 2017.

[32] Shreyasi Acharya et al. Underlying Event properties in pp collisions at $\sqrt{s} = 13$ TeV. *JHEP*, 04:192, 2020.

[33] Antonio Ortiz, Antonio Paz, José D. Romo, Sushanta Tripathy, Erik A. Zepeda, and Irais Bautista. Multiparton interactions in *pp* collisions from machine learning-based regression. *Phys. Rev. D*, 102(7):076014, 2020.

[34] Antonio Ortiz and Erik A. Zepeda. Extraction of the multiplicity dependence of multi-parton interactions from LHC pp data using machine learning techniques. *J. Phys. G*, 48(8):085014, 2021.

[35] Shreyasi Acharya et al. Measurements of long-range two-particle correlation over a wide pseudorapidity range in p–Pb collisions at $\sqrt{s_{\mathrm{NN}}} = 5.02$ TeV. *JHEP*, 01:056, 2024.

[36] Antonio Ortiz and Lizardo Valencia Palomo. Universality of the underlying event in pp collisions. *Phys. Rev. D*, 96(11):114019, 2017.

[37] Antonio Ortiz, Arvind Khuntia, Omar Vázquez-Rueda, Sushanta Tripathy, Gyula Bencedi, Suraj Prasad, and Feng Fan. Unveiling the effects of multiple soft partonic interactions in pp collisions at s=13.6 TeV using a new event classifier. *Phys. Rev. D*, 107(7):076012, 2023.

[38] Shreyasi Acharya et al. Study of charged particle production at high pT using event topology in pp, p–Pb and Pb–Pb collisions at sNN=5.02TeV. *Phys. Lett. B*, 843:137649, 2023.

[39] G. Arnison et al. Hadronic Jet Production at the CERN proton - antiproton Collider. *Phys. Lett. B*, 132:214, 1983.

[40] C. Albajar et al. Production of Low Transverse Energy Clusters in anti-p p Collisions at $\sqrt{s}$ = 0.2-0.9 TeV and their Interpretation in Terms of QCD Jets. *Nucl. Phys. B*, 309:405–425, 1988.

[41] C. Albajar et al. A Study of the General Characteristics of $p\bar{p}$ Collisions at $\sqrt{s}$ = 0.2 TeV to 0.9 TeV. *Nucl. Phys. B*, 335:261–287, 1990.

[42] T. Affolder et al. Charged Jet Evolution and the Underlying Event in $p\bar{p}$ Collisions at 1.8 TeV. *Phys. Rev. D*, 65:092002, 2002.

[43] Feng Fan. Particle production as a function of underlying-event activity and very forward energy with ALICE. *EPJ Web Conf.*, 276:01009, 2023.

[44] Gyula Bencedi, Antonio Ortiz, and Antonio Paz. Disentangling the hard gluon bremsstrahlung effects from the relative transverse activity classifier in pp collisions. *Phys. Rev. D*, 104(1):016017, 2021.

[45] Z. Koba, Holger Bech Nielsen, and P. Olesen. Scaling of multiplicity distributions in high-energy hadron collisions. *Nucl. Phys. B*, 40:317–334, 1972.

[46] Sandor Hegyi. KNO scaling 30 years later. *Nucl. Phys. B Proc. Suppl.*, 92:122–129, 2001.

[47] Jan Fiete Grosse-Oetringhaus and Klaus Reygers. Charged-Particle Multiplicity in Proton-Proton Collisions. *J. Phys. G*, 37:083001, 2010.

[48] J. Dias de Deus, C. Pajares, and C. A. Salgado. Production associated to rare events in high-energy hadron hadron collisions. *Phys. Lett. B*, 408:417–421, 1997.

[49] G. J. Alner et al. An Investigation of Multiplicity Distributions in Different Pseudorapidity Intervals in anti-p p Reactions at a CMS Energy of 540-GeV. *Phys. Lett. B*, 160:193–198, 1985.

[50] G. J. Alner et al. Scaling Violations in Multiplicity Distributions at 200-GeV and 900-GeV. *Phys. Lett. B*, 167:476–480, 1986.

[51] Jaroslav Adam et al. Charged-particle multiplicities in proton–proton collisions at $\sqrt{s}$ = 0.9 to 8 TeV. *Eur. Phys. J. C*, 77(1):33, 2017.

[52] Alberto Giovannini and Roberto Ugoccioni. Possible scenarios for soft and semihard components structure in central hadron hadron collisions in the TeV region. *Phys. Rev. D*, 59:094020, 1999. [Erratum: Phys.Rev.D 69, 059903 (2004)].

[53] Peter Skands, Stefano Carrazza, and Juan Rojo. Tuning PYTHIA 8.1: the Monash 2013 Tune. *Eur. Phys. J. C*, 74(8):3024, 2014.

[54] T. Pierog, Iu. Karpenko, J. M. Katzy, E. Yatsenko, and K. Werner. EPOS LHC: Test of collective hadronization with data measured at the CERN Large Hadron Collider. *Phys. Rev. C*, 92(3):034906, 2015.

[55] Christian Bierlich et al. A comprehensive guide to the physics and usage of PYTHIA 8.3. *SciPost Phys. Codeb.*, 2022:8, 2022.

[56] Klaus Werner, Fu-Ming Liu, and Tanguy Pierog. Parton ladder splitting and the rapidity dependence of transverse momentum spectra in deuteron-gold collisions at RHIC. *Phys. Rev. C*, 74:044902, 2006.

[57] H. J. Drescher, M. Hladik, S. Ostapchenko, T. Pierog, and K. Werner. Parton based Gribov-Regge theory. *Phys. Rept.*, 350:93–289, 2001.

[58] K. Werner. Strings, pomerons, and the venus model of hadronic interactions at ultra-relativistic energies. *Phys. Rept.*, 232:87–299, 1993.

[59] N.N. Kalmykov, S.S. Ostapchenko, and A.I. Pavlov. Quark-gluon-string model and eas simulation problems at ultra-high energies. *Nuclear Physics B - Proceedings Supplements*, 52(3):17–28, 1997.

[60] Christian Wolfgang Fabjan et al. ALICE: Physics Performance Report. *J. Phys. G*, 32:1295–2040, 2006.

[61] K. Aamodt et al. The ALICE experiment at the CERN LHC. *JINST*, 3:S08002, 2008.

[62] G. Dellacasa et al. ALICE technical design report of the inner tracking system (ITS). Jun 1999.

[63] The alice tpc, a large 3-dimensional tracking device with fast readout for ultra-high multiplicity events. *Nuclear Instruments and Methods in Physics Research Section A: Accelerators, Spectrometers, Dete ctors and Associated Equipment*, 622(1):316–367, 2010.

[64] G. Dellacasa et al. ALICE: Technical design report of the time projection chamber. Jan 2000.

[65] Betty Bezverkhny Abelev et al. Performance of the ALICE Experiment at the CERN LHC. *Int. J. Mod. Phys. A*, 29:1430044, 2014.

[66] John Erthal Gaiser. Charmonium Spectroscopy From Radiative Decays of the J/ψ and ψ'. Other thesis, 8 1982.

[67] Veikko Karimäki. Effective Vertex Fitting. 6 1997.

[68] G. Agakichiev et al. A New robust fitting algorithm for vertex reconstruction in the CERES experiment. *Nucl. Instrum. Meth. A*, 394:225–231, 1997.

[69] Albert E. Beaton and John W. Tukey. The fitting of power series, meaning polynomials, illustrated on band-spectroscopic data. *Technometrics*, 16(2):147–185, 1974.

[70] P Cortese et al. ALICE technical design report on forward detectors: FMD, T0 and V0. 9 2004.

[71] J. Conrad, J. G. Contreras, and C. E. Jorgensen. Minimum bias triggers in proton-proton collisions with VZERO and pixel detectors. 2005.

[72] Peter Zeiler Skands. Tuning Monte Carlo Generators: The Perugia Tunes. *Phys. Rev. D*, 82:074018, 2010.

[73] S. Acharya et al. Underlying-event properties in pp and p–Pb collisions at $\sqrt{s_{\rm NN}} = 5.02$ TeV. *JHEP*, 06:023, 2023.

[74] K Aamodt et al. The ALICE experiment at the CERN LHC. *JINST*, 3(08):S08002, Aug 2008.

[75] S. Acharya et al. Production of pions, kaons, and protons as a function of the relative transverse activity classifier in pp collisions at $\sqrt{s} = 13$ TeV. *JHEP*, 06:027, 2023.

[76] The ALICE definition of primary particles. Jun 2017.

[77] Betty Abelev et al. Centrality Dependence of Charged Particle Production at Large Transverse Momentum in Pb–Pb Collisions at $\sqrt{s_{\rm NN}} = 2.76$ TeV. *Phys. Lett. B*, 720:52–62, 2013.

[78] G. D'Agostini. A multidimensional unfolding method based on Bayes' theorem. *Nuclear Instruments and Methods in Physics Research Section A: Accelerators, Spectrometers, Detectors and Associated Equipment*, 362(2):487–498, 1995.

[79] Tim Adye. Unfolding algorithms and tests using RooUnfold. In *PHYSTAT 2011*, pages 313–318, Geneva, 2011. CERN.

[80] S. Acharya et al. Transverse momentum spectra and nuclear modification factors of charged particles in pp, p-Pb and Pb-Pb collisions at the LHC. *JHEP*, 11:013, 2018.

[81] Shreyasi Acharya et al. Charged-particle production as a function of multiplicity and transverse spherocity in pp collisions at $\sqrt{s}$ = 5.02 and 13 TeV. *Eur. Phys. J. C*, 79(10):857, 2019.

[82] Christian Bierlich, Gösta Gustafson, Leif Lönnblad, and Harsh Shah. The Angantyr model for Heavy-Ion Collisions in PYTHIA8. *JHEP*, 10:134, 2018.

[83] Hong Pi. An event generator for interactions between hadrons and nuclei — fritiof version 7.0. *Computer Physics Communications*, 71(1):173–192, 1992.

[84] Shreyasi Acharya et al. Charged-particle production as a function of multiplicity and transverse spherocity in pp collisions at $\sqrt{s}$ = 5.02 and 13 TeV. *Eur. Phys. J. C*, 79(10):857, 2019.

[85] S. Acharya et al. Transverse momentum spectra and nuclear modification factors of charged particles in pp, p-Pb and Pb-Pb collisions at the LHC. *JHEP*, 11:013, 2018.

[86] René Brun, F Bruyant, Federico Carminati, Simone Giani, M Maire, A McPherson, G Patrick, and L Urban. *GEANT: Detector Description and Simulation Tool; Oct 1994*. CERN Program Library. CERN, Geneva, 1993. Long Writeup W5013.

[87] Shreyasi Acharya et al. Production of charged pions, kaons, and (anti-)protons in Pb-Pb and inelastic *pp* collisions at $\sqrt{s_{NN}}$ = 5.02 TeV. *Phys. Rev. C*, 101(4):044907, 2020.

[88] S. Acharya et al. Charged-particle multiplicity distributions over a wide pseudorapidity range in proton-proton collisions at $\sqrt{s}$ = 0.9, 7, and 8 TeV. *Eur. Phys. J. C*, 77(12):852, 2017.

[89] S. V. Tezlaf. Significance of the negative binomial distribution in multiplicity phenomena. *Phys. Scripta*, 98(11):115310, 2023.

[90] Antonio Ortiz. Energy dependence of underlying-event observables from RHIC to LHC energies. *Phys. Rev. D*, 104:076019, 2021.

[91] Timo Antero Aaltonen et al. Study of the energy dependence of the underlying event in proton-antiproton collisions. *Phys. Rev. D*, 92(9):092009, 2015.

[92] Mark Strikman. Transverse Nucleon Structure and Multiparton Interactions. *Acta Phys. Polon. B*, 42:2607–2630, 2011.

[93] Albert M Sirunyan et al. Pseudorapidity distributions of charged hadrons in proton-lead collisions at $\sqrt{s_{\rm NN}} = 5.02$ and 8.16 TeV. *JHEP*, 01:045, 2018.

[94] Antonio Ortiz, Guy Paić, and Eleazar Cuautle. Mid-rapidity charged hadron transverse spherocity in pp collisions simulated with Pythia. *Nucl. Phys. A*, 941:78–86, 2015.

[95] Cari Cesarotti and Jesse Thaler. A Robust Measure of Event Isotropy at Colliders. *JHEP*, 08:084, 2020.

[96] Filip Krizek. Search for jet quenching effects in high-multiplicityproton-proton collisions at $\sqrt{s} = 13$ TeV. *PoS*, HardProbes2020:156, 2021.

[97] Torbjörn Sjöstrand et al. An introduction to PYTHIA 8.2. *Comput. Phys. Commun.*, 191:159–177, 2015.

[98] Bo Andersson, G. Gustafson, G. Ingelman, and T. Sjostrand. Parton Fragmentation and String Dynamics. *Phys. Rept.*, 97:31–145, 1983.

[99] Spyros Argyropoulos and Torbjörn Sjöstrand. Effects of color reconnection on $t\bar{t}$ final states at the LHC. *JHEP*, 11:043, 2014.

[100] Christian Bierlich and Jesper Roy Christiansen. Effects of color reconnection on hadron flavor observables. *Phys. Rev. D*, 92(9):094010, 2015.

[101] Shreyasi Acharya et al. Measurement of Prompt D^0, Λ_c^+, and $\Sigma_c^{0,++}(2455)$ Production in Proton–Proton Collisions at $\sqrt{s} = 13$ TeV. *Phys. Rev. Lett.*, 128(1):012001, 2022.

[102] Shreyasi Acharya et al. Λ_c^+ production in *pp* and in *p*-Pb collisions at $\sqrt{s_{NN}}$=5.02 TeV. *Phys. Rev. C*, 104(5):054905, 2021.

[103] Antonio Ortiz and Guy Paic. A look into the "hedgehog" events in pp collisions using a new event shape – flatenicity. 4 2022.

[104] Collaboration ALICE. Letter of intent for ALICE 3: A next generation heavy-ion experiment at the LHC. Technical report, CERN, Geneva, Mar 2022.

[105] Antonio Ortiz. Experimental results on event shapes at hadron colliders. *Adv. Ser. Direct. High Energy Phys.*, 29:343–357, 2018.

[106] Antonio Ortiz, Gyula Bencedi, and Héctor Bello. Revealing the source of the radial flow patterns in proton–proton collisions using hard probes. *J. Phys. G*, 44(6):065001, 2017.

[107] Shreyasi Acharya et al. Observation of a multiplicity dependence in the p_{T}-differential charm baryon-to-meson ratios in proton-proton collisions at $\sqrt{s} = 13$ TeV. *Phys. Lett. B*, 829:137065, 2022.

[108] Antonio Ortiz, Peter Christiansen, Eleazar Flores, Ivonne Cervantes, and Guy Paic. Color Reconnection and Flowlike Patterns in *pp* Collisions. *Phys. Rev. Lett.*, 111(4):042001, 2013.

[109] Shreyasi Acharya et al. Λ_c^+ Production and Baryon-to-Meson Ratios in pp and p-Pb Collisions at $\sqrt{s_{NN}}$=5.02 TeV at the LHC. *Phys. Rev. Lett.*, 127(20):202301, 2021.

[110] Betty Bezverkhny Abelev et al. Multiplicity Dependence of Pion, Kaon, Proton and Lambda Production in p-Pb Collisions at $\sqrt{s_{NN}} = 5.02$ TeV. *Phys. Lett. B*, 728:25–38, 2014.

[111] Pengyao Cui. Production of strange hadrons in jets and underlying events in pp and p–Pb collisions with ALICE. *Phys. Scripta*, 97(5):054009, 2022.

Publications

Research Articles

- **ALICE** Collaboration, "Charged-particle production as a function of the relative transverse activity classifier in pp, p–Pb, and Pb–Pb collisions at the LHC", JHEP 01 (2024) 056, doi:10.1007/JHEP01(2024)056, arXiv:2310.07490 [nucl-ex]
- **ALICE** Collaboration, "Underlying-event properties in pp and p–Pb collisions at $\sqrt{s_{\rm NN}} = 5.02\,\text{TeV}$", JHEP 06 (2023) 023, doi:10.1007/JHEP06(2023)023, arXiv:2204.10389 [nucl-ex]
- A. Ortiz, A. Khuntia, O. Vázquez-Rueda, S. Tripathy, G. Bencedi, S. Prasad, and F. Fan, "Unveiling the effects of multiple soft partonic interactions in pp collisions at $\sqrt{s} = 13.6$ TeV using a new event classifier", Phys. Rev. D 107 (2023) 7, 076012, doi:10.1103/PhysRevD.107.076012, arXiv:2211.06093 [hep-ph]

Conference Proceeding

- F. Fan, "Particle production as a function of underlying-event activity and very forward energy with ALICE", EPJ Web Conf. 276 (2023) 01009, arXiv:2208.11348 [nucl-ex], Contribution to: SQM 2022 (the 20th International Conference on Strangeness in Quark Matter)

Acknowledgement

To me, the journey to pursue a doctorate has been an adventure full of fun, challenge, and self-exploration. It is like the growth of life, spiraling upwards to new heights. I am honoured to have worked with many colleagues throughout this journey. I am deeply thankful to my supervisors, Daicui Zhou and Antonio Ortiz Velásquez, whose support and guidance will always steer me to the right path in my career. I am also appreciative of Andreas Morsch's valuable suggestions on my work. This work received support from CONAHCyT under the Grants CB A1-S-22917 and CF 2042; as well as from PAPIIT-UNAM under the grant number IG100524. It was also supported by the NSFC Key Grant 12061141008 and National Key R&D Program of China under Grant 2018YFE0104700 and 2018YFE0104800.

In addition, I would like to express my heartfelt gratitude to my ALICE colleagues at Central China Normal University (CCNU): Yaxian Mao, Hua Pei, Zhongbao Yin, Xiaoming Zhang, and Daicui Zhou. I am also appreciative of my doctoral dissertation defense committee: Andreas Morsch, Antonio Ortiz Velásquez, Jinhui Chen, Yaxian Mao, Zebo Tang, Benwei Zhang, and Daicui Zhou, who provided rigorous assessments and valuable suggestions.

I would also like to extend my heartfelt gratitude to my friends at Instituto de Ciencias Nucleares, Universidad Nacional Autónoma de México in Mexico: Paola Vargas, Áulide Martínez Tapia, Jesús Eduardo Muñoz Méndez, Ale García Madrigal, Marco Díaz, Carlos Díaz, Donaldo Orbe, and Alex Santacruz, who have provided me with invaluable assistance and have brought me a lot of joy during my stay in Mexico.

I am grateful to my friends and classmates at CCNU, including Lin Chen, Jiamin Chen, Shuo Chen, Linlin Huang, Yuan Wang, Jianhui Zhu, Ran Xu, Xinye Peng, Xinglong Li, Ahsan Mehmood Khan, Qundong Han, Ya Zhu, Wan Chang, Guangfu Zhu, Yanchun Ding, Pengyao Cui, Tiantian Yin, Hongli Ma, Huijin Guo, Yongzhen Hou, Tiantian Cheng, Mingyu Zhang, Wendan Guo, Xiuxiu Jiang, Siyu Tang, Biao Zhang, Yingjie Zhou, Donghai Liu, Tao Fang, Sheng Bai, Liu He, Youpeng Su, Zhaozheng Geng, Jie Yi, Yubiao Wang, Xinyi Zhou, Qiuyue Zhang, Feng Li, Hao Liu, Wenhui Feng, Yu Wang, Lang Xu, among others, who brought me a lot of fun and engaged in many physics-related discussions with me.

Finally, I thank my parents and myself. One small step for me, one giant leap for my future career.